MIT Libraries | DSpace@MIT

MIT Open Access Articles

Nucleon structure from mixed action calculations using 2+1 flavors of asqtad sea and domain wall valence fermions

The MIT Faculty has made this article openly available. ***Please share*** how this access benefits you. Your story matters.

Citation: Bratt, J. et al., LHPC. "Nucleon Structure from Mixed Action Calculations Using 2+1 Flavors of Asqtad Sea and Domain Wall Valence Fermions." Physical Review D 82.9 (2010) : © 2010 The American Physical Society

As Published: http://dx.doi.org/10.1103/PhysRevD.82.094502

Publisher: American Physical Society

Persistent URL: http://hdl.handle.net/1721.1/62191

Version: Final published version: final published article, as it appeared in a journal, conference proceedings, or other formally published context

Terms of Use: Article is made available in accordance with the publisher's policy and may be subject to US copyright law. Please refer to the publisher's site for terms of use.

Massachusetts Institute of Technology

Nucleon structure from mixed action calculations using 2 + 1 flavors of asqtad sea and domain wall valence fermions

J. D. Bratt,[1] R. G. Edwards,[2] M. Engelhardt,[3] Ph. Hägler,[4] H. W. Lin,[2,5] M. F. Lin,[1,6] H. B. Meyer,[1,7] B. Musch,[4,2] J. W. Negele,[1] K. Orginos,[8] A. V. Pochinsky,[1] M. Procura,[1,4] D. G. Richards,[2] W. Schroers,[9,*] and S. N. Syritsyn[1]

(LHPC)

[1]*Center for Theoretical Physics, Massachusetts Institute of Technology, Cambridge, Massachusetts 02139, USA*
[2]*Thomas Jefferson National Accelerator Facility, Newport News, Virginia 23606, USA*
[3]*Department of Physics, New Mexico State University, Las Cruces, New Mexico 88003-0001, USA*
[4]*Physik-Department der TU München, James-Franck-Straße, D-85748 Garching, Germany*
[5]*Department of Physics, University of Washington, Seattle, Washington 98195-1560, USA*
[6]*Department of Physics, Sloane Laboratory, Yale University, New Haven, Connecticut 06520, USA*
[7]*CERN Physics Department, 1211 Geneva 23, Switzerland*
[8]*Department of Physics, College of William and Mary, P.O. Box 8795, Williamsburg, Virginia 23187-8795, USA*
[9]*Institute of Physics, Academia Sinica, Taipei 115, Taiwan, Republic of China*
(Received 1 February 2010; published 5 November 2010)

We present high statistics results for the structure of the nucleon from a mixed-action calculation using 2 + 1 flavors of asqtad sea and domain-wall valence fermions. We perform extrapolations of our data based on different chiral effective field theory schemes and compare our results with available information from phenomenology. We discuss vector and axial form factors of the nucleon, moments of generalized parton distributions, including moments of forward parton distributions, and implications for the decomposition of the nucleon spin.

DOI: 10.1103/PhysRevD.82.094502 PACS numbers: 12.38.Gc, 13.60.Fz

I. INTRODUCTION

Determining the structure of the nucleon in terms of quarks and gluons is central to our goal of understanding baryonic matter at the level of its smallest constituents. While the theory describing the strong interactions of quarks and gluons, quantum chromodynamics, was identified 35 years ago, its predictions at low energies have been notoriously hard to derive *ab initio*. The modern approach to calculating the properties of hadrons is based on the Euclidean path integral representation of QCD discretized on a space-time lattice, i.e. lattice QCD. Importance sampling methods, implemented on massively parallel computers, make it possible to extract, in particular, many properties of the nucleon.

In recent years, advances both in algorithms and in computer technology made a series of remarkable calculations possible that had a large impact on our understanding of nucleon structure. Among the quantities calculated we would like to mention the quark contribution to the nucleon spin [1,2], the nucleon transverse structure [3], and the nucleon axial charge [4,5]. Recently, the nucleon electromagnetic and axial form factors have received special attention in Refs. [6,7] using dynamical Wilson and asqtad fermions. Another important milestone is the advent of full domain-wall calculations (see Refs. [8,9]) and of dynamical twisted-mass fermions [10]. Disconnected diagrams play a key role in an ongoing study of the strange quark content of the nucleon [11]. For reviews and progress reports on the current state of the field, see Refs. [12–15].

Over the past years several of us have reported on hadron structure measurements using mixed-action calculations with 2 + 1 flavors of dynamical asqtad sea quarks [16,17]—corresponding to degenerate u, d quarks + the strange quark—and domain-wall valence quarks [18–22]. A significant milestone was reached in Ref. [20], which summarized our findings for higher moments of generalized form factors. The current paper represents a major update of that work: it includes the observables presented previously with higher statistics, as well as an additional, lower pion-mass calculation. Beyond that, it covers form factors and chiral extrapolations of the forward moments that were not shown previously. The propagators and technology underlying these calculations have not only successfully been applied to nucleon structure, but have also turned out to be enormously valuable to other studies; see e.g. [23–25] and references therein. Mixed-action calculations have also been studied in the framework of effective field theory; see [26–28]. It is the purpose of the current paper to report our final results including all improvements we have made over the years on the method and technology of our computations.

The layout of this paper is as follows. We give an overview of our notation and conventions and present the

*Current address: NuAS, Stubenrauchstrasse 3, 12357 Berlin, Germany.

 © 2010 The American Physical Society

observables that we study in Sec. II. The discussion of our technology and of the improvements we have made over our previous calculations together with consistency checks takes place in Sec. III. Our results are presented in Sec. IV which is divided into the following subsections: Section IV A is dedicated to the axial charge g_A. The discussion of the electromagnetic form factors and the axial form factors takes place in Secs. IV B and IV C, respectively. The generalized form factors and their extrapolation using different schemes of chiral effective theory are presented in Sec. IV D.

The generalized form factors of the energy-momentum tensor provide vital information as to how spin is apportioned within the nucleon—a long-standing puzzle of hadron physics. In particular, they enable a first-principles calculation in lattice QCD of J_q, the total angular momentum carried by the quarks [1,2,20,29,30], and hence have a crucial role in resolving this puzzle. Section IV E is dedicated to this topic. Our summary and outlook for future work are given in Sec. V. Since the summary includes cross references to the most significant tables and figures, the reader mainly interested in new results might find it useful to use that section as a guide to the highlights of our calculations.

II. OVERVIEW OF PHYSICAL OBSERVABLES

The observables we are reporting on are defined via matrix elements of bilocal light-cone quark operators in nucleon states. They can be systematically discussed in the framework of so-called generalized parton distributions [31–34]. The relevant bilocal operator is given by

$$\mathcal{O}_{q,\Gamma}(x) = \int \frac{d\lambda}{4\pi} e^{i\lambda x} \bar{q}\left(\frac{-\lambda n}{2}\right)\Gamma_\mu n^\mu \mathcal{P} e^{-ig\int_{-\lambda/2}^{\lambda/2} d\alpha n\cdot A(\alpha n)} \times q\left(\frac{\lambda n}{2}\right), \quad (1)$$

with x being the momentum fraction, n a light-cone vector, and Γ representing any gamma matrix from the basis γ_μ, $\gamma_\mu\gamma_5$, and $\sigma_{\mu j}$, $j = 1, 2$.

The quark field q in Eq. (1) can carry any of the up, down, or strange flavors; however, here we restrict ourselves to $q = u, d$. Since in our lattice calculations the up and down quarks have degenerate masses, isospin symmetry is built in by construction. Note that our matrix elements always refer to the case of a proton; i.e. the nucleon sources used in the construction of the matrix elements in Eqs. (12) and (13) below always contain two u and one d quark. When comparing lattice matrix elements to experiment, we need to choose appropriate flavors or flavor combinations. The isovector combination $\mathcal{O}_q \equiv \mathcal{O}_u - \mathcal{O}_d$, where we subtract the down-quark contribution from that of the up quarks, can be constructed from the difference between proton and neutron observables obtained in experiment. The isoscalar combination $\mathcal{O}_{u+d}$, on the other hand, corresponds to the sum of proton and neutron observables. To compute proton observables as measured by probing a proton with a photon, one needs to take into account the charge weighting factors of the quark-photon vertex and thus consider the combination $q = 2/3u - 1/3d$. In all but the isovector case, the matrix elements will in principle receive contributions from both the connected and the disconnected diagrams. In this work we have neglected the disconnected contributions since they are very costly to obtain. For recent studies of disconnected contributions in the framework of calculations of form factors and moments of parton distribution functions (PDFs) we refer to, e.g. Refs. [35,36].

The matrix elements of the operator Eq. (1) between nucleon states with momentum $\vec{p}$ and polarization λ can be parametrized generically by exploiting their Lorentz tensor structure. This has been discussed in detail in the literature [34], and we merely present the results here.

For the case $\Gamma_\mu = \gamma_\mu$, the nucleon matrix element adopts the form

$$\langle p', \lambda'|\mathcal{O}_{q,\gamma}(x)|p, \lambda\rangle = \langle\langle \not{n}\rangle\rangle H(x, \xi, t) + \frac{n_\mu \Delta_\alpha}{2m}\langle\langle i\sigma^{\mu\alpha}\rangle\rangle E(x, \xi, t), \quad (2)$$

where we have introduced the notation $\langle\langle \mathcal{X}\rangle\rangle = \bar{u}(p', \lambda')\mathcal{X}u(p, \lambda)$ and the parameters $\Delta = p' - p$, $t \equiv -Q^2 = -(p' - p)^2$, and $\xi = -n\cdot\Delta/2$. In the framework of form factors in Secs. IV B and IV C, we will denote the squared momentum transfer by Q^2 since this is a common and widespread convention. The unpolarized generalized parton distributions (GPDs) $H(x, \xi, t)$ and $E(x, \xi, t)$ are Lorentz scalars and thus frame-independent functions parametrizing the matrix element. We point out that the matrix element also depends implicitly on a renormalization scale, μ^2, and scheme.

In the case $\Gamma_\mu = \gamma_\mu\gamma_5$ we obtain a Lorentz-covariant parametrization in terms of the polarized GPDs $\tilde{H}(x, \xi, t)$ and $\tilde{E}(x, \xi, t)$:

$$\langle p', \lambda'|\mathcal{O}_{q,\gamma\gamma_5}(x)|p, \lambda\rangle = \langle\langle \not{n}\gamma_5\rangle\rangle \tilde{H}(x, \xi, t) + \frac{n\cdot\Delta}{2m}\langle\langle\gamma_5\rangle\rangle \tilde{E}(x, \xi, t). \quad (3)$$

The case $\Gamma_{\mu,j} = \sigma_{\mu j}$ will be discussed in a separate publication [37]. The kinematic parameter x is the average longitudinal momentum fraction of the struck quark, and ξ and t are the longitudinal and the total squared momentum transfer to the nucleon, respectively. The GPDs are

defined over the full intervals $x = -1 \cdots +1$, and $\xi = -1 \cdots +1$. Depending on whether $|x| > |\xi|$ or vice versa they have the interpretation of amplitudes for the emission and absorption of a quark or for the emission of a quark-antiquark pair, respectively.

An attractive feature of the generalized parton distributions is that they occur in a range of different processes, e.g. deeply virtual Compton scattering, wide-angle Compton scattering, and exclusive meson production, in addition to the classic processes that probe the forward parton distributions and form factors. The challenge of GPDs lies in their more complex structure—each generalized parton distribution is a function of three parameters rather than just one, and the different experimental processes provide different constraints on their form. Typically only convolutions of these functions in the x variable are experimentally accessible.

Since lattice calculations deal with operators and matrix elements in Euclidean space, a direct computation of nonlocal light-cone elements is not possible. To facilitate the lattice calculations, one takes x^{n-1} moments of Eqs. (2) and (3), yielding a tower of local operators whose matrix elements can be related to the corresponding moments of H, E, $\tilde{H}$, and $\tilde{E}$. In this study, we will compute matrix elements of the following local generalized currents,

$$\mathcal{O}_{q,\Gamma}^{\{\mu_1 \cdots \mu_n\}} = \bar{q}(0)\Gamma^{\{\mu_1} \mathrm{i}\overleftrightarrow{D}^{\mu_2} \cdots \mathrm{i}\overleftrightarrow{D}^{\mu_n\}} q(0), \tag{4}$$

where, again, Γ^μ can refer to either γ^μ or $\gamma^\mu\gamma_5$. Curly braces around indices represent a symmetrization and the subtraction of traces of the indices and the derivative is defined via $\overleftrightarrow{D} = 1/2(\vec{D} - \overleftarrow{D})$.

Taking the moments with respect to (w.r.t.) x of the GPDs, we define

$$\begin{aligned} H^n(\xi, t) &\equiv \int_{-1}^{1} dx x^{n-1} H(x, \xi, t), \\ E^n(\xi, t) &\equiv \int_{-1}^{1} dx x^{n-1} E(x, \xi, t), \\ \tilde{H}^n(\xi, t) &\equiv \int_{-1}^{1} dx x^{n-1} \tilde{H}(x, \xi, t), \\ \tilde{E}^n(\xi, t) &\equiv \int_{-1}^{1} dx x^{n-1} \tilde{E}(x, \xi, t). \end{aligned} \tag{5}$$

The nonforward nucleon matrix elements of the local operators, Eq. (4), can in turn be parametrized according to their Lorentz structure in terms of generalized form factors (GFFs) $A_{nm}(t)$, $\tilde{A}_{nm}(t)$, $B_{nm}(t)$, $\tilde{B}_{nm}(t)$, and $C_{nm}(t)$,

$$\begin{aligned} \langle p', \lambda' | \mathcal{O}^{\mu_1} | p, \lambda \rangle &= \langle\langle \gamma^{\mu_1} \rangle\rangle A_{10}(t) + \frac{\mathrm{i}}{2m} \langle\langle \sigma^{\mu_1 \alpha} \rangle\rangle \Delta_\alpha B_{10}(t), \\ \langle p', \lambda | \mathcal{O}^{\{\mu_1 \mu_2\}} | p, \lambda \rangle &= \bar{p}^{\{\mu_1} \langle\langle \gamma^{\mu_2\}} \rangle\rangle A_{20}(t) + \frac{\mathrm{i}}{2m} \bar{p}^{\{\mu_1} \langle\langle \sigma^{\mu_2\}\alpha} \rangle\rangle \Delta_\alpha B_{20}(t) + \frac{1}{m} \Delta^{\{\mu_1} \Delta^{\mu_2\}} C_{20}(t), \\ \langle p', \lambda' | \mathcal{O}^{\{\mu_1 \mu_2 \mu_3\}} | p, \lambda \rangle &= \bar{p}^{\{\mu_1} \bar{p}^{\mu_2} \langle\langle \gamma^{\mu_3\}} \rangle\rangle A_{30}(t) + \frac{\mathrm{i}}{2m} \bar{p}^{\{\mu_1} \bar{p}^{\mu_2} \langle\langle \sigma^{\mu_3\}\alpha} \rangle\rangle \Delta_\alpha B_{30}(t) + \Delta^{\{\mu_1} \Delta^{\mu_2} \langle\langle \gamma^{\mu_3\}} \rangle\rangle A_{32}(t) \\ &\quad + \frac{\mathrm{i}}{2m} \Delta^{\{\mu_1} \Delta^{\mu_2} \langle\langle \sigma^{\mu_3\}\alpha} \rangle\rangle \Delta_\alpha B_{32}(t), \end{aligned} \tag{6}$$

for the vector operators and

$$\begin{aligned} \langle p', \lambda' | \mathcal{O}_{\gamma_5}^{\mu_1} | p, \lambda \rangle &= \langle\langle \gamma^{\mu_1} \gamma_5 \rangle\rangle \tilde{A}_{10}(t) + \frac{1}{2m} \Delta^{\mu_1} \langle\langle \gamma_5 \rangle\rangle \tilde{B}_{10}(t), \\ \langle p', \lambda' | \mathcal{O}_{\gamma_5}^{\{\mu_1 \mu_2\}} | p, \lambda \rangle &= \bar{p}^{\{\mu_1} \langle\langle \gamma^{\mu_2\}} \gamma_5 \rangle\rangle \tilde{A}_{20}(t) + \frac{1}{2m} \Delta^{\{\mu_1} \bar{p}^{\mu_2\}} \langle\langle \gamma_5 \rangle\rangle \tilde{B}_{20}(t), \\ \langle p', \lambda' | \mathcal{O}_{\gamma_5}^{\{\mu_1 \mu_2 \mu_3\}} | p, \lambda \rangle &= \bar{p}^{\{\mu_1} \bar{p}^{\mu_2} \langle\langle \gamma^{\mu_3\}} \gamma_5 \rangle\rangle \tilde{A}_{30}(t) + \frac{1}{2m} \Delta^{\{\mu_1} \bar{p}^{\mu_2} \bar{p}^{\mu_3\}} \langle\langle \gamma_5 \rangle\rangle \tilde{B}_{30}(t) + \Delta^{\{\mu_1} \Delta^{\mu_2} \langle\langle \gamma^{\mu_3\}} \gamma_5 \rangle\rangle \tilde{A}_{32}(t) \\ &\quad + \frac{1}{2m} \Delta^{\{\mu_1} \Delta^{\mu_2} \Delta^{\mu_3\}} \langle\langle \gamma_5 \rangle\rangle \tilde{B}_{32}(t), \end{aligned} \tag{7}$$

for the axial-vector operators. Here we have defined the average nucleon momentum $\bar{p} = (p' + p)/2$. By comparing this with the x^{n-1} moments of Eqs. (2) and (3), and using Eq. (5), one finds that the ξ dependence of the moments of the GPDs is merely polynomial,

$$\begin{aligned} H^{n=1}(\xi, t) &= A_{10}(t), \\ H^{n=2}(\xi, t) &= A_{20}(t) + (2\xi)^2 C_{20}(t), \\ H^{n=3}(\xi, t) &= A_{30}(t) + (2\xi)^2 A_{32}(t), \\ E^{n=1}(\xi, t) &= B_{10}(t), \\ E^{n=2}(\xi, t) &= B_{20}(t) - (2\xi)^2 C_{20}(t), \\ E^{n=3}(\xi, t) &= B_{30}(t) + (2\xi)^2 B_{32}(t), \ldots, \end{aligned} \tag{8}$$

and

$$\begin{aligned} \tilde{H}^{n=1}(\xi, t) &= \tilde{A}_{10}(t), \\ \tilde{H}^{n=2}(\xi, t) &= \tilde{A}_{20}(t), \\ \tilde{H}^{n=3}(\xi, t) &= \tilde{A}_{30}(t) + (2\xi)^2 \tilde{A}_{32}(t), \\ \tilde{E}^{n=1}(\xi, t) &= \tilde{B}_{10}(t), \\ \tilde{E}^{n=2}(\xi, t) &= \tilde{B}_{20}(t), \\ \tilde{E}^{n=3}(\xi, t) &= \tilde{B}_{30}(t) + (2\xi)^2 \tilde{B}_{32}(t), \ldots. \end{aligned} \tag{9}$$

In the forward limit of Eqs. (2) and (3) with $\vec{p} = \vec{p}'$, we obtain the well-known parton distribution functions,

$$\begin{aligned} q(x) &= H(x, \xi = 0, t = 0), \\ \Delta q(x) &= \tilde{H}(x, \xi = 0, t = 0). \end{aligned} \tag{10}$$

Note that in the case $\xi = 0$ the GPDs—and also the GFFs, including the form factors for $n = 1$—admit a probability interpretation [38] and that this property holds even in the case $t \neq 0$. Taking together Eqs. (5) and (8)–(10), and setting $t = 0$, will similarly yield the moments

$$\begin{aligned} \langle x^{n-1} \rangle_q &= H^n(0, 0) = A_{n0}(0), \\ \langle x^{n-1} \rangle_{\Delta q} &= \tilde{H}^n(0, 0) = \tilde{A}_{n0}(0). \end{aligned} \tag{11}$$

The matrix elements are obtained on the lattice from the two-point functions

$$C^{2\mathrm{pt}}(T, \vec{p}) = \sum_{\vec{x}} e^{-\mathrm{i}\vec{p}\cdot\vec{x}} \mathrm{Tr}(\Gamma_{\mathrm{pol}} \langle n(\vec{x}, T) \bar{n}(\vec{0}, 0) \rangle), \tag{12}$$

and the three-point functions

$$\begin{aligned} C^{3\mathrm{pt}}_{\mathcal{O}}(T, T_0, \vec{p}, \vec{p}') = \sum_{\vec{x}, \vec{y}} e^{-\mathrm{i}\vec{p}'\cdot\vec{x} + \mathrm{i}(\vec{p}' - \vec{p})\cdot\vec{y}} \mathrm{Tr}(\Gamma_{\mathrm{pol}} \langle n(\vec{x}, T_0) \\ \times \mathcal{O}(\vec{y}, T) \bar{n}(\vec{0}, 0) \rangle). \end{aligned} \tag{13}$$

We have introduced the lattice proton operators, $n(\vec{x}, T)$ and $\bar{n}(\vec{x}, T)$. In order to maximize overlap with the ground state, we use the smeared sources defined in Ref. [39]. This overlap can be parametrized by a function $Z(\vec{p})$ according to $\langle \Omega | n(x) | \vec{p}, \lambda \rangle = \sqrt{Z(\vec{p})} u(p, \lambda) e^{-\mathrm{i}p\cdot x}$. We also use the projection operator, $\Gamma_{\mathrm{pol}} = \frac{1}{2}(1 + \gamma_4)\frac{1}{2}(1 - \mathrm{i}\gamma_3\gamma_5)$. $\mathcal{O} = \bar{q}(0)\mathcal{J}q(0)$ denotes the operator with all appropriate indices in which we are interested.

Applying the transfer matrix formalism yields the following expression for the behavior of the two- and three-point functions:

$$\begin{aligned} C^{2\mathrm{pt}}(T, \vec{p}) &= \frac{Z(\vec{p}) e^{-ET}}{2E} \mathrm{Tr}(\Gamma_{\mathrm{pol}}(\mathrm{i}\not{p} + m_N)) \\ &\quad + \text{excited states}. \\ C^{3\mathrm{pt}}_{\mathcal{O}}(T, T_0, \vec{p}, \vec{p}') &= \frac{\sqrt{Z(\vec{p}) Z(\vec{p}')} e^{-E'(T_0 - T) - ET}}{2E' 2E} \\ &\quad \times \mathrm{Tr}(\Gamma_{\mathrm{pol}}(\mathrm{i}\not{p}' + m_N) \mathcal{J} (\mathrm{i}\not{p} + m_N)) \\ &\quad + \text{excited states}. \end{aligned} \tag{14}$$

In order to cancel the exponential factors and wave-function normalizations, we construct the ratio

$$\begin{aligned} R_{\mathcal{O}}(T, T_0) &= \frac{C^{3\mathrm{pt}}_{\mathcal{O}}(T, T_0, \vec{p}, \vec{p}')}{\sqrt{C^{2\mathrm{pt}}(T, \vec{p}) C^{2\mathrm{pt}}(T, \vec{p}')}} \\ &\quad \times \sqrt{\frac{C^{2\mathrm{pt}}(T_0 - T, \vec{p}) C^{2\mathrm{pt}}(T, \vec{p}')}{C^{2\mathrm{pt}}(T_0 - T, \vec{p}') C^{2\mathrm{pt}}(T, \vec{p})}} \\ &\xrightarrow{T_0 \gg T \gg 1} \sum_{\lambda, \lambda'} \frac{\bar{u}(\vec{p}, \lambda) \Gamma_{\mathrm{pol}} u(\vec{p}', \lambda')}{\sqrt{2E(E + m_N) 2E'(E' + m_N)}} \\ &\quad \times \langle \vec{p}', \lambda' | \mathcal{O} | \vec{p}, \lambda \rangle, \end{aligned} \tag{15}$$

which becomes proportional to the desired matrix elements for sufficiently large source-sink separations, T_0, and with the operator insertion sufficiently far from both source and sink, $T \gg 1$ and $T_0 - T \gg 1$. Typically, we find a plateau region $[T_{\min}, T_{\max}]$ over which we average the resulting value of the operator.

Since we operate with a finite lattice of extent aL, the momentum values which we can choose are discrete and are given by $\vec{p} = 2\pi/(aL)\vec{n}_p$ with $\vec{n}_p$ a vector whose components are integers ranging from $-L/2$ to $L/2$. For the nucleon sink we choose the two values $\vec{p}' = 2\pi/(aL)\vec{0}$ and $\vec{p}' = 2\pi/(aL)(-1, 0, 0)$ and for the source we choose $\vec{p}$ such that the absolute value of the integer momentum vector, $|\vec{n}_p|$ is smaller than 5. This defines the set of t values accessible in our calculation. Note that the (generalized) form factors will receive contributions from several different momentum and index combinations at any fixed value of t. By constructing an overdetermined system of equations from all those combinations we make optimal use of the available data. This procedure has been discussed in detail in Ref. [2].

The energy of a state at momentum $\vec{p}$ is related to its mass through the dispersion relation. In our analysis we use the continuum dispersion relation. We have verified that the resulting energy agrees, for the spatial momenta employed in our calculation, with the energy of a nucleon at nonzero momentum actually calculated on the lattice.

In the case of the electromagnetic current, $\bar{\psi}\gamma_\mu\psi$, the generalized form factors correspond to the electromagnetic form factors of the nucleon. For the axial current, $\bar{\psi}\gamma_\mu\gamma_5\psi$, the form factors correspond to the axial and the pseudoscalar form factors. These will be covered in detail in Secs. IV B and IV C.

TABLE I. Summary of our data sets.

$m_{\rm sea}^{\rm asqtad}$, $N_f = 2+1$	$m_{\rm val}^{\rm DWF}$	Volume	No. confs.	No. meas.
0.007/0.050	0.0081	$20^3 \times 64$	463	3704
0.010/0.050	0.0138	$28^3 \times 64$	274	2192
0.010/0.050	0.0138	$20^3 \times 64$	631	5048
0.020/0.050	0.0313	$20^3 \times 64$	486	3888
0.030/0.050	0.0478	$20^3 \times 64$	563	4504
0.040/0.050	0.0644	$20^3 \times 32$	350	350
0.050	0.0810	$20^3 \times 32$	425	425

TABLE II. Hadron masses and decay constants in physical units.

Light $m_{\rm sea}^{\rm asqtad}$	Volume Ω	$(am)_\pi$	$(af)_\pi$	$(am)_N$	m_π (MeV)	f_π (MeV)	m_N (MeV)
0.007	$20^3 \times 64$	0.1842(7)	0.0657(3)	0.696(7)	292.99(111)	104.49(45)	1107.1(111)
0.010	$28^3 \times 64$	0.2238(5)	0.0681(2)	0.726(5)	355.98(80)	108.31(34)	1154.8(80)
0.010	$20^3 \times 64$	0.2238(5)	0.0681(2)	0.726(5)	355.98(80)	108.31(34)	1154.8(80)
0.020	$20^3 \times 64$	0.3113(4)	0.0725(1)	0.810(5)	495.15(64)	115.40(23)	1288.4(80)
0.030	$20^3 \times 64$	0.3752(5)	0.0761(2)	0.878(5)	596.79(80)	121.02(34)	1396.5(80)
0.040	$20^3 \times 32$	0.4325(12)	0.0800(5)	0.941(6)	687.94(191)	127.21(78)	1496.8(95)
0.050	$20^3 \times 32$	0.4767(10)	0.0822(4)	0.991(5)	758.24(159)	130.70(67)	1576.3(80)

III. NEW LATTICE CALCULATIONS

We now present the methods and technologies we have used for our calculations. As discussed previously in Ref. [20], we continue to employ the asqtad action for the sea quarks and the domain-wall (DWF) action for the valence quarks. In addition, we also add one lighter mass to our data set. The data sets used in this paper are summarized in Table I. The columns show the bare asqtad quark mass for $N_f = 2 + 1$ dynamical fermions, the corresponding bare DWF mass, the volume in lattice units, the number of gauge field configurations used, and the number of measurements included in the analysis. The bare valence DWF masses have been tuned such that the physical pion masses agree with those obtained from the purely asqtad calculation. The size of the fifth dimension has been set to $L_5 = 16$. The choice and tuning of these parameters has been discussed in detail in Ref. [20].

We work in a mass independent scheme. The lattice spacing is therefore independent of the bare quark mass, and its value has been determined to be $a = 0.1241(25)$ fm, corresponding to $a^{-1} = 1.591(32)$ GeV in Ref. [21], taken from heavy quark spectroscopy [40]. This yields a physical volume of $V = (aL)^3 = (2.5\ \text{fm})^3$ on the $L^3 = 20^3$ lattices and of $V = (aL)^3 = (3.5\ \text{fm})^3$ on the $L^3 = 28^3$ lattice. The physical values of the nucleon masses, pion masses, and pion decay constants are needed for our computation of hadron structure. These have been previously determined in Ref. [21]. We have listed them in Table II. The columns show the bare asqtad sea quark mass, the lattice size, and the resulting lattice pion mass, pion decay constant, and nucleon mass. Finally, they are converted to physical values in MeV.[1]

In contrast with our previous publication [20], in this work we did not use Dirichlet boundary conditions on the first and the middle time slice, forming so-called chopped lattices. Instead, the technology that has been employed consists in computing multiple source/sink pairs on a single gauge field configuration; it is discussed in more detail in Sec. III A. We find this technique both more convenient to use and more powerful in making optimal use of the existing resources. The quality of the results is superior since it allows us to process eight source/sink pairs instead of just two as before. We have recalculated our results on the lattices with asqtad sea quark masses of $m_{\rm sea}^{\rm asqtad} = 0.007$–$0.030$. The higher masses are included in some plots to guide the eye, but have never been included in the chiral fits. Section III B discusses possible systematic errors of our nucleon matrix elements.

We also take all possible sources of correlations into account carefully by performing all fits using the error-correlation matrix among all data points at fixed pion mass and the "superjackknife" technique for combining data from different pion masses in a single fit. These techniques are discussed in Sec. III C. Section III D specifies our renormalization procedure for the lattice operators we use and lists all relevant renormalization constants. Finally, Sec. III E discusses potential influences of finite-volume effects on our lattice data.

[1]Note that unlike in Ref. [21], in this paper we use the normalization of f_π such that $f_\pi = 92.4$ MeV.

A. Improved statistics

In order to improve the statistical quality of our data set, we employ a method we call "coherent sink technique." This method proves to be a substantial improvement over previous methods employed for the extraction of three-point functions from lattice data. Effectively, we obtain eight measurements of matrix elements per configuration. Hence, this allows us to make optimal use of the rather expensive configurations generated with dynamical quarks.

On every other configuration we place sources at space-time positions $(\vec{0}, 0)$, $(\vec{L}/2, 16)$, $(\vec{0}, 32)$, and $(\vec{L}/2, 48)$, where $\vec{L}$ denotes a spatial vector with components (L, L, L). We then perform 12 inversions of the Dirac operator, corresponding to the four spin and three color indices of the quarks, and feed them into the construction of the forward propagators. Using these forward propagators, we create a momentum projected nucleon sink a temporal distance T_0 away from the source; i.e. we end up with four sinks located at Euclidean times T_0, $T_0 + 16$, $T_0 + 32$, and $T_0 + 48$.

If we did a conventional calculation, we would consider each source-sink pair completely separately, constructing a set of backward propagators from the sink and evaluating the three-point function. Thus, each measurement would require a separate set of backward propagator calculations. With our new approach, however, we calculate a single set of coherent backward propagators in the simultaneous presence of all four sinks. Combining these coherent backward propagators with the forward propagators yields the physical matrix elements plus terms that vanish due to gauge invariance when computing expectation values.

Additionally, we also create a momentum projected antinucleon sink a temporal distance $-T_0$ away from each source and perform an analogous calculation for coherent antinucleon propagators. It is then straightforward to relate the matrix elements of our twist-two quark operators in an antinucleon to the desired results in a nucleon. To summarize, given a set of forward propagators, we obtain eight measurements of $C_{\mathcal{O}}^{3\mathrm{pt}}$ at the cost of two rather than eight sets of inversions for the backward propagators. To minimize correlations, we alter the source

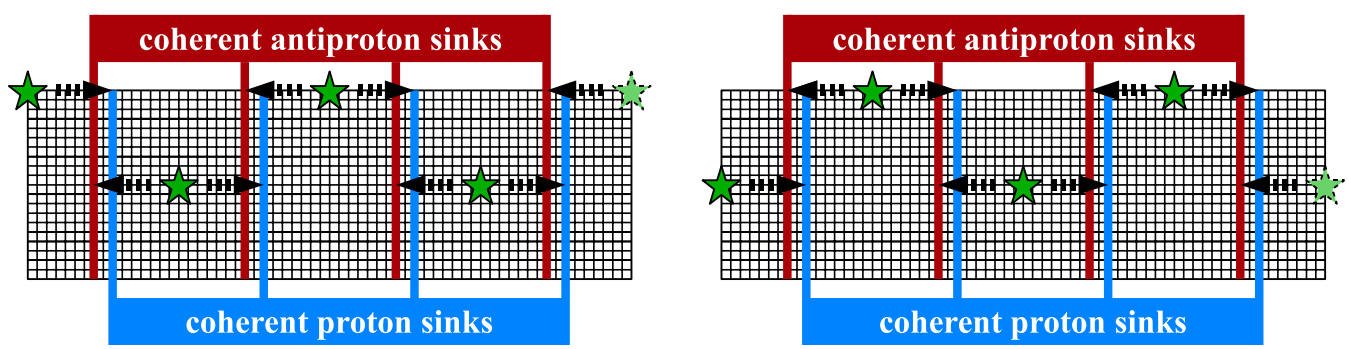

FIG. 1 (color online). Layout of smeared nucleon sources (stars) and coherent, fixed momentum sinks (vertical lines) on our lattices: (left) even configurations; (right) odd configurations.

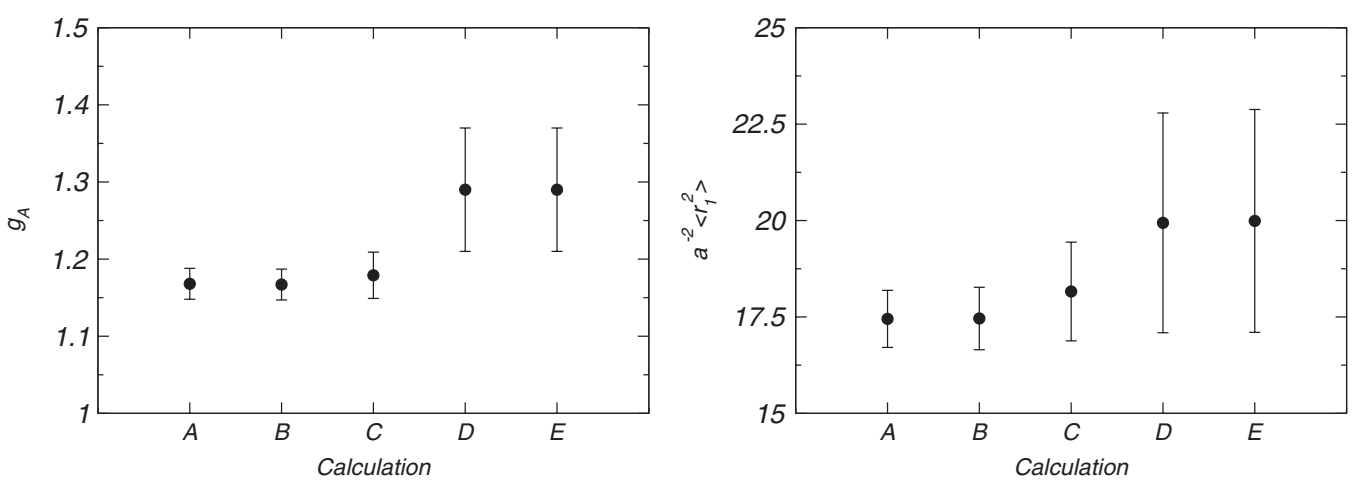

FIG. 2. Comparison of coherent sink technique and two source-sink separations with our previous calculation. The observables are the axial charge, g_A in the left panel [see Sec. IV A], and the isovector charge radius, $a^{-2}\langle r_1^2\rangle$ in the right panel [see Sec. IV B].

TABLE III. Calculation techniques used for the comparison of the coherent sink techniques and two source-sink separations with our previous calculation.

Label	No. meas.	T_0	Technology
A	$448 \cdot 8$	9	Independent backward propagators, nucleon/antinucleon
B	$448 \cdot 8$	9	Coherent backward propagators, nucleon/antinucleon
C	$448 \cdot 8$	10	Coherent backward propagators, nucleon/antinucleon
D	448	10	Single source/conf., nucleon only, unchopped $L_t = 64$ lattice
E	448	10	Single source/conf., nucleon only, chopped $L_t = 32$ lattice

locations on every other lattice to be $(\vec{L}/2, 0)$, $(\vec{0}, 16)$, $(\vec{L}/2, 32)$, and $(\vec{0}, 48)$. Thus, each source is shifted by a displacement of $\vec{L}/2$. This layout of the sources is illustrated in Fig. 1.

We find that the individual measurements only exhibit minimal correlations, and thus this strategy provides a valuable increase of statistics; see Ref. [41] for a discussion of autocorrelations. We consistently apply binning with a bin size above ten which eliminates residual autocorrelations from our data. Below we study whether this technique introduces any systematic errors into our calculation.

B. Tests for systematic errors

We have performed tests concerning three possible sources of systematic errors: The coherent sink scheme described in the previous section, the choice of boundary conditions in the temporal direction, and the choice of the source-sink separation, T_0, which is an important input parameter entering any three-point function calculation.[2] Following Eq. (14) it is advisable to pick T_0 as large as possible. However, if T_0 becomes too large, the two-point function in the ratio Eq. (15) introduces an increasing noise that will eventually wipe out the signal. Thus, T_0 should be chosen such that we are still able to project out the ground state in a suitably chosen plateau region, but not so large that the signal-to-noise ratio becomes too bad.

From previous calculations (cf. e.g. [20]), we know that a separation of $T_0 \simeq 1.2$ fm is a reasonable choice. Our tests of this assumption, together with the other characteristics of our calculation mentioned above, are summarized in Fig. 2. The labels for the calculations denoted on the abscissa are explained in Table III. The gauge fields are a sample of 448 configurations at the working point $m_{\rm sea}^{\rm asqtad} = 0.010/0.050$ on the 20^3 lattice; cf. Table I. The technique employed in our previous publication, Ref. [20], corresponds to the label "E"; cf. Table III. To address whether the chopping prescription—to cut the lattice into two halves, impose Dirichlet boundary conditions, and compute observables on both halves separately—employed in that publication introduces a systematic error, we have repeated the calculation on the unchopped lattice. This case is denoted by label "D." It is evident that the results are essentially identical for both the axial charge and the mean squared radius. We thus conclude that the chopping prescription did not introduce any systematic error.

Next, using the same sample of configurations we performed eight independent calculations of propagators on the lattice with locations identical to those chosen for the coherent propagators; cf. Sec. III A. This case is denoted by "A." It is evident that the statistical improvement is remarkable, indicating that the results are sufficiently decorrelated to warrant the extra effort.

The true power of the coherent sink technique is demonstrated by case "B." The computational requirements for the backward propagators are just 1/4 of those of case A, yet the result is almost identical and completely consistent. This gives us further confidence that our technology is indeed correct.

Finally, we also compare the two source-sink separations, $T_0 = 9$ and $T_0 = 10$, the latter denoted by case "C." There is an increase of about 50% in the error bar between case B and case C, but the results are fully compatible within error bars. This indicates that a separation of $T_0 = 9$ is already sufficient to extract the ground state, and higher-state contaminations are negligibly small. We thus proceed

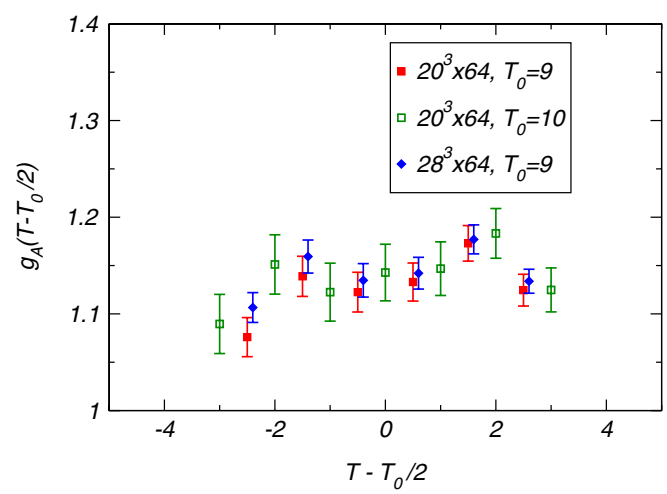

FIG. 3 (color online). Comparison of two separations on two volumes for the isovector axial charge, g_A. This plot shows the resulting plateau plot, i.e. $g_A(T)$ as a function of the location of the operator insertion at fixed source-sink separation.

[2]The issue of finite-size effects is addressed separately in Sec. III E

to use the method denoted by B for the remainder of this publication.

To illustrate the result from different source-sink separations and to make sure that excited state contributions are small, we also show a plateau plot for one of our observables. Figure 3 shows the isovector axial charge, g_A, as a function of the location of the operator insertion prior to averaging over the plateau region. The plateau is flat up to $\mathcal{O}(a^2)$ cutoff effects for any T_0 since the operator corresponds to a conserved charge. If we had to suspect contamination from excited state contributions, the overall level of the plateau would be systematically different from the corresponding ones using the $T_0 = 9$ separation. We do not observe such a systematic effect and thus conclude that going to the smaller separation does not introduce systematic uncertainties from excited states.

In summary, the new technology does indeed constitute a major improvement over the one previously employed in terms of statistical accuracy, but does not lead to a detectable increase in systematic error.

C. Superjackknife analysis and error correlation

When calculating physical observables and their uncertainties from different lattice data sets, we have to take into account the correlations of different data points with each other. It turns out that there are three possible cases we need to consider: (a) Observables calculated from data points computed on a single ensemble of lattice data. (b) Observables calculated from data points computed on several statistically independent ensembles of lattice data, where each ensemble contributes only a single data point. (c) Observables calculated from data points from different ensembles, where each ensemble contributes more than one data point. An example for case (a) is dipole fits to form factors, where each fit is done to a set of different Q^2 values at a fixed pion mass. Case (b) occurs for chiral fits to hadron masses [21] or moments of forward parton distributions [39]. Case (c) is the most complicated and shows up in simultaneous fits to (generalized) form factors as functions of both Q^2 (or of t in case of the GFFs) and m_π.

In case (a) we are dealing with data that may have correlations among data points. Case (b) has no correlation among different data points since the underlying gauge field configurations are entirely independent. Case (c) has data points that are correlated (those points obtained on the same sample of gauge field configurations) and others that are not correlated (those obtained on different samples of configurations). Although in case (c) the error-correlation matrix will be strictly block diagonal, a straightforward numerical estimation may not take this property into account. In particular, the off-diagonal entries in the error-correlation matrix may have large uncertainties themselves and thus introduce numerical instabilities.

In this paper, we have decided to consistently adopt the jackknife method to compute uncertainties and to use the error-correlation matrix in the function χ^2 where it does not introduce numerical instabilities. The standard jackknife error prescription is well known and discussed widely in the literature; see e.g. [42,43]. We briefly summarize the method for an observable with exact statistical mean A as follows: given a series of measurements $\{a_i\}$, $i = 1, \ldots, N$, with N being the total number of measurements, a_i being the ith measurement we define the ith jackknife average via

$$\bar{a}_i = \frac{1}{N-1} \sum_{j=1, i\neq j}^{N} a_j. \tag{16}$$

Thus, we obtain a new set of N jackknife averages, $\{\bar{a}_i\}$. The natural estimator for A reads $\bar{a} = \frac{1}{N}\sum_{i=1}^{N} \bar{a}_i$ in terms of the $\{\bar{a}_i\}$. More generally, for any function $f(A)$ of the observable, the set of N jackknife blocks provides an estimate of the mean $\bar{F}$,

$$\bar{F} = \frac{1}{N} \sum_{i=1}^{N} f(\bar{a}_i), \tag{17}$$

as well as an estimator for its uncertainty,

$$\sigma_F^2 = \frac{N-1}{N} \sum_{i=1}^{N} (f(\bar{a}_i) - f(\bar{a}))^2. \tag{18}$$

Note that this method also generalizes to the case of a function of several observables, labeled by a Greek index, with expectation values A_α, $\alpha = 1, \ldots, n$. Again, this topic has been widely discussed in the literature, including in our previous studies; see e.g. [22]. As an important example, we describe the case of a fit to several observables. The function that we minimize in a nonlinear fit to n different lattice measurements is given by

$$\chi_i^2 = \sum_{\alpha=1}^{n} \sum_{\beta=1}^{n} (y_\alpha(\{x\}) - \bar{a}_{\alpha,i})(y_\beta(\{x\}) - \bar{a}_{\beta,i}) C^{-1}_{\alpha\beta}, \tag{19}$$

where $y_\alpha(\{x\})$ is a model function with parameters $\{x\}$ and a possible dependence on the index α. The covariance matrix $C_{\alpha\beta}$ is defined by

$$C_{\alpha\beta} = \frac{N-1}{N} \sum_{i=1}^{N} (\bar{a}_\alpha - \bar{a}_{\alpha,i})(\bar{a}_\beta - \bar{a}_{\beta,i}). \tag{20}$$

For each configuration with number i we substitute the jackknife averages $\bar{a}_{\alpha,i}$ and minimize χ_i^2 w.r.t. the parameters $\{x\}$. The parameter values which minimize Eq. (19) are thus implicit functions of the original data set. Finally, we use Eqs. (17) and (18) on the resulting set of parameters to obtain estimates of their central values and of their statistical uncertainties.

As a special case, we consider the case of a dipole fit at fixed pion mass, where each $a_{\alpha,i}$ denotes the form-factor measurement on the ith jackknife block at momentum transfer Q_α^2, and the function $y_\alpha(M_d, A_0) = A_0/(1 + Q_\alpha^2/M_d^2)^2$ in Eq. (19) is the dipole model function; cf. Equation (37) below, the parameters being the dipole mass, M_d, and the overall normalization, A_0. The best fit

parameters are obtained from a minimization of the associated function χ^2 for all jackknife blocks in the sample, and we get the results by using Eqs. (17) and (18), where the function $f(\{A_\alpha\})$ denotes either M_d or A_0.

As has been mentioned previously, it may happen that the off-diagonal elements of $C_{\alpha\beta}$ are only poorly determined and the resulting inverse has zero or negative eigenvalues. In that case, the function χ^2 is not positive definite and the problem is ill defined. If this happens, we have to resort to simply using the diagonal matrix elements of $C_{\alpha\beta}$ and the method reduces to the regular, uncorrelated fit. We point out that even in this case the statistical error associated with this procedure is correctly estimated by the jackknife method, Eq. (18).

We also want to point out that each measurement can be taken from a single gauge field configuration or obtained as an average of a small set of B subsequent configurations. In the latter case, the jackknife procedure corresponds to what is called "jackknife with block-size B" in Ref. [43]. To summarize, the jackknife method allows us to compute functions of averages obtained on a given ensemble. The estimation of the uncertainty in Eq. (18) correctly takes into account correlations among the input data.

When we are dealing with a function of several observables computed on different ensembles, the method needs to be generalized further. In order to take the particular features of such a "supersample" containing both correlated and uncorrelated data into account, we use an extension of the jackknife method, called "superjackknife" [44,45]. The idea is to define generalized (super)jackknife blocks, with which averages and errors can still be estimated using Eqs. (17) and (18). To illustrate this procedure we start with M distinct, uncorrelated ensembles with N_k samples available in the kth ensemble. On these ensembles we again have a set of measurements, $\{a^{(k)}_{\alpha,i}\}$, which denotes the measurement on the ith sample of the kth ensemble. The averages $\bar{a}^{(k)}_\alpha = 1/N_k \sum_{i=1}^{N_k} a^{(k)}_{\alpha,i}$ and the jackknife blocks $\bar{a}^{(k)}_{\alpha,i}$ are introduced as in Eq. (16) above. The total number of superjackknife blocks is defined by $N = \sum_{k=1}^{M} N_k$. With appropriate superjackknife blocks $\{\tilde{a}^{(k)}_{\alpha,i}\}$ we can generalize Eq. (19) to

$$\chi_i^2 = \sum_{k=1}^{M}\sum_{\alpha=1}^{n^{(k)}}\sum_{\beta=1}^{n^{(k)}} (y^{(k)}_\alpha(\{x\}) - \tilde{a}^{(k)}_{\alpha,i})(y^{(k)}_\beta(\{x\}) - \tilde{a}^{(k)}_{\beta i})(C^{(k)})^{-1}_{\alpha\beta}, \tag{21}$$

where we introduce the notation $n^{(k)}$ for the number of observables in the kth ensemble. The index i now denotes the number of the superjackknife block, $i = 1, \ldots, N$. The N superjackknife blocks $\tilde{a}^{(k)}_{\alpha,i}$, i.e. the N sets of arguments at which the function is to be evaluated, are constructed as follows. The first N_1 blocks consist of

$$\tilde{a}^{(k)}_{\alpha,i} = \begin{cases} \bar{a}^{(k)}_{\alpha,i}: k = 1 \\ \bar{a}^{(k)}_{\alpha}: k \neq 1 \end{cases} \quad \text{with} \quad i = 1, \ldots, N_1, \quad k = 1, \ldots, M, \quad \alpha = 1, \ldots, n^{(k)}. \tag{22}$$

The following N_2 blocks consist of

$$\tilde{a}^{(k)}_{\alpha,i+N_1} = \begin{cases} \bar{a}^{(k)}_{\alpha,i}: k = 2 \\ \bar{a}^{(k)}_{\alpha}: k \neq 2 \end{cases} \quad \text{with} \quad i = 1, \ldots, N_2, \quad k = 1, \ldots, M, \quad \alpha = 1, \ldots, n^{(k)}, \tag{23}$$

and so on. This generalization takes the correlations within each ensemble correctly into account, while at the same time implicitly sets correlations among different ensembles to zero. It is evident that it reduces to the regular jackknife method, Eq. (16), in the case of a single ensemble.

A typical case that the superjackknife method can be applied to is the fit of a form factor which has been expanded simultaneously in m_π and Q^2 to all available lattice data; see e.g. the small-scale expansion (SSE) formula in Eq. (43). The function $y^{(k)}_\alpha(c_A, B^r_{10}(\lambda)) = y(c_A, B^r_{10}(\lambda); m^{(k)}_\pi, (Q^{(k)}_\alpha)^2)$ in Eq. (21) is the form-factor model function and Eqs. (22) and (23) collect all form-factor data on the ensembles with different pion masses, $m^{(k)}_\pi$, and at different $(Q^{(k)}_\alpha)^2$ values. Note that the values of Q^2 on each ensemble are different in general since both the lattice volumes and the nucleon masses are different. After N minimizations to the supersamples, we obtain all parameters—in our example the low-energy constants c_A and $B^r_{10}(\lambda)$—by virtue of Eqs. (17) and (18) from the resulting set of best fit parameters.

In order to ascertain that results obtained with the superjackknife method are compatible with those obtained with competitor schemes, like the bootstrap resampling plan, which has, e.g., been employed in Ref. [21], we have made a detailed comparison between the two methods based on fits to our data for the nucleon axial charge, g_A. Figure 4 shows a comparison of two fits to g_A, one based on the three smallest pion masses and one based on the four smallest pion masses, corresponding, respectively, to the upper panels and the lower panels of the figure. The two left plots show error bands determined from the bootstrap resampling method, and the two right plots show results from the superjackknife prescription. The technical details and results will be discussed later in Sec. IVA, we use this fit merely as a test to verify that the bootstrap and the superjackknife methods give indistinguishable error bands in the two situations. We point out that the case with three masses is a "bad" fit with large uncertainties and the case with four masses has substantially smaller uncertainties and provides a much better fit. We conclude that the two resampling schemes give essentially identical error estimates and are thus equally applicable, both in fits with large and in fits with small uncertainties.

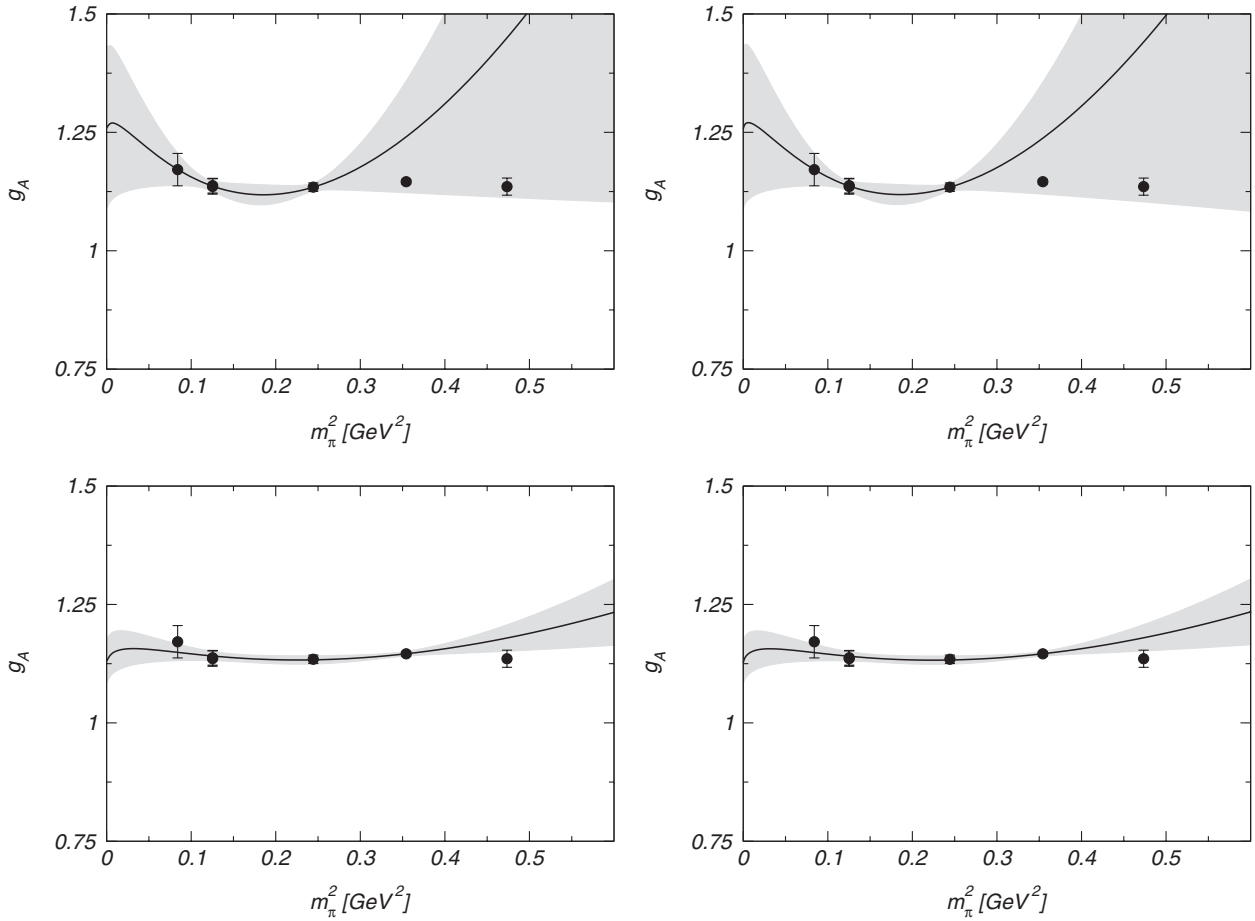

FIG. 4. Comparison of bootstrap (left panels) and superjackknife (right panels) resampling plans for chiral fits to the nucleon axial charge, g_A. The upper two plots show fits to the lowest three masses, the lower two show fits to the lowest four masses.

The error-correlation matrix also allows us to study a phenomenon about lattice data that looks puzzling when one assumes that data points at distinct momentum transfers Q^2 are independent. In this paper we will plot a couple of those cases; see e.g. Fig. 25 below. A couple of data points are systematically higher; they are off by more than 1 standard deviation from the central fit. If these points were independent measurements, it would be a highly significant deviation. Thus, the question is whether these six points are highly correlated so that only one or 2 degrees of freedom have fluctuated randomly. Using the technology of error correlations presented in this section we have addressed this phenomenon in detail in Ref. [41]. We have found that the correlation of such data points is very high, typically (80–90)%. On the other hand, the resulting χ^2/dof is still around 1 which proves that such "outliers" are not statistically significant, although a naive visual analysis would lead to the erroneous conclusion that the data are incompatible with the fit function. In this way the treatment of error correlations as implemented in this work is absolutely necessary to derive conclusive statements about the statistical quality of fits to lattice data points.

D. Renormalization of lattice operators

The matrix elements we compute numerically are in the lattice regularization at a scale of the lattice cutoff, $\mu^2 = a^{-2}$. In order to compare them to experiment, we need to convert them to a commonly used scheme. When the renormalization is multiplicative, the conversion is done via

$$\langle \mathcal{O}^{\mathrm{cont}} \rangle = Z_{\mathcal{O}} \langle \mathcal{O}^{\mathrm{latt}} \rangle, \tag{24}$$

$\langle \mathcal{O}^{\mathrm{cont}} \rangle$ being the matrix element in the $\overline{\mathrm{MS}}$ scheme and $\langle \mathcal{O}^{\mathrm{latt}} \rangle$ the bare lattice operator. The factor $Z_{\mathcal{O}}$ is the renormalization constant which depends on the details of the lattice action and the operator, but not the external states of the matrix element.

Since on the lattice all operators are representations of the finite hypercubic group $H(4)$, there will necessarily be fewer operators than in the continuum group, $O(4)$. This means that, in general, continuum operators correspond to linear combinations of a finite set of lattice operators and the right-hand side of Eq. (24) is replaced by a sum containing operators of different dimensions. In such a

situation, computing renormalization coefficients will be impractical since subtracting power-law divergences nonperturbatively is required. It is possible, however, to compute the coefficients if operators of different dimensions do not mix—in the case of the operators appearing in Eq. (4), this requires choosing distinct indices, which is only possible for operators with at most four indices. Hence, our lattice technology limits us to the computation of only the lowest moments of (generalized) parton distributions.

We apply the perturbative renormalization constants computed in Ref. [46]. We have employed them previously in [20]. All the perturbative coefficients relevant to this work are listed in Table IV, together with the representation of $H(4)$. In addition, we also obtain renormalization constants for the electromagnetic and axial currents nonperturbatively; see Table V in Sec. IV B and Table XXXIII in Sec. IV C. In particular, the wave-function renormalization encoded in the axial current renormalization factor Z_A implicitly enters most of the operators we study and is not small; therefore, it is desirable to determine this one common factor nonperturbatively and employ the same recipe as in [20], namely,

$$Z_{\mathcal{O}} = \frac{Z_{\mathcal{O},\mathrm{pert}}}{Z_{A,\mathrm{pert}}} \cdot Z_{A,\mathrm{nonpert}}, \tag{25}$$

with $Z_{A,\mathrm{pert}} = 0.964$ for all but the vector and axial currents. The numerical results in this paper are all transformed to the $\overline{\mathrm{MS}}$ scheme at the scale of $\mu^2 = 4\ \mathrm{GeV}^2$.

We note that an ongoing analysis of *nonperturbative* renormalization constants employing the Rome-Southampton scheme [47] turns out to be challenging due to discretization effects and the restricted range of applicability of the perturbative scale evolution. From our preliminary results [48], we can, however, obtain a numerical estimate of the potential systematic uncertainty due to the renormalization of the one-derivative operators, which is $\approx 7\%$. We include this systematic uncertainty in our final results in Table XLIV.

TABLE IV. Perturbative renormalization constants to convert bare matrix elements to the scale $\mu = a^{-1}$ in the $\overline{\mathrm{MS}}$ scheme.

Operator	$H(4)$	$Z_{\mathcal{O}}^{\mathrm{pert}}$
$\bar{q}[\gamma_5]\gamma_{\{\mu}D_{\nu\}}q$	$\tau_1^{(3)}$	0.962
$\bar{q}[\gamma_5]\gamma_{\{\mu}D_{\nu\}}q$	$\tau_1^{(6)}$	0.968
$\bar{q}[\gamma_5]\gamma_{\{\mu}D_{\nu}D_{\rho\}}q$	$\tau_1^{(4)}$	0.980
$\bar{q}[\gamma_5]\gamma_{\{\mu}D_{\nu}D_{\rho\}}q$	$\tau_1^{(8)}$	0.982

TABLE V. Renormalization constant of the vector currents.

$m_{\mathrm{sea}}^{\mathrm{asqtad}}$	Volume	Z_V
0.007/0.050	$20^3 \times 64$	1.1159
0.010/0.050	$28^3 \times 64$	1.1169
0.010/0.050	$20^3 \times 64$	1.1206
0.020/0.050	$20^3 \times 64$	1.1351
0.030/0.050	$20^3 \times 64$	1.1464

E. Finite-volume effects

It is important to assess the potential influence of finite-volume effects on our observables. Our calculations are done in a fixed physical volume; hence we expect the finite-volume effects to increase as the pion mass decreases. Since at the working point $m_{\mathrm{sea}}^{\mathrm{asqtad}} = 0.010/0.050$ we have two volumes at our disposal, 20^3 and 28^3, corresponding, respectively, to $(2.5\ \mathrm{fm})^3$ and $(3.5\ \mathrm{fm})^3$, we have a way to estimate the size of these effects at a fixed pion mass of 356 MeV.

We start with the simplest quantity, namely, the mass of the nucleon. Figure 5 displays the mass plateau on the two volumes, together with the band from fitting the two-point correlators with the function [9]

$$C_{2\mathrm{pt}}(t) = Z_0^{-m_N t} + Z_1 e^{-m_{N,\mathrm{exc}} t} + (-1)^t Z_{\mathrm{osc}} e^{-E_{\mathrm{osc}} t} \tag{26}$$

in range $2 \le (t/a) \le 15$. The same source is used on both volumes, and the effective mass is extremely similar. Fits to the mass plateau yield the result

$$m_\pi = 356\ \mathrm{MeV}: \quad |1 - m_N(L = 2.5\ \mathrm{fm})/m_N(L = 3.5\ \mathrm{fm})| < 1.8\% \quad (95\%\ \mathrm{conf.\ lev.}). \tag{27}$$

As a consequence, in extrapolations carried out throughout this paper, we will use a common value of the nucleon mass for both volumes. Second, Fig. 3, used earlier to illustrate the source-sink separation dependence, also compares the plateau plot for g_A on the 20^3 and the 28^3 lattices. The whole function $g_A(T)$, where T is the source-operator separation, is strikingly similar between the two volumes. We will return to this fact in Sec. IV A dedicated to g_A.

Figure 6 shows the isovector Dirac radius, $\langle r_1^2 \rangle$ extracted from a dipole fit to the form factor $F_1^v(Q^2)$, as a function of the pion mass, m_π. These observables will be discussed in

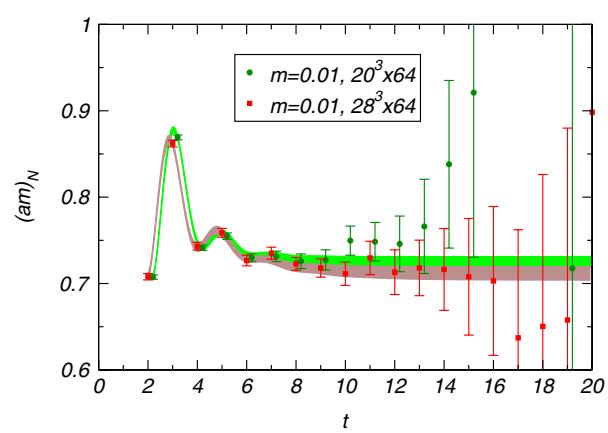

FIG. 5 (color online). Mass plateau at $am = 0.010$ on the 20^3 and the 28^3 lattices. The band corresponds to Eq. (26).

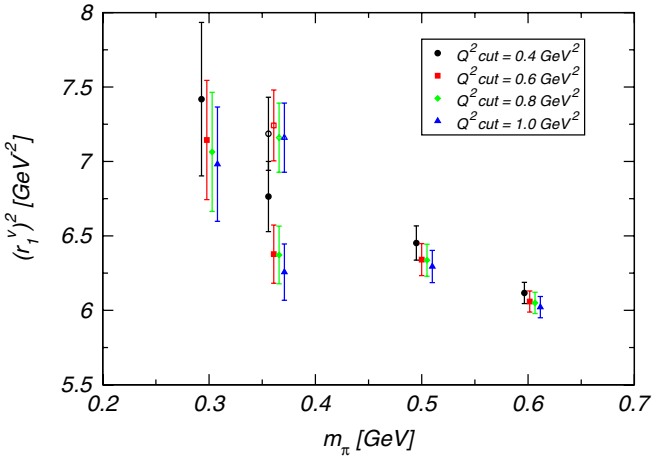

FIG. 6 (color online). Isovector Dirac radius $\langle r_1^2 \rangle$ as a function of the pion mass for all ensembles.

detail in Sec. IV B; here we only wish to exhibit the finite-size effects. The upper cutoff in Q^2 for the dipole fit has been varied and the results for different cutoffs have been drawn with a slight displacement for clarity. At the pion mass of $m_\pi = 356$ MeV, there is a discrepancy outside the error bars between the two volumes. However, when reducing the data set to Q^2 values below 0.4 GeV^2, we find that the two Dirac radii are actually compatible. The discrepancy becomes apparent only at data points beyond $Q^2 > 0.4$ GeV^2.

When studying the isovector form factor $F_2^v(Q^2)$, we obtain the Pauli radii, $\langle r_2^2 \rangle$, and the anomalous magnetic moments, κ_v, shown in Fig. 7. Also these observables will be discussed in detail in Sec. IV B; here we again wish to exhibit only the finite-size effects. As in the previous plot, we have applied dipole fits with varying upper cutoff in Q^2. Again, we find that there is a notable discrepancy for $\langle r_2^2 \rangle$

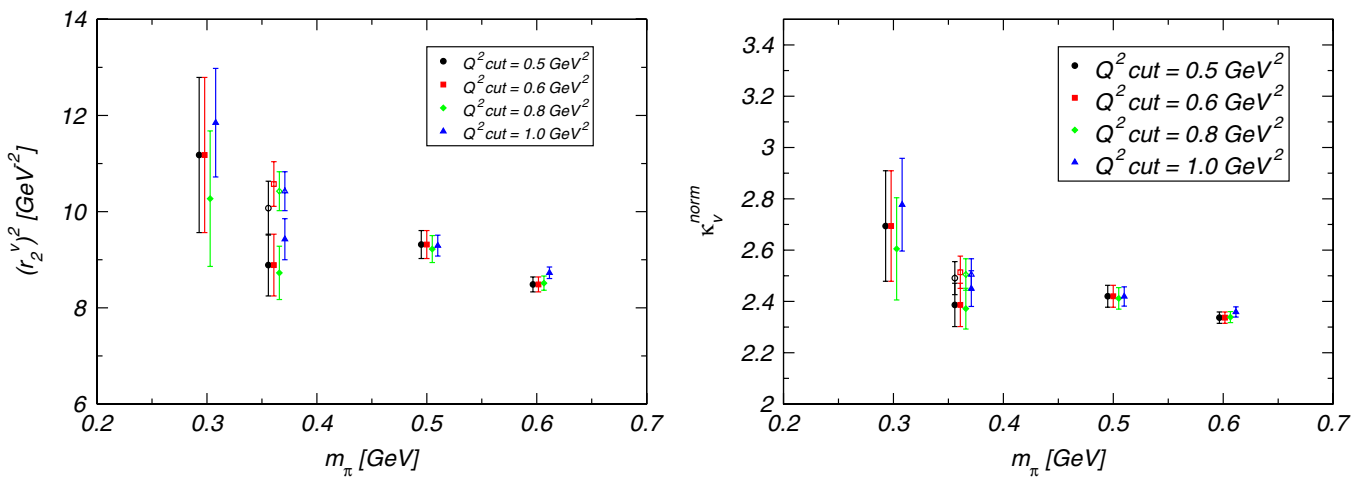

FIG. 7 (color online). Isovector Pauli radius, $\langle r_2^2 \rangle$, and anomalous magnetic moment, $\kappa_v^{\rm norm} \equiv \frac{m_N^{\rm phys}}{m_N(m_\pi)} F_2^v(0)$, as a function of the pion mass for all ensembles.

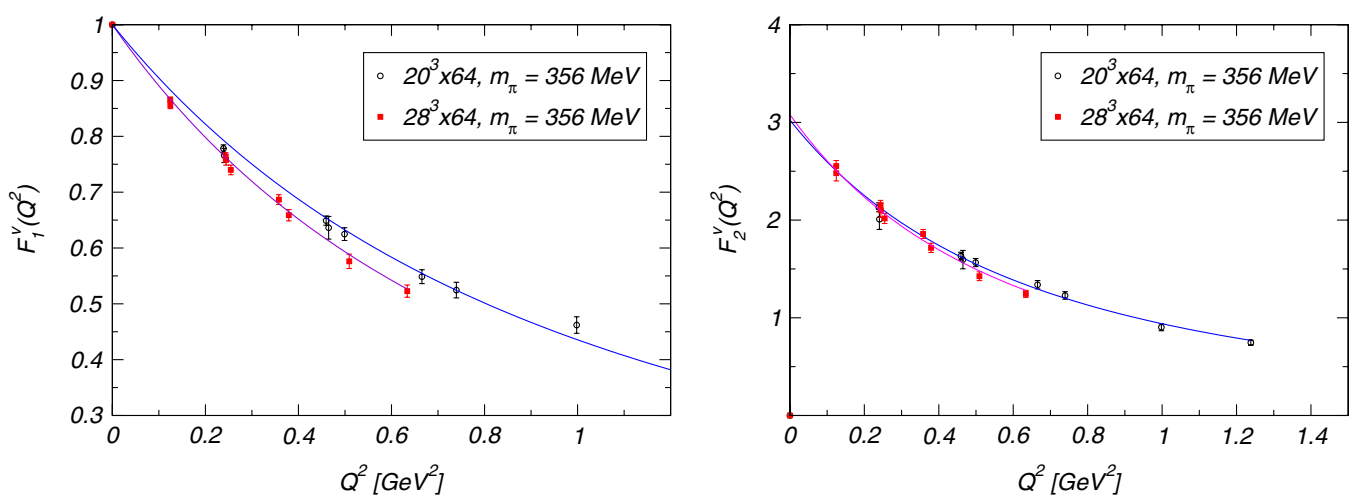

FIG. 8 (color online). Direct comparison of finite-volume effects for the isovector form factors, $F_1^v(Q^2)$ and $F_2^v(Q^2)$, at $m_\pi = 356$ MeV on the two volumes $\Omega = 28^3 \times 64$ and $\Omega = 20^3 \times 64$.

when data points at $Q^2 > 0.4$ GeV^2 are included in the plot. For κ_v we find that the results on the two volumes deviate systematically, but are still compatible taking into account their statistical uncertainty.

We can also scrutinize this behavior by looking at the form factors as a function of Q^2 directly and compare the location of the points on the two volumes. Figure 8 shows this comparison. The solid curves are dipole fits to all available data points. It is evident that their dipole masses are different, but the data points at small Q^2 are identical. The difference in curvature is caused only by points beyond that.

We conclude that we observe finite-size effects in our lattice form-factor data. However, the finite-size effects are significant only for intermediate values of Q^2. Based on the smallest values of Q^2, the Dirac and Pauli radii may be identical on both volumes. We did not find a satisfactory explanation based on chiral expansions or models at this point and leave this matter for future investigations.

As a final remark, in Sec. IV D we will compare the radii defined by the generalized form factors. There we will also find suggestive evidence that the mass radius is larger on the larger volume. Here our intention was to illustrate our observation of finite-volume effects with the data that are most accurate.

IV. RESULTS

A. The axial charge

In this section we present new data on the nucleon axial charge g_A. Although axial form factors are discussed in more depth below in Sec. IV C, the fundamental phenomenological importance of the axial charge warrants highlighting our new results for this observable already at this point. Aside from the changes in technology described in Sec. III, our calculation follows closely the methods of Ref. [4]. In particular we use the local axial current for the calculation, and the five-dimensional axial current is used to determine the normalization of the local current, as described in detail at the beginning of Sec. IV C.

The new data are displayed in Fig. 9. The value of g_A is remarkably independent of the pion mass, and lies at a value (8–10)% lower than the experimental value of 1.2695(29), while statistical errors are less than 2%. A naive extrapolation linear in m_π^2 of the $m_\pi < 500$ MeV data leads to $g_A(m_\pi) = 1.153(28)$. We will discuss below what difference more sophisticated chiral effective theory fits make.

It is worth describing to what extent the situation has changed since the calculation [4]. In the latter, less accurate calculation, the lattice data also showed a very mild pion-mass dependence. Using a 3-parameter fit based on the leading one-loop pion-mass dependence in the SSE at finite-volume leads to the value $g_A(m_\pi = 140\ \text{MeV}) = 1.226(84)$. The finite-volume effects predicted by the formula at the simulation points were found to be negligible compared to the statistical errors. The largest pion mass included in the fit was 760 MeV, and the lightest 356 MeV.

Thanks to the new, higher statistics data, we control the finite-volume effects to a higher level of accuracy. Indeed, fitting the 20^3 and 28^3 g_A plateau at $am = 0.010$ (see Fig. 3) leads to the bound

$$m_\pi = 356\,\text{MeV}: \quad |g_A(L = 3.5\,\text{fm}) - g_A(L = 2.5\,\text{fm})| < 0.045 \quad (95\%\,\text{conf. lev.}). \tag{28}$$

To further tighten this statement, we want to constrain the possibility that the plateau for g_A could be affected by different excited state contributions on the two volumes. Indeed, even if the nucleon mass has a weak volume dependence for $L \geq 2.5$ fm [see Eq. (27)], the energy of the first excited state in that symmetry channel could *a priori* have a significant volume dependence: in large volume we expect it to be a nucleon and a pion with a nonvanishing relative momentum. However, comparing the local effective mass on the 20^3 and 28^3 lattices, Fig. 5, we see good agreement between them (the same

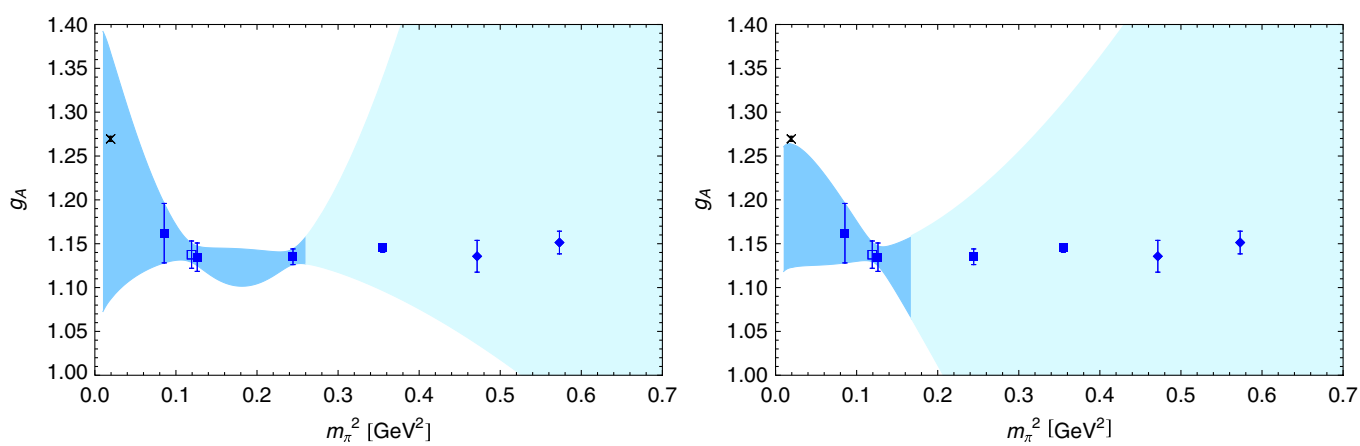

FIG. 9 (color online). SSE fit to the axial charge. Left: three-parameter fit with $m_\pi < 500$ MeV. Right: two-parameter fit with $m_\pi < 360$ MeV.

nucleon interpolating operator is used on both volumes). We conclude that the contamination of the first excited state does not increase significantly with the volume. In particular, the bound (28) on the g_A finite-size effects is robust. While a nonmonotonic volume dependence of g_A that would make the difference in Eq. (28) accidentally small cannot be excluded, this bound strongly constrains how much of the discrepancy between the lattice data and the experimental value of g_A can be attributed to finite-volume effects.

As mentioned above, a naive extrapolation linear in m_π^2 of our lattice data leads to values of $g_A(m_\pi)$ about 10% lower than the phenomenological value. We now proceed with the fit ansatz provided by the SSE framework [50],

$$\begin{aligned} g_A(m_\pi) = g_A &- \frac{g_A^3 m_\pi^2}{16\pi^2 f_\pi^2} + 4m_\pi^2\Bigg\{C(\lambda) + \frac{c_A^2}{4\pi^2 f_\pi^2} \\ &\times\left[\frac{155}{972}g_1 - \frac{17}{36}g_A\right] + \gamma\log\frac{m_\pi}{\lambda}\Bigg\} + \frac{4c_A^2 g_A}{27\pi f_\pi^2\Delta}m_\pi^3 \\ &+ \frac{8c_A^2 g_A m_\pi^2}{27\pi^2 f_\pi^2}\left[1 - \frac{m_\pi^2}{\Delta^2}\right]^{1/2}\log R(m_\pi) + \frac{c_A^2\Delta^2}{81\pi^2 f_\pi^2} \\ &\times(25g_1 - 57g_A)\Bigg\{\log\frac{2\Delta}{m_\pi} - \left[1 - \frac{m_\pi^2}{\Delta^2}\right]^{1/2} \\ &\times\log R(m_\pi)\Bigg\}, \end{aligned} \tag{29}$$

with g_1 the axial-delta-delta coupling, c_A the axial-nucleon-delta coupling, and Δ denoting the delta-nucleon mass splitting, in the chiral limit. Following [50], we define the function

$$R(m) = \frac{\Delta}{m} + \sqrt{\frac{\Delta^2}{m^2} - 1}. \tag{30}$$

When the Δ baryon is below threshold, as is the case in our lattice calculations, $\sqrt{\Delta^2 - m_\pi^2}\log R(m_\pi)$ is substituted by $-\sqrt{m_\pi^2 - \Delta^2}\arccos(\Delta/m_\pi)$. A three-parameter SSE fit to our data at pion masses below 500 MeV with a fixed value of $c_A = 1.5$—a motivation for this choice is given in Ref. [9]—gives (see left panel of Fig. 9),

$$g_A^0 = 1.22(17), \qquad g_1 = 3.9(3.0). \tag{31}$$

The result thus does increase as the pion mass is lowered, but becomes consistent only with the phenomenological value by virtue of its uncertainty also rising significantly. As an alternative, we perform a two-parameter fit to $m_\pi <$ 360 MeV, where we fix the value of g_1 to 2.5, close to the $SU(4)$ spin-flavor quark symmetry prediction $9/5g_A$. This fit is illustrated on the right panel of Fig. 9. Here the result for g_A is slightly lower than in the three-parameter fit, and the error bar barely extends to the phenomenological value.

As has already been mentioned above, our previous calculation of g_A in Ref. [4] included data points at larger pion masses in the fit—as a result of which it has a smaller statistical uncertainty for the extrapolated value. Another calculation in Ref. [5] contains only pion masses larger than 500 MeV. A discussion of the range of validity of one chiral expansion scheme in Ref. [51] concludes that lattice data below pion masses of 300 MeV are necessary for a reliable prediction. Reference [52] observes a bending down of the extrapolation due to the data point at the smallest available pion mass in that calculation, $m_\pi =$ 331 MeV. This is above our smallest mass. However, our smallest pion-mass data point has a larger error bar and is just consistent with the one from Ref. [52]; it may be the case that at this parameter the data are already affected by finite-volume effects—a possibility also mentioned in that paper. This interpretation is supported by the observation that the other data points at larger pion masses tend to be systematically higher than our data points. However, at our data point at $m_\pi = 356$ MeV we do not find any evidence of finite-volume effects which indicates that at lighter pion mass these effects would have to set in rather quickly.

While in the present work we find no significant evidence for a pion-mass dependence of g_A, our data are simultaneously compatible with the possibility that the functional form predicted by the small-scale expansion applies below $m_\pi = 350$ MeV and with the phenomenological value of g_A.

B. Electromagnetic form factors

The matrix element of the electromagnetic current between nucleon states can be parametrized in terms of two form factors. Common choices are the Dirac and Pauli form factors, $F_1(Q^2)$ and $F_2(Q^2)$, and the electric and magnetic Sachs form factors, $G_E(Q^2)$ and $G_M(Q^2)$. The former directly correspond to the form factors $A_{10}(Q^2)$ and $B_{10}(Q^2)$ from Eq. (6). The latter are related by a simple linear transformation to the isovector Dirac and Pauli form factors, $F_1^v(Q^2)$ and $F_2^v(Q^2)$:

$$G_E(Q^2) = F_1^v(Q^2) - \frac{Q^2}{(2m_N)^2}F_2^v(Q^2), \tag{32}$$

$$G_M(Q^2) = F_1^v(Q^2) + F_2^v(Q^2). \tag{33}$$

We will also use the standard notation for the anomalous magnetic moment of the nucleon in units of $e/2m_N(m_\pi)$,

$$\kappa_v = F_2^v(0). \tag{34}$$

When performing chiral fits we will work with

$$\kappa_v^{\rm norm} = \frac{m_N^{\rm phys}}{m_N(m_\pi)}\kappa_v, \tag{35}$$

which represents the isovector anomalous magnetic moment in units of the physical Bohr magneton, $e/2m_N^{\rm phys}$.

We use the ultralocal discretizations of the dimension three quark bilinear operators; i.e. their support is a single lattice site. Because of quantum effects the matrix elements of these lattice operators are not trivially renormalized, and we have to apply renormalization constants to them.

Since the forward matrix element $\langle p, \lambda | \bar{\psi} \gamma_\mu \psi | p, \lambda \rangle$ counts the total number of quarks of type ψ and this number is known by construction, we obtain Z_V by dividing the unrenormalized isovector current in the forward case. We point out that in the forward case the disconnected contribution is exactly zero since the disconnected operator cannot change the total number of quarks of any type. Thus, the value for Z_V obtained this way will be exact also if we consider disconnected contributions in future work. The resulting renormalization constants Z_V for the vector current are listed in Table V. The renormalization constants of the axial current are discussed later in Sec. IV C.

To study the charge distribution of the nucleon at large distances, it makes sense to consider the leading contribution of the form factors at small values of Q^2 [3]. The linear coefficient of the small-Q^2 expansion can serve as a measure of the nucleon size and is known as the mean squared radius, $\langle r_i^2 \rangle$, where i labels the different Lorentz and flavor structures one may consider:

$$F_i(Q^2) = F_i(0)(1 - \tfrac{1}{6} Q^2 \cdot \langle r_i^2 \rangle + \mathcal{O}(Q^4)). \tag{36}$$

The radii, $\langle r_i^2 \rangle$, can also be extracted from experiment. For a recent review see Ref. [53]. Although this is straightforward for the proton isovector $F_1^v(Q^2)$ form factor, a determination from fits to the experiment [54,55] turns out to be inconsistent with an analysis based on dispersion theory [56–58]. The latter radii are systematically larger than the former. To resolve this discrepancy, a dedicated experiment is currently being performed [59]. For the proton isovector $F_2^v(Q^2)$ a different discrepancy has been found in recent spin-transfer measurements [60–64]. The source of this mismatch is generally believed to be two-photon exchange processes [55], which is challenging to verify. On the lattice, we can study these observables without any two-photon contamination and thus make a significant contribution toward resolving the discrepancy.

Section IVB discusses the results for the form factors of the electromagnetic current. First, we study the isovector Dirac form factor $F_1^v(Q^2)$ in Sec. IV B 1 and the isovector Pauli form factor $F_2^v(Q^2)$ in Sec. IV B 2. The scaling behavior of form factors at larger values of Q^2 is shown in Sec. IV B 3. Section IV B 4 discusses the Sachs parametrization of form factors. Section IV B 5 discusses the slope of the ratio $F_1^d/F_1^u(Q^2)$ to learn about the flavor dependence of the form factors. The isoscalar form factors are shown in Sec. IV B 6. Section IV B 7 summarizes our findings. Where applicable, we compare the chirally extrapolated results to experiment.

1. Isovector Dirac form factor $F_1^v(Q^2)$

This section covers the isovector Dirac form factor, $F_1^v(Q^2)$. Phenomenologically, this form factor is commonly fit using a dipole form at fixed pion mass. We will thus first attempt to fit $F_1^v(Q^2)$ using the dipole form and study the stability of this fit as a function of the Q^2 range. Next, we will perform chiral fits using the SSE, Ref. [65], which includes explicit $\Delta(1232)$ degrees of freedom [66,67]. We will first compare the expansion applied to the Dirac radii, $\langle r_1^2 \rangle$, obtained from the previous dipole fits. We will then study the covariant baryon chiral perturbation theory expansion (BChPT) for the same quantity; see Refs. [9,68].

Finally, we will present SSE fits to the simultaneous Q^2 and m_π dependence of our lattice data. The latter method has the strong advantage that no reliance on the applicability of the dipole form is assumed. For these fits we apply the superjackknife and error-correlation matrix methods discussed in Sec. III C. Thus, we believe that this fit strategy is superior to the ones previously employed.

Dipole fits to isovector $F_1^v(Q^2)$.—

In this section we discuss the Q^2 dependence of the form factors at fixed values of the pion mass, m_π. The function we will use throughout this section is the dipole formula,

$$F_1^v(Q^2) = A_0/(1 + Q^2/M_d^2)^2, \tag{37}$$

with A_0 fixing the overall normalization and M_d being the dipole mass. From Eqs. (37) and (36) it is immediately obvious that the dipole mass is related to the Dirac radius of $F_1^v(Q^2)$ via

$$\langle r_1^2 \rangle = \frac{12}{M_d^2}. \tag{38}$$

In order to verify whether the functional form indeed allows for a meaningful application of the dipole formula, we have performed a series of fits in which we varied the fit interval $[Q^2_{\min}, Q^2_{\max}]$ and listed the variation of the fit parameters. We have restricted ourselves to the 28^3 lattice with pion mass $m_\pi = 356$ MeV. Results are summarized in Table VI. The table shows the fit interval used, the resulting value of χ^2/dof (degrees of freedom), the normalization A_0—which must be equal to one within precision due to the conservation of the vector current—and the dipole mass, M_d, together with the resulting Dirac radius, $\langle r_1^2 \rangle$. All error estimates have been obtained by applying the jackknife method to the minimization of the χ^2 including the error-correlation matrix, as discussed in Sec. III C. Table VI is divided into three blocks—first, the large-Q^2 cutoff is varied, next the small-Q^2 cutoff is varied, and finally the fit-interval window is moved along the available data set. Note that when one leaves out the small Q^2 values, the data point $F_1^v(0)$ is no longer included in the fit interval and A_0 can vary more.

The overall conclusion is that A_0 is always compatible with one within error bars and all results for M_d are consistent over the entire table. The former is an important internal consistency check, and the latter allows us to conclude that the dipole function is indeed an excellent description of the $F_1^v(Q^2)$ form factor over the entire range of available Q^2 values.

After performing similar fits at all available pion masses, we obtained the numbers compiled in Table VII. We have taken all available Q^2 values for each fit at fixed pion mass.

TABLE VI. Dipole fits to isovector $F_1^v(Q^2)$ with varying fit intervals on the 28^3 lattice with $m_\pi = 356$ MeV.

$[Q^2_{\min}, Q^2_{\max}]$ (GeV^2)	χ^2/dof	A_0	M_d (GeV)	$\langle r_1^2 \rangle$ (fm^2)
[0, 1.5]	1.22	1.0004(20)	1.299(21)	0.2770(92)
[0, 0.5]	1.09	9.9931(21)	1.298(23)	0.2774(97)
[0, 0.4]	1.27	9.9956(22)	1.293(23)	0.2797(99)
[0, 0.3]	1.52	9.9932(22)	1.287(22)	0.2820(98)
[0, 0.2]	2.43	1.0006(23)	1.276(24)	0.2870(11)
[0, 1.5]	1.22	1.0004(20)	1.299(21)	0.2770(92)
[0.1, 1.5]	1.23	0.9965(42)	1.305(22)	0.2744(93)
[0.2, 1.5]	0.72	0.9780(80)	1.338(25)	0.2611(97)
[0.3, 1.5]	0.90	0.9765(148)	1.339(31)	0.2605(120)
[0, 4, 1.5]	1.21	0.9445(354)	1.384(59)	0.2440(207)
[0.5, 1.5]	1.41	0.9469(692)	1.378(105)	0.2462(376)
[0.3, 0.5]	0.65	1.0098(499)	1.288(85)	0.2819(370)
[0.2, 0.4]	0.77	0.9749(117)	1.351(38)	0.2558(146)
[0.1, 0.3]	1.59	0.9948(47)	1.297(24)	0.2778(104)

TABLE VII. Dipole fits to isovector $F_1^v(Q^2)$ for all data sets.

m_π (MeV)	χ^2/dof	A_0	M_d (GeV)	$\langle r_1^2 \rangle$ (fm^2)
293	0.89	0.9983(73)	1.307(35)	0.2734(147)
356 on 28^3	1.22	1.0004(20)	1.299(21)	0.2770(92)
356 on 20^3	1.95	0.9999(15)	1.382(20)	0.2447(70)
495	1.57	0.9994(9)	1.3829(12)	0.2444(42)
597	3.76	0.9998(5)	1.4144(8)	0.2336(27)

Again, we have performed a combined error analysis with error-correlation matrix and jackknife. We find that the resulting values for the Dirac radii, $\langle r_1^2 \rangle$, are systematically smaller than the experimental value, $\langle r_1^2 \rangle^{\exp} = 0.637(12)$ fm^2 from Ref. [69]. We discuss possible resolutions of this discrepancy in the following by discussing chiral fits to our lattice data.

SSE fits to isovector $\langle r_1^2 \rangle$.—

As we have seen, the Dirac radius—and, consequently, the size of the nucleon—is lower than experiment at the pion masses we use. Hence, for a meaningful comparison the Dirac radii $\langle r_1^2 \rangle$ obtained in Table VII need to be extrapolated as a function of the pion mass, m_π. In this chapter we perform the chiral extrapolation using the SSE. The pion-mass dependence to next-to-leading order (NLO) is given by

$$\langle r_1^2 \rangle = -\frac{1}{(4\pi f_\pi)^2}\left(1 + 7g_A^2 + (10g_A^2 + 2)\log\left(\frac{m_\pi}{\lambda}\right)\right) - \frac{12B_{10}^r(\lambda)}{(4\pi f_\pi)^2} + \frac{c_A^2}{54\pi^2 f_\pi^2}\left(26 + 30\log\left(\frac{m_\pi}{\lambda}\right) + 30\frac{\Delta}{\sqrt{\Delta^2 - m_\pi^2}}\log\left(\frac{\Delta}{m_\pi} + \sqrt{\frac{\Delta^2}{m_\pi^2} - 1}\right)\right). \quad (39)$$

This expansion has a logarithmic divergence at $m_\pi \to 0$. Since the proton and the neutron are linear combinations of the isovector and isoscalar operators, the radius $\langle r_1^2 \rangle$ of either the proton or the neutron will similarly diverge in the chiral limit. In our fits we fix some of the parameters involved in the chiral expressions; see Table VIII. The axial coupling g_A in the chiral limit has been set equal to 1.2 according to Refs. [4,50,70]. The chiral limit values of f_π and the nucleon mass have been determined in Ref. [71] and Refs. [21,72,73], respectively. The delta-nucleon mass splitting Δ is taken equal to its physical value from the position of the delta resonance pole. Without any loss of generality, we set the regularization scale λ equal to 1 GeV. As input for our fits of $\langle r_1^2 \rangle$ we take the Dirac radii obtained from the dipole fits in Table VII. We perform a

TABLE VIII. Input parameters used for the chiral expansion.

Parameter	Value
g_A	1.2
c_A	1.5 or free parameter
f_π (MeV)	86.2
m_N (GeV)	0.8900
Δ (GeV)	0.2711
g_1	2.5

TABLE IX. NLO SSE fits to the isovector Dirac radii, $\langle r_1^2 \rangle$, obtained from dipole fits.

m_π max (MeV)	χ^2/dof	c_A	$B_{10}^r(1\ \mathrm{GeV})$
500	8.0	1.951(36)	1.713(78)
600	7.2	1.873(20)	1.557(48)

two-parameter fit with the counterterm $B_{10}^r(\lambda = 1\ \mathrm{GeV})$ and the coupling c_A. We vary the upper cutoff in m_π and collect the resulting fits in Table IX. The quality of the fits is not so good; we will see in Fig. 10 that the curvature of the SSE curve is stronger than that of the lattice data. Furthermore, the value of c_A tends to be larger than 1.5. One interpretation is that the range of validity of the SSE does not extend to our lattice data. On the other hand, if the smallest data point suffers from finite-size effects, it is still possible that the SSE is consistent with lattice data on a very large volume.

BChPT fits to isovector $\langle r_1^2 \rangle$.—

In the covariant baryon chiral perturbation theory (BChPT) scheme we use, the $\Delta(1232)$ degrees of freedom are not explicitly included while recoil corrections to the nonrelativistic heavy-baryon results, which correspond to

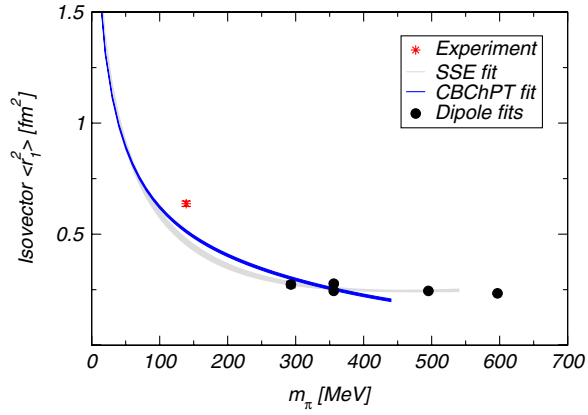

FIG. 10 (color online). Chiral fits to isovector Dirac radii, $\langle r_1^2 \rangle$, for $m_\pi < 500$ MeV (SSE) and $m_\pi < 400$ MeV (BChPT).

kinetic insertions in the nucleon propagator, are systematically resummed [74]. The chiral expansion of the $\langle r_1^2 \rangle$ Dirac radius is given by [68]

$$\langle r_1^2 \rangle = B_{c1} + (\langle r_1^2 \rangle)^{(3)} + (\langle r_1^2 \rangle)^{(4)} + \mathcal{O}(p^6). \tag{40}$$

The notation $(\langle \cdot \rangle)^{(M)}$ denotes the contribution of a quantity to the Mth order in the expansion in p^M. The specific expressions are

$$\begin{aligned}
B_{c1} &= -12 d_6^r(\lambda), \\
(\langle r_1^2 \rangle)^{(3)} &= -\frac{1}{16\pi^2 f_\pi^2 M_N^4}\left(7g_A^2 M_N^4 + 2(5g_A^2+1)M_N^4 \log\frac{m_\pi}{\lambda} + M_N^4 - 15 g_A^2 m_\pi^2 M_N^2 + g_A^2 m_\pi^2 (15 m_\pi^2 - 44 M_N^2)\log\frac{m_\pi}{M_N}\right) \\
&\quad + \frac{g_A^2 m_\pi}{16\pi^2 f_\pi^2 M_N^4 \sqrt{4M_N^2 - m_\pi^2}}(15 m_\pi^4 - 74 m_\pi^2 M_N^2 + 70 M_N^4)\arccos\frac{m_\pi}{2M_N}, \\
(\langle r_1^2 \rangle)^{(4)} &= -\frac{3c_6 g_A^2 m_\pi^2}{16\pi^2 f_\pi^2 M_0^4 \sqrt{4M_0^2 - m_\pi^2}}\left[m_\pi(m_\pi^2 - 3M_0^2)\arccos\frac{m_\pi}{2M_0} + \sqrt{4M_0^2 - m_\pi^2}\left(M_0^2 + (M_0^2 - m_\pi^2)\log\frac{m_\pi}{M_0}\right)\right].
\end{aligned} \tag{41}$$

The expression up to order $\mathcal{O}(p^4)$ introduces two fit parameters, $d_6^r(\lambda)$ and c_6. We set the scale of dimensional regularization λ equal to the value of the nucleon mass in the chiral limit, M_0. We point out that when only the third order in expansion (40) is considered, one should replace M_N by M_0 in Eqs. (41). In our fits, however, we consider only the full expansion at order $\mathcal{O}(p^4)$. Consequently, we are always using a pion-mass dependent form, $M_N(m_\pi)$, for M_N. Similar to Ref. [9] we use the expansion from Ref. [75] to model the functional form $M_N(m_\pi)$:

$$\begin{aligned}
M_N(m_\pi) = M_0 - 4c_1 m_\pi^2 &+ \frac{3g_A^2 m_\pi^3}{32\pi^2 f_\pi^2 \sqrt{4 - m_\pi^2/M_0^2}}\left(-4 + \frac{m_\pi^2}{M_0^2} + 4c_1\frac{m_\pi^4}{M_0^3}\right)\arccos\frac{m_\pi}{2M_0} - \frac{3m_\pi^4}{128\pi^2 f_\pi^2}\left(\left(\frac{6g_A^2}{M_0} - c_2\right)\right. \\
&\left. + 4\left(\frac{g_A^2}{M_0} - 8c_1 + c_2 + 4c_3\right)\log\frac{m_\pi}{\lambda}\right) + 4e_1^r(\lambda)m_\pi^4 - \frac{3c_1 g_A^2 m_\pi^6}{8\pi^2 f_\pi^2 M_0^2}\log\frac{m_\pi}{M_0},
\end{aligned} \tag{42}$$

with c_1, c_2, c_3, and $e_1^r(\lambda)$ being parameters that need to be fixed. In order to fix these constants we follow Ref. [9] again and pick the parameters c_2, c_3, and c_4 from the literature; cf. Refs. [73,76–79]. For M_0 we could adopt the chiral value m_N listed in Table VIII which we have used for the SSE. However, since the functional dependence on M_0 is highly complicated and all expressions can be sensitive to small changes in M_0, we decided to consider it a free

TABLE X. Low-energy constants involved in the chiral expansion of the nucleon mass up to NNLO. M_0, $e_1^r(1\ \mathrm{GeV})$, and c_1 are determined from a fit to lattice data and experiment.

M_0 (MeV)	$e_1^r(\lambda = 1\ \mathrm{GeV})$ (GeV^{-3})	c_1 (GeV^{-1})	c_2 (GeV^{-1})	c_3 (GeV^{-1})	c_4 (GeV^{-1})
876.6(17)	1.27(12)	−0.983(22)	3.2	−3.4	3.5

parameter and determine both M_0 and the remaining parameters c_1 and $e_1^r(\lambda)$ from a fit to the data points listed in Table II with pion masses $m_\pi < 500$ MeV. The physical nucleon mass is included in the fit. The resulting $\chi^2/\mathrm{dof} = 2.93$ is acceptable, and the parameters are in agreement with those reported in [9]. If we include all nucleon masses up to $m_\pi < 600$ MeV, the $\chi^2/\mathrm{dof} = 4.15$ increases slightly. Since we do not know the exact range of validity, we adopt the more conservative choice $m_\pi < 500$ MeV. When the experimental point is not included, the uncertainty of M_0 increases dramatically and becomes inconsistent with Ref. [9]. The results are summarized in Table X. As an alternative to Eq. (42) we may use an expression from Ref. [21]. It turns out, however, that the influence of different expansions of $M_N(m_\pi)$ on the radii is quite small.

There is one more subtlety that prevents a straightforward BChPT fit in the way it was possible for the SSE: The parameter c_6 in Eq. (41) appears only at $\mathcal{O}(p^4)$. The physical meaning of this low-energy constant is that of the chiral limit of the isovector anomalous magnetic moment. In order to gain statistics and better constrain our free parameters, we follow the prescriptions devised in Ref. [9] and perform a simultaneous fit to $\langle r_1^2\rangle$, $\langle r_2^2\rangle$, and κ_v in the BChPT scheme. This is done later in the BChPT part of Sec. IV B 2. Note that we restrict the joint fit to pion masses $m_\pi < 400$ MeV. The reason is that both $\langle r_1^2\rangle$ and $\langle r_2^2\rangle$ have a stronger curvature at larger pion masses than our lattice data and the χ^2/dof would be unacceptably large when pion masses beyond 400 MeV are included. We cannot exclude that the range of validity of the BChPT is smaller than that of the SSE. Figure 10 displays the results from the SSE fit (see Table IX) and the BCHPt fit (see Sec. IV B 2), with $m_\pi < 500$ MeV (for the SSE) and $m_\pi < 400$ MeV (for the BChPT) graphically. The experimental value in the graph is taken from Ref. [69]. Both curves are quite similar near the physical point. However, the lattice data are still quite flat for the available pion masses. Our lattice results do not give any indication of the divergence we should see approaching the chiral limit. We also remark that we observe a finite-volume dependence at $m_\pi = 356$ MeV of almost 12% if we perform dipole fits to all available Q^2, as discussed in Sec. III E. This effect could potentially increase rapidly at lower pion masses, and therefore the smallest $m_\pi = 293$ MeV data point could be too low. Thus, it is not excluded that the fit works well below 400 MeV if one had data at larger volume. At this point we observe that the effect goes in the right direction and is qualitatively consistent. For a conclusive statement, we still require more data at smaller pion masses and at larger volumes.

Simultaneous expansion fit to isovector $F_1^v(Q^2, m_\pi)$.— The dipole fits to $F_1^v(Q^2)$ discussed previously indeed provide an excellent description of the data over the entire range of available data. However, applying dipole fits suffers from the disadvantage that there is little fundamental justification for their usage. They are simply employed because they appear to work well. As an alternative strategy, we consider now the simultaneous chiral expansions in both m_π and Q^2. These expansions are expected to hold only for small values of Q^2 and m_π, but we can apply them to our entire data set, i.e. by combining data from several different ensembles at different m_π values in the same chiral fit without model-dependent assumptions on the functional form.

In the following, we present results from the application of the expression from Ref. [67] to the isovector form factor $F_1^v(Q^2, m_\pi)$:

$$F_1^v(Q^2, m_\pi) = 1 + \frac{1}{(4\pi f_\pi)^2}\Bigg(-Q^2\Bigg[\frac{68}{81}c_A^2 - \frac{2}{3}g_A^2 - 2B_{10}^r(\lambda) + \Bigg(\frac{40}{27}c_A^2 - \frac{5}{3}g_A^2 - \frac{1}{3}\Bigg)\log\Bigg(\frac{m_\pi}{\lambda}\Bigg)\Bigg] + \int_0^1 dx\Bigg[\frac{16}{3}\Delta^2 c_A^2 + m_\pi^2\Bigg(3g_A^2 + 1 - \frac{8}{3}c_A^2\Bigg) + Q^2x(1-x)\Bigg(5g_A^2 + 1 - \frac{40}{9}c_A^2\Bigg)\Bigg]\log\Bigg(\frac{\tilde{m}^2}{m_\pi^2}\Bigg) + \int_0^1 dx\Bigg[-\frac{32}{9}c_A^2 Q^2 x(1-x) \times \frac{\Delta \log R(\tilde{m})}{\sqrt{\Delta^2 - \tilde{m}^2}}\Bigg] - \int_0^1 dx\frac{32}{3}c_A^2\Delta[\sqrt{\Delta^2 - m_\pi^2}\log R(m_\pi) - \sqrt{\Delta^2 - \tilde{m}^2}\log R(\tilde{m})]\Bigg), \tag{43}$$

where we use the function $R(z)$ defined in Eq. (30) and introduce

$$\tilde{m}^2 = m_\pi^2 + Q^2 x(1-x). \tag{44}$$

Note that the expansion in Eq. (43) is finite at $Q^2 = 0$, i.e. $F_1^v(Q^2 = 0, m_\pi) = 1$ for any value of m_π including zero, but its derivative w.r.t. Q^2 at the origin will diverge logarithmically as $m_\pi \to 0$; cf. Equation (39). Again, the fit

parameters are $B^r_{10}(1\ \mathrm{GeV})$ and c_A. The other parameters are fixed at their chiral values; see Table VIII.

As we will also point out in Sec. IV B 3, our comparatively large lattice volume puts us at a disadvantage when studying the ratio $F_2(Q^2)/F_1(Q^2)$ for large values of $Q^2 > 1\ \mathrm{GeV}^2$. However, when using chiral expansions, this choice turns out to work to our advantage since we have sufficiently many data points at lower values of Q^2 to meaningfully apply the chiral expansion directly to the Q^2 dependence. In the chiral fits we will certainly need to apply cuts in Q^2. Hence, every fit will have fewer data points contributing to it than in the dipole case. Thus, in the end the uncertainty may very well turn out to be larger. However, this is offset by the advantage that we do not make any phenomenological assumptions on the Q^2 dependence and the results can truly be considered "first principle" results.

As the first step, we fix the interval in Q^2 to be $Q^2 \in [0, 0.5]\ \mathrm{GeV}^2$. This choice is a reasonable guess based on the discussion in Ref. [66]. With this interval, we vary the cut representing the upper value of the pion mass, m_π. The resulting values for χ^2/dof, the fit parameters and the extrapolated Dirac radii, $\langle r_1^2\rangle$ at the physical pion mass, are listed in Table XI. From this table we conclude that it is necessary to apply a rather conservative cut and restrict ourselves to $m_\pi < 400$ MeV. The value of χ^2/dof becomes extremely large beyond this point which implies that the function fails to properly describe the m_π dependence of the data. This fact is not surprising and has been reported also in [66,80,81]. We have also observed it above when applying the SSE and BChPT formulas to the radii obtained from dipole fits. In all those cases it became evident that the pion-mass dependence of the lattice data is weaker than NLO SSE demands. Although the values of the fit parameters in Table XI stabilize when ensembles at $m_\pi > 400$ MeV are included, the resulting parameters are incompatible with those obtained in the region $m_\pi < 400$ MeV. Next, we need to ascertain that the cut in Q^2 can be justified. We vary the upper end of the fit interval in Q^2 by keeping the cut for $m_\pi < 400$ MeV in place. The results are shown in Table XII. It turns out that the fit quality only mildly depends on the cut we apply in Q^2. This situation is quite different from the pion-mass dependence we encountered previously. The SSE expression Eq. (43) provides an excellent fit to the Q^2 dependence for essentially the entire range of data points, but fails to describe the pion-mass dependence for all except the smallest masses.

We now discuss the resulting curves for the chiral expansion with the cuts $Q^2 < 0.5\ \mathrm{GeV}^2$ and $m_\pi < 400$ MeV. Figure 11 shows the data for the ensemble at $m_\pi = 293$ MeV and the curve based on the best fit parameters listed in Table XII applied to the same pion mass. Regarding the Q^2 dependence in Fig. 11 we observe the surprising feature that the resulting curve appears to fit the data very well over a very large range of Q^2 values. However, we do not believe this to be of physical significance since there is no reason to believe in the validity of the chiral expansion at Q^2 values as large as $1\ \mathrm{GeV}^2$. Hence, we consider this feature to be merely accidental and the upper cut in Q^2 necessary on theoretical grounds.

Figure 12 shows the resulting chiral extrapolation of the Dirac radii as a function of the pion mass, m_π. For illustration purposes, we have included the radii obtained from the dipole fits (cf. Table VII) in the plot. These data points have no influence on the curve presented and just serve as a comparison of the two fitting methods. The red star in the plot shows the experimental value taken from Ref. [58]. When studying the resulting Dirac radii in Fig. 12 we find

TABLE XI. Fits to isovector $F_1^v(Q^2, m_\pi)$ at fixed interval of $Q^2 = [0, 0.5]\ \mathrm{GeV}^2$ with different pion-mass cuts. The experimental form factors are not included in the fit.

m_π max (MeV)	χ^2/dof	$B^r_{10}(1\ \mathrm{GeV})$	c_A	$\langle r_1^2\rangle(m_\pi^{\mathrm{phys}})$ (fm^2)
300	0.59	0.60(39)	1.15(33)	0.623(68)
400	1.86	0.35(11)	1.009(97)	0.686(21)
500	12.74	1.195(46)	1.623(23)	0.5355(98)
600	30.74	1.181(29)	1.631(13)	0.5446(65)

TABLE XII. Fits to isovector $F_1^v(Q^2, m_\pi)$ at varying intervals of Q^2 with fixed pion-mass cut, $m_\pi < 400$ MeV.

Q^2 max (GeV^2)	χ^2/dof	$B^r_{10}(1\ \mathrm{GeV})$	c_A	$\langle r_1^2\rangle(m_\pi^{\mathrm{phys}})$ (fm^2)
0.7	1.84	0.483(71)	1.127(54)	0.661(14)
0.5	1.86	0.35(11)	1.009(97)	0.686(21)
0.3	1.82	0.60(21)	1.241(158)	0.645(37)

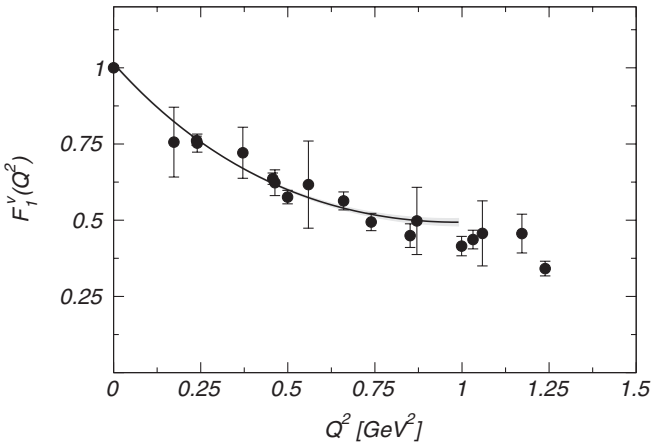

FIG. 11. SSE best fit to isovector form factor $F_1^v(Q^2, m_\pi = 293$ MeV) with lattice data for that ensemble.

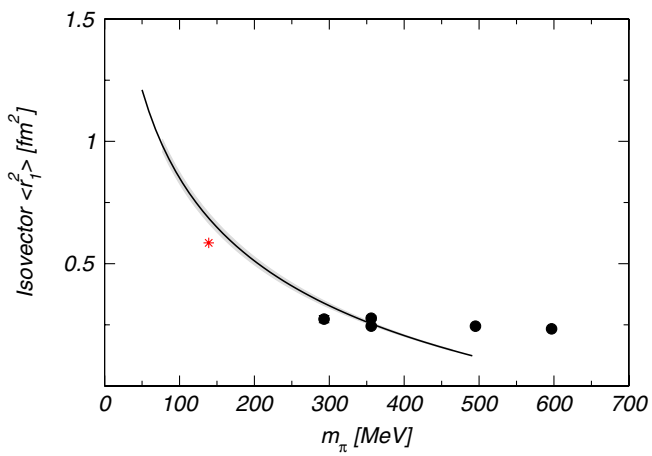

FIG. 12 (color online). Isovector Dirac radii $\langle r_1^2\rangle$ with best fit using kinematic cuts $Q^2 < 0.5$ GeV^2 and $m_\pi < 400$ MeV. The data points shown are dipole radii and experiment, which serve to compare this method with the previous one. They have not been included in the fit.

that the fit slightly overshoots the experiment and that the lattice data may very well account for the physical value of $\langle r_1^2\rangle$. Finally, we point out that the fitted parameters c_A and $B_{10}^r(1\text{ GeV})$ from the simultaneous strategy are different from those obtained with the previous strategy; cf. Table IX.

From the resulting χ^2/dof we do not see that the SSE at NLO fails to describe the functional form of $F_1^v(Q^2, m_\pi)$ if we consider the parameter region $Q^2 < 0.5$ GeV^2 and $m_\pi < 400$ MeV. The simultaneous fit yields larger uncertainties than an SSE or BChPT fit to Dirac radii from dipole fits and prefers a smaller value of c_A. In general a combined fit has the advantage that no phenomenological assumption on the functional behavior w.r.t. Q^2 is needed. Therefore this approach should become the method of choice as sufficiently small m_π and Q^2 are reached.

TABLE XIII. Comparison of dipole and tripole fit for isovector $F_2^v(Q^2)$ on the 28^3 lattice at $m_\pi = 356$ MeV.

	Dipole	Tripole
χ^2/dof	1.04	1.15
A_0	3.107(71)	3.044(68)
$M_{d/t}$ (GeV)	1.067(17)	1.374(20)
$\langle r_2^2\rangle$ (fm^2)	0.411(13)	0.371(11)

2. *Isovector Pauli form factor* $F_2^v(Q^2)$

Since according to the definition Eq. (8), $F_2^v(Q^2)$ involves a spin flip, this form factor may be better described with an additional suppression of Q^2. On the other hand, as we will discuss in the section on asymptotic scaling, Sec. IV B 3, the ratio of form factors does not follow the quark-counting rules one would expect from the leading perturbative expansion. Hence, one could use either the dipole expression already employed for the form factor $F_1^v(Q^2)$, Eq. (37), or a tripole expression via

$$F_2^v(Q^2) = A_0/(1 + Q^2/M_t^2)^3, \tag{45}$$

with the tripole mass, M_t. The tripole mass is related to the Pauli radius via

$$\langle r_2^2\rangle = \frac{18}{M_t^2}. \tag{46}$$

In the following we will first fit $F_2^v(Q^2)$ using the dipole form at fixed pion mass and study the stability of this fit as a function of cutoffs. Next, we also apply the tripole form to $F_2^v(Q^2)$ and study whether the data favors one of the two forms.

Again, we first consider the lattice results at the large volume, 28^3, at pion mass $m_\pi = 356$ MeV. At this point as well as in the remainder of this section we determine the uncertainty by applying the jackknife method to the minimization of χ^2 including the error-correlation matrix; cf. Sec. III C. When comparing dipole and tripole fits for

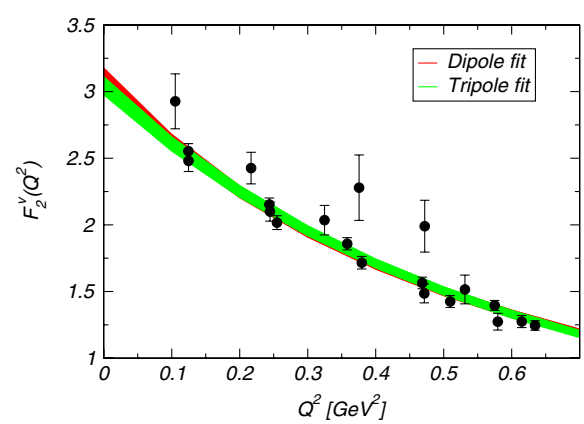

FIG. 13 (color online). Comparison of dipole and tripole fits for isovector $F_2^v(Q^2)$ on the 28^3 lattice at $m_\pi = 356$ MeV.

TABLE XIV. Dipole fits to $F_2^v(Q^2)$ with varying fit intervals.

$[Q^2_{\min}, Q^2_{\max}]$ [GeV]^2	χ^2/dof	A_0	M_d (GeV)	$\langle r_2^2 \rangle$ (fm^2)
[0, 1.5]	1.04	3.107(71)	1.067(17)	0.411(13)
[0, 0.5]	1.15	3.111(74)	1.067(20)	0.411(16)
[0, 0.4]	1.19	3.066(78)	1.095(30)	0.389(21)
[0, 0.3]	1.54	3.065(82)	1.086(34)	0.396(25)
[0, 1.5]	1.04	3.107(71)	1.067(17)	0.411(13)
[0.2, 1.5]	1.16	3.113(75)	1.064(18)	0.413(14)
[0.3, 1.5]	1.54	3.145(126)	1.052(33)	0.422(27)
[0.4, 1.5]	1.57	2.824(239)	1.139(76)	0.360(48)
[0.5, 1.5]	2.05	2.843(312)	1.130(96)	0.366(63)
[0.3, 0.5]	1.83	3.866(444)	0.893(75)	0.586(98)
[0.2, 0.4]	1.59	3.054(92)	1.098(37)	0.387(26)
[0.1, 0.3]	1.54	3.065(82)	1.086(34)	0.396(25)

the entire range of available data, we find the results listed in Table XIII. The fits are applied to the entire range of available Q^2 values. They are shown graphically in Fig. 13.

Both results agree within error bars for A_0. The resulting χ^2/dof is almost identical, but the resulting Pauli radii disagree by two sigma. Based on the quality of the fits it is not possible to favor either choice since it appears that the distinction only becomes important outside of the range of the available data.

In order to study whether both fit strategies remain stable over the entire range of data, we perform the same variation of the fitting interval as previously for $F_1^v(Q^2)$. The results for the dipole fit are shown in Table XIV and the corresponding tripole fit results in Table XV.

When varying the upper cutoff it is apparent that the variation is minimal and the resulting parameters only weakly depend on the cutoff. The uncertainty increases as expected, but the effect is small. On the other hand, when varying the lower cutoff the error bar increases notably. However, the central values remain stable and the data are still well described by the dipole fit over the entire range. When shifting the fit interval, the inclusion of

TABLE XV. Tripole fits to $F_2^v(Q^2)$ with varying fit intervals.

$[Q^2_{\min}, Q^2_{\max}]$ [GeV]^2	χ^2/dof	A_0	M_t (GeV)	$\langle r_2^2 \rangle$ (fm^2)
[0, 1.5]	1.15	3.044(68)	1.374(20)	0.371(11)
[0, 0.5]	1.15	3.072(72)	1.358(24)	0.380(14)
[0, 0.4]	1.25	3.034(76)	1.386(36)	0.365(19)
[0, 0.3]	1.53	3.046(80)	1.364(40)	0.377(22)
[0, 1.5]	1.15	3.044(68)	1.374(20)	0.371(11)
[0.2, 1.5]	1.24	3.029(71)	1.377(21)	0.370(11)
[0.3, 1.5]	1.60	2.998(108)	1.384(38)	0.366(20)
[0.4, 1.5]	1.57	2.709(204)	1.490(88)	0.316(37)
[0.5, 1.5]	2.04	2.714(261)	1.483(11)	0.319(47)
[0.3, 0.5]	1.84	3.643(361)	1.183(85)	0.501(72)
[0.2, 0.4]	1.59	3.004(86)	1.400(43)	0.357(22)
[0.1, 0.3]	1.53	3.046(80)	1.364(40)	0.377(22)

TABLE XVI. Tripole fits to isovector $F_2^v(Q^2)$ for all data sets.

m_π (MeV)	χ^2/dof	A_0	M_t (GeV)	$\langle r_2 \rangle$ (fm)
293	1.31	2.896(162)	1.389(53)	0.363(28)
356 on 28^3	1.15	3.044(68)	1.374(20)	0.371(11)
356 on 20^3	2.09	2.958(76)	1.436(25)	0.340(12)
495	1.39	3.210(44)	1.482(14)	0.319(6)
597	1.93	3.402(27)	1.529(94)	0.300(4)

TABLE XVII. SSE fit to the isovector anomalous magnetic moment, $\kappa_v^{\rm norm}$, obtained from tripole fits.

m_π max (MeV)	χ^2/dof	κ_v^0	c_V (GeV^{-1})	E_1^r(1 GeV) (GeV^{-3})
600	1.18	4.68(24)	−2.84(37)	−6.08(41)

data points at smaller values of Q^2 improves the quality of the fit and reduces the error bars notably. In the case of the tripole fit, the value of A_0 is systematically lower, but still within error bars. We conclude that $F_2^v(Q^2)$ is well described by either functional form over the entire kinematic range, but the strongest influence on fixing the parameters of the fit comes from the region of smaller Q^2 values, in particular, from $Q^2 < 0.3$ GeV^2. Compared to the fits to $F_1^v(Q^2)$ we thus find a qualitatively similar picture, although the sensitivity of the parameters to the inclusion of the data at small values of Q^2 is larger.

Finally, we perform a series of tripole fits to our entire data set at all pion masses. Results are summarized in Table XVI. We again observe finite-size effects for the Pauli radius $\langle r_2\rangle$. On top of this, the Pauli radius increases as the pion mass decreases on the lattices with fixed physical volume. Hence, we have reason to expect that finite-size effects may be non-negligible for the smallest value of m_π.

SSE chiral fits to isovector $\langle r_2^2\rangle$ and κ^v.—

Similar to what we did for the isovector Dirac form factor, we now fit the mean squared Pauli radius $\langle r_2^2\rangle$ and the isovector anomalous magnetic moment, κ_v, using chiral formulas from the SSE expansion at NLO. In this case, the expressions as functions of m_π are [67,82]

$$\langle r_2^2\rangle = \frac{g_A^2 m_N}{8f_\pi^2\kappa_v(m_\pi)\pi m_\pi} + \frac{c_A^2 m_N}{9f_\pi^2\kappa_v(m_\pi)\pi^2\sqrt{\Delta^2 - m_\pi^2}}\log\left(\frac{\Delta}{m_\pi} + \sqrt{\frac{\Delta^2}{m_\pi^2} - 1}\right) + \frac{24m_N}{\kappa_v(m_\pi)}B_{c2},$$

$$\kappa_v(m_\pi) = \kappa_v^0 - \frac{g_A^2 m_\pi m_N}{4\pi f_\pi^2} + \frac{2c_A^2\Delta m_N}{9\pi^2 f_\pi^2}\left(\sqrt{1 - \frac{m_\pi^2}{\Delta}}\log R(m_\pi) + \log\left(\frac{m_\pi}{2\Delta}\right)\right) - 8E_1^r(\lambda)m_N m_\pi^2 + \frac{4c_A c_V g_A m_N m_\pi^2}{9\pi^2 f_\pi^2}\log\left(\frac{2\Delta}{\lambda}\right)$$
$$+ \frac{4c_A c_V g_A m_N m_\pi^3}{27\pi f_\pi^2\Delta} - \frac{8c_A c_V g_A \Delta^2 m_N}{27\pi^2 f_\pi^2}\left(\left(1 - \frac{m_\pi^2}{\Delta^2}\right)^{3/2}\log R(m_\pi) + \left(1 - \frac{3m_\pi^2}{2\Delta^2}\right)\log\left(\frac{m_\pi}{2\Delta}\right)\right), \quad (47)$$

where $R(m)$ was defined in Eq. (30). The pion-mass dependence of the product $\kappa_v(m_\pi)\langle r_2^2\rangle$ contains a single unknown parameter, B_{c2}, whose effect is similar to the counterterm $B_{10}^r(\lambda)$ in $\langle r_1^2\rangle$. In addition to the expression above, we need to correct for the fact that Eq. (47) assumes the nucleon mass to be constant when computing the m_π dependence of κ_v. This assumption is certainly not justified, so we need to correct the expression by working with the normalized anomalous magnetic moment, $\kappa_v^{\rm norm}$, as defined in Eq. (35). The SSE pion-mass dependence for κ_v involves three additional low-energy constants, κ_v^0, c_V, and $E_1^r(\lambda)$. Since $\kappa_v(m_\pi)$ is also part of the expression for $\langle r_2^2\rangle$ and is always obtained from the same tripole fit to $F_2^v(Q^2)$, it makes sense to fit κ_v separately at first and then perform a single-parameter fit to $\kappa_v\langle r_2^2\rangle$. In this way, the best fit stability is guaranteed.

TABLE XVIII. SSE fit to the isovector Pauli radius, $\langle r_2^2\rangle$, obtained from tripole fits.

m_π max (MeV)	χ^2/dof	B_{c2} (GeV^{-3})
600	22.2	−6.1(12) 10^{-2}

We employ the same parameters for the expression as listed previously in Table VIII. In this case we fix c_A to the value of 1.5. Furthermore, since κ_v has three fit parameters, we can only work with a pion-mass cut of $m_\pi < 600$ MeV. The result is shown in Table XVII. The subsequent fit to $\kappa_v\langle r_2^2\rangle$ with κ_v being canceled out in the next step is shown in Table XVIII. Unfortunately, the resulting χ^2/dof is not very good, evidently due to the stronger curvature of the NLO SSE form. The curves will be plotted below in Fig. 14.

BChPT fits to isovector $\langle r_2^2\rangle$ and κ^v.—

The expansions of the isovector anomalous magnetic moment, κ_v, and the isovector mean squared Pauli radius, $\langle r_2^2\rangle$, up to the order $\mathcal{O}(p^4)$ are given by

$$\langle r_2^2\rangle = \frac{M_N}{M_0}\left(\frac{1}{\kappa_v}B_{c2} + (\langle r_2^2\rangle)^{(3)} + (\langle r_2^3\rangle)^{(4)}\right) + \mathcal{O}(p^6),$$
$$\kappa_v = \frac{M_N}{M_0}(c_6 - 16M_0 m_\pi^2 e_{106}^r(\lambda) + \delta\kappa_v^{(3)} + \delta\kappa_v^{(4)}) + \mathcal{O}(p^6), \quad (48)$$

with the individual contributions at each order:

$$
\begin{aligned}
B_{c2} &= 24M_0 e_{74}^r(\lambda),\\
(\langle r_2^2\rangle)^{(3)} &= \frac{1}{\kappa_v}\frac{g_A^2 M_0}{16\pi^2 f_\pi^2 M_N^5(m_\pi^2-4M_N^2)}\Big[-124M_N^6+105m_\pi^2M_N^4-18m_\pi^4M_N^2+6(3m_\pi^6-22M_N^2m_\pi^4+44M_N^4m_\pi^2\\
&\quad -16M_N^6)\log\frac{m_\pi}{M_N}\Big]+\frac{1}{\kappa_v}\frac{g_A^2M_0}{8\pi^2f_\pi^2M_N^5m_\pi(4M_N^2-m_\pi^2)^{3/2}}[9m_\pi^8-84M_N^2m_\pi^6+246M_N^4m_\pi^4-216M_N^6m_\pi^2\\
&\quad +16M_N^8]\arccos\frac{m_\pi}{2M_N},\\
(\langle r_2^2\rangle)^{(4)} &= -\frac{1}{\kappa_v}\frac{c_6g_A^2m_\pi^3}{16\pi^2f_\pi^2M_0^4(4M_0^2-m_\pi^2)^{3/2}}(4m_\pi^4-27m_\pi^2M_0^2+42M_0^4)\arccos\frac{m_\pi}{2M_0}+\frac{1}{\kappa_v}\frac{1}{16\pi^2f_\pi^2M_0^4(m_\pi^2-4M_0^2)}\\
&\quad\times\Big[16c_4M_0^7+52g_A^2M_0^6-4c_4m_\pi^2M_0^5-14c_6g_A^2m_\pi^2M_0^4-13g_A^2m_\pi^2M_0^4+8(3g_A^2-c_4M_0)(m_\pi^2-4M_0^2)M_0^4\log\frac{m_\pi}{M_0}\\
&\quad +4c_6g_A^2m_\pi^4M_0^2-g_A^2(m_\pi^2-4M_0^2)(4c_6m_\pi^4-3c_6m_\pi^2M_0^2+24M_0^4)\log\frac{m_\pi}{M_0}\Big],\\
\delta\kappa_v^{(3)} &= \frac{g_A^2m_\pi^2M_0}{8\pi^2f_\pi^2M_N^3}\Big[(3m_\pi^2-7M_N^2)\log\frac{m_\pi}{M_N}-3M_N^2\Big]-\frac{g_A^2m_\pi M_0}{8\pi^2f_\pi^2M_N^3\sqrt{(4M_N^2-m_\pi^2)}}[3m_\pi^4-13M_N^2m_\pi^2+8M_N^4]\arccos\frac{m_\pi}{2M_N},\\
\delta\kappa_v^{(4)} &= -\frac{m_\pi^2}{32\pi^2f_\pi^2M_0^2}\Big[4g_A^2(c_6+1)M_0^2-g_A^2(5c_6m_\pi^2+28M_0^2)\log\frac{m_\pi}{M_0}+4M_0^2(2c_6g_A^2+7g_A^2+c_6-4c_4M_0)\log\frac{m_\pi}{\lambda}\Big]\\
&\quad -\frac{g_A^2c_6m_\pi^3}{32\pi^2f_\pi^2M_0^2\sqrt{4M_0^2-m_\pi^2}}(5m_\pi^2-16M_0^2)\arccos\frac{m_\pi}{2M_0}.
\end{aligned}
\tag{49}
$$

In the Pauli radius, c_6 only shows up in the $\mathcal{O}(p^4)$ part which is of higher order. Thus, we cannot use the mean squared radius $\langle r_2^2\rangle$ for a determination of c_6 in isolation. We therefore settle for a simultaneous fit to all three quantities $\langle r_1^2\rangle$, $\langle r_2^2\rangle$, and κ_v. To do this, we insert the expansion from Eq. (42) for the nucleon mass M_N in Eqs. (40), (41), (48), and (49). The parameter c_4 is again taken from Table X. We take correlations into account by using both the error-correlation matrix and the superjackknife prescriptions as outlined in Sec. III C. For these fits we also set the scale to $\lambda = M_0$. The resulting fits are stable; however, the χ^2/dof is relatively large. The reason is that the BChPT curves for both $\langle r_1^2\rangle$ and $\langle r_2^2\rangle$ show a stronger curvature than our lattice data. If we included data at higher pion masses, χ^2/dof would increase even more. The results are summarized in Table XIX. Both the (poor) quality of the fit as well as the parameters agree with Ref. [9]. We finally display the fits with $m_\pi < 600$ MeV (SSE) and $m_\pi < 400$ MeV (BChPT) for the normalized isovector anomalous magnetic moment, $\kappa_v^{\rm norm}$, on the left panel of Fig. 14 and the results from the fits with $m_\pi < 600$ MeV (SSE) and $m_\pi < 400$ MeV (BChPT) for the Pauli radius, $\langle r_2^2\rangle$, in the right panel of said figure.

We find that the fit quality for $\kappa_v^{\rm norm}$ is good and the fits to $\langle r_2^2\rangle$ are similar to those for $\langle r_1^2\rangle$—the lattice data does not yet display the feature of strong divergence in the chiral limit and tends to be flatter as a function of the pion mass than the associated curves from chiral perturbation theory. Again, it is possible that the fits work already well below $m_\pi = 400$ MeV for calculations carried out in sufficiently large spatial volumes.

Simultaneous fits to $F_2^v(Q^2, m_\pi)$.—

For the chiral expansion in $F_2^v(Q^2, m_\pi)$ we use the simultaneous expansion based on SSE in Q^2 and m_π from Refs. [67,82]:

$$
\begin{aligned}
F_2^v(Q^2, m_\pi) &= \kappa_v(m_\pi) - g_A^2\frac{4\pi m_N}{(4\pi f_\pi)^2}\int_0^1 dx(\tilde m - m_\pi)\\
&\quad +\frac{32c_A^2m_N\Delta}{9(4\pi f_\pi)^2}\int_0^1 dx\Big[\frac{1}{2}\log\Big(\frac{\tilde m^2}{4\Delta^2}\Big)\\
&\quad -\log\Big(\frac{m_\pi}{2\Delta}\Big)+\frac{\sqrt{\Delta^2-\tilde m^2}}{\Delta}\log R(\tilde m)\\
&\quad -\frac{\sqrt{\Delta^2-m_\pi^2}}{\Delta}\log R(m_\pi)\Big],
\end{aligned}
\tag{50}
$$

TABLE XIX. Simultaneous fit of the BChPT expression to the anomalous magnetic moment, κ_v, and the radii $\langle r_1^2\rangle$ and $\langle r_2^2\rangle$, as obtained from tripole fits.

χ^2/dof	c_6	$d_6^r(M_0)$ (GeV^{-2})	$e_{74}^r(M_0)$ (GeV^{-3})	$e_{106}^r(M_0)$ (GeV^{-3})
10.23	4.31(11)	0.924(12)	1.201(34)	−0.08(11)

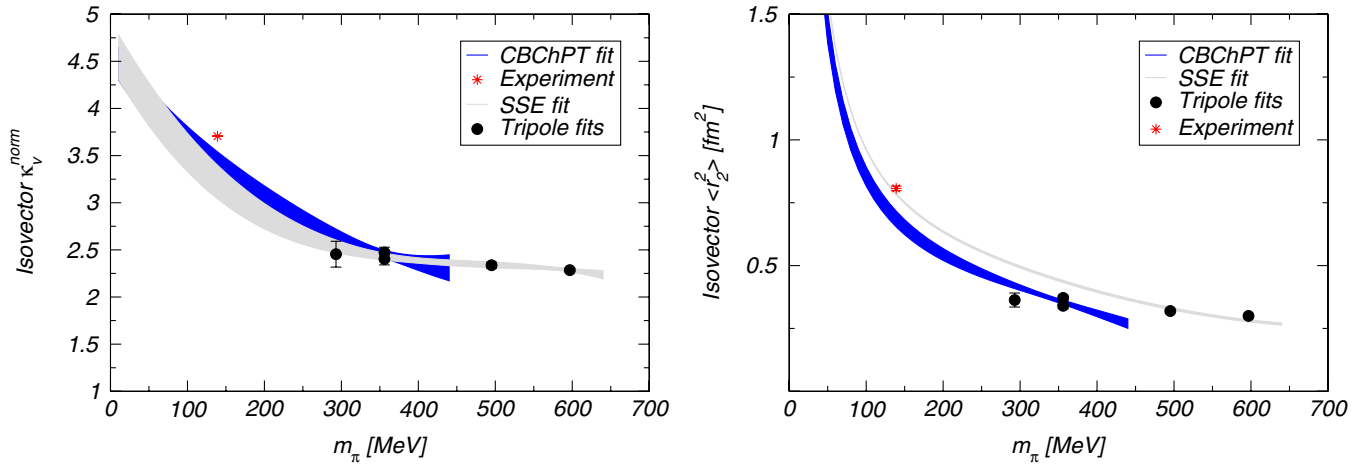

FIG. 14 (color online). Results of SSE and BChPT fits to the normalized anomalous magnetic moment $\kappa_v^{\rm norm}$ (left panel) and to the isovector mean squared radius $\langle r_2^2 \rangle$ (right panel).

with $R(x)$ and $\tilde{m}$ as defined previously in Eqs. (30) and (44). Note that this expansion also includes the function for $\kappa_v(m_\pi)$ defined previously in Eq. (47). The input parameters are the same as used previously, Table VIII. The parameters are c_V, $E_1^r(\lambda = 1\ \text{GeV})$, and κ_v^0 in addition to c_A. The number of parameters is larger than for $F_1^v(Q^2)$, but we decided nevertheless not to add the experimental data point in this fit.

Similar to our study for the form factor $F_1^v(Q^2, m_\pi)$ in Sec. IV B 1, we also vary the cuts in Q^2 and m_π to find an acceptable fit range for $F_2^v(Q^2, m_\pi)$. We start out by keeping the cut $Q^2 < 0.4\ \text{GeV}^2$ in place and varying the cut in the pion mass. Table XX summarizes our findings. Note that we cannot use $m_\pi < 400$ MeV since we would have insufficient data points to constrain all three parameters in κ_v; cf. Equation (47). As seen from the resulting values of χ^2/dof the quality of the fits is good for the entire range of pion masses. This feature is distinct from the corresponding case of $F_1^v(Q^2, m_\pi)$. Next, we vary the upper cut in Q^2 and keep $m_\pi < 500$ MeV. The results are collected in Table XXI. When increasing the number of data points, the χ^2/dof increases and we conclude that the selection $Q^2 < 0.4\ \text{GeV}^2$ is preferred. Apparently, the Q^2 dependence is not described well beyond that point. We also remind the reader that we find finite-volume effects to be reduced when only considering $Q^2 < 0.4\ \text{GeV}^2$ in Sec. III E. Hence, we finally settle for the cuts $Q^2 = [0, 0.4]\ \text{GeV}^2$ and $m_\pi < 500$ MeV for our final plots. This choice is compatible with our choice for $F_1^v(Q^2, m_\pi)$, and it both gives acceptable fits and minimizes the unknown higher-order contributions in the SSE. We notice, however, that the parameter c_A is systematically lower than in the previous SSE fits and not compatible with its estimate from the $\Delta \to N\pi$ decay width [9]. Graphically, the resulting curve is shown for a single ensemble at $m_\pi = 293$ MeV in Fig. 15. The graph makes

TABLE XX. Fits to isovector $F_2^v(Q^2, m_\pi)$ at fixed interval of $Q^2 = [0, 0.4]\ \text{GeV}^2$ with different pion-mass cuts.

m_π max (MeV)	χ^2/dof	c_V (GeV^{-1})	E_1^r(1 GeV) (GeV^{-3})	κ_v^0	c_A
500	1.82	−4.1(20)	−4.7(11)	4.47(50)	0.852(98)
600	1.61	−3.54(46)	−4.40(31)	4.62(14)	0.851(97)

TABLE XXI. Fits to isovector $F_2^v(Q^2, m_\pi)$ with varying cuts in Q^2 at fixed pion-mass cut, $m_\pi < 500$ MeV.

Q^2 max (GeV^2)	χ^2/dof	c_V (GeV^{-1})	E_1^r(1 GeV) (GeV^{-3})	κ_v^0	c_A
0.3	1.54	−6.6(68)	−3.8(11)	4.67(51)	0.40(32)
0.4	1.82	−4.1(20)	−4.7(11)	4.47(50)	0.852(98)
0.5	2.03	−4.0(14)	−4.57(78)	4.63(36)	0.851(42)
0.6	2.77	−4.4(13)	−5.11(77)	4.44(36)	0.941(35)
0.7	4.87	−4.0(11)	−5.40(74)	4.40(35)	1.100(25)

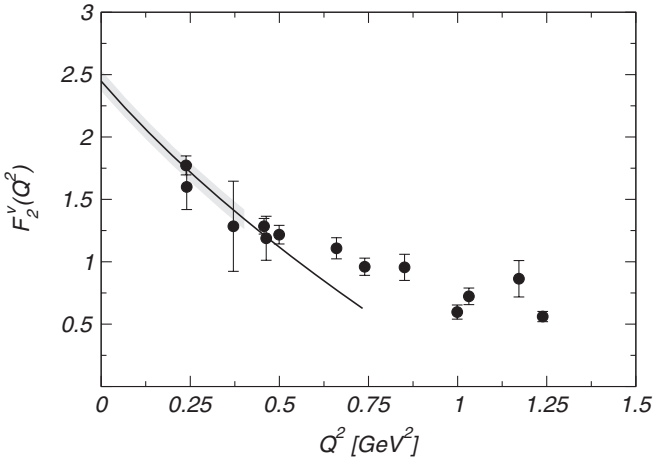

FIG. 15. Isovector form factor $F_2^v(Q^2, m_\pi)$ lattice data with best fit SSE at $m_\pi = 293$ MeV.

it apparent that $F_2^v(Q^2, m_\pi)$ should be cut below $Q^2 < 0.4$ GeV^2.

We finally plot curves of $\langle r_2^2 \rangle$ and $\kappa_v^{\rm norm}$ derived from the above fit as functions of m_π in Fig. 16. The tripole fit data points and the experimental result are included in the graph to provide a comparison to the former method. They have not been used in the fit. The qualitative picture is similar to that from the SSE and BChPT fits to the tripole radii and magnetic moments. The curves slightly underestimate the results at the physical pion mass. The advantage of this scheme is the same as in the simultaneous fits to $F_1^v(Q^2, m_\pi)$, namely, the absence of phenomenological assumptions on the functional behavior w.r.t. Q^2.

3. Asymptotic scaling

Although form factors have been studied experimentally for several decades and using perturbative QCD many qualitative and quantitative features have been understood very well, for the proton $F_2^p(Q^2)$ a notable discrepancy has been found in recent spin-transfer measurements [60–64]. From quark-counting rules one expects the ratio $F_2^p(Q^2)/F_1^p(Q^2)$ to scale proportionally to Q^{-2} which is consistent with experimental measurements using the Rosenbluth method. The recent spin-transfer experiments, on the other hand, found a scaling of $F_2^p(Q^2)/F_1^p(Q^2)$ proportional to Q^{-1}, instead. The source of the discrepancy is now generally believed to be two-photon exchange processes; see Ref. [55]. On the lattice we are in a unique position to study form factors using exactly single-photon exchanges without contamination from other processes. This analysis can proceed in a fully model-independent way.

The downside of the lattice technology is the limitation to rather small virtualities, Q^2, since the external momenta, $\vec{p}'$ and $\vec{p}$ in Eq. (2), cannot be chosen too large. For larger values of the external momenta the exponential in Eqs. (12) and (13) introduces large fluctuations which quickly deteriorate the signal-to-noise ratio. A quantitative analysis of this phenomenon has been given in Ref. [83]. Also, controlling the cutoff effects requires $|\vec{q}| \ll \pi/a$.

Figure 17 shows our results for the ratio $QF_2^v(Q^2)/F_1^v(Q^2)$ for all available ensembles. The quantities displayed show signs of saturation beyond $Q^2 = 1$ GeV^2 for the largest pion masses. For the smaller pion masses saturation is not achieved conclusively, but we observe evidence of a pion-mass dependence of the ratio. Unfortunately, we do not have data at sufficiently high momentum transfer on the 28^3 lattice at $m_\pi = 356$ MeV to reach the scaling region of interest.

To conclude, we find that the picture obtained from spin-transfer experiments is qualitatively reproduced in our lattice data. The residual pion-mass dependence prohibits

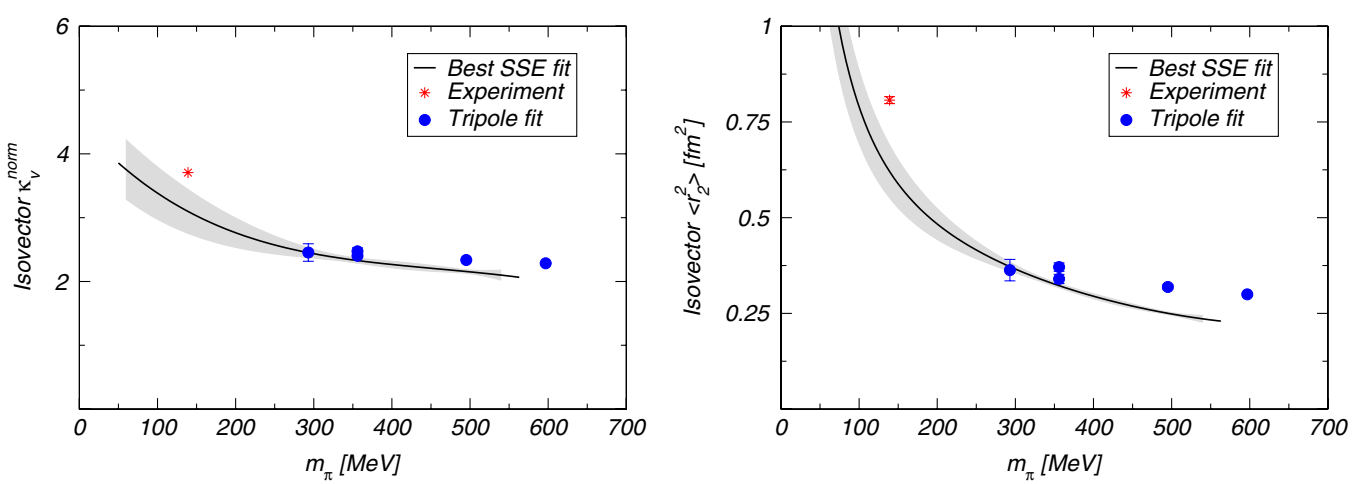

FIG. 16 (color online). Isovector normalized anomalous magnetic moment $\kappa_v^{\rm norm}$ (left panel) and mean squared radius $\langle r_2^2 \rangle$ (right panel) as a function of the pion mass as obtained from an SSE fit to the chiral expansion of $F_2^v(Q^2, m_\pi)$. The data points shown are tripole radii and experiment, which serve to compare this method to the previous one and to phenomenology. They have not been included in the fit.

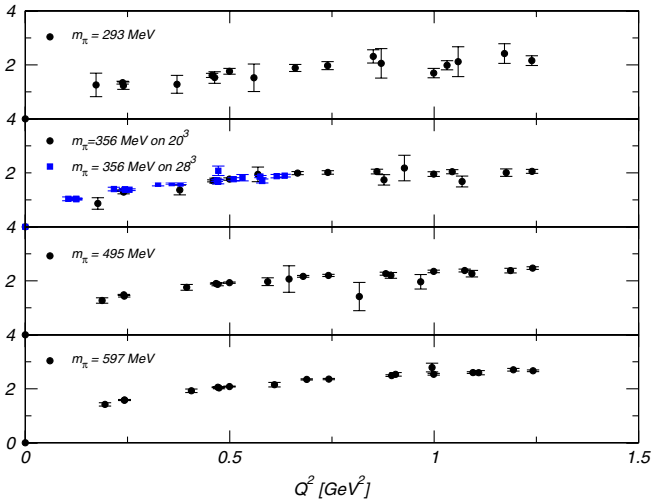

FIG. 17 (color online). Data for the ratio of $QF_2^v(Q^2)/F_1^v(Q^2)$.

a more precise quantitative analysis. New techniques are probably needed to establish the relative scaling of the form factors with confidence.

4. Isovector Sachs form factors

In the previous Secs. IV B 1 and IV B 2 we have discussed the Dirac and Pauli form factors, $F_1^v(Q^2)$ and $F_2^v(Q^2)$, and found them to obey dipole forms very well over their entire parameter range. The Sachs form factors, $G_E(Q^2)$ and $G_M(Q^2)$, are linear combinations thereof and phenomenologically are usually fit using also dipole forms. It is therefore important to see whether the lattice data prefer the one or the other dipole fit scheme since the sum of dipoles can only be approximately another dipole form.

To facilitate this study, we have subjected both $G_E(Q^2)$ and $G_M(Q^2)$ to the same tests as previously applied to $F_1^v(Q^2)$ and $F_2^v(Q^2)$. The results are summarized in Tables XXII and XXIII. They show fit results obtained by applying various cuts in Q^2 to dipole fits to $G_E(Q^2)$ and $G_M(Q^2)$, respectively. All tables correspond to the case $m_\pi = 356$ MeV on the 28^3 lattice.

We also compared the dipole vs the tripole form for $G_M(Q^2)$. The results from the fits are shown in Table XXIV. Figure 18 compares the results graphically. Similar to the case of the Pauli form factor we do not find a favorite fitting function.

Finally, we apply the dipole fits to all available data sets and extract the radii, $\langle r_E\rangle$ and $\langle r_M\rangle$. The results are shown in Tables XXV and XXVI. It turns out that a dipole fit to $G_E(Q^2)$ has a slightly smaller χ^2/dof compared to a fit to $F_1^v(Q^2)$. On the other hand, fitting $G_M(Q^2)$ with a dipole or a tripole is no better than fitting $F_2^v(Q^2)$. In both cases the fits do not exhibit a clear preference for either a dipole or a tripole function. Similar to the fits to $F_1^v(Q^2)$ and the case of $F_2^v(Q^2)$ we observe finite-size effects when comparing the two volumes at 20^3 and 28^3. However, in the case of $G_E(Q^2)$ they appear to be less pronounced, even though the χ^2/dof is slightly smaller.

5 Flavor dependence

We investigated the flavor dependence of the connected part of the $F_1(Q^2)$ form factor by studying the ratio of $F_1^d(Q^2)/F_1^u(Q^2)$. Experimentally, this ratio is being scrutinized currently; see Ref. [84] for the Web site of the experiment. Since the forward value of the ratio is trivially determined by the number of quarks, the interesting quantity is the slope, $s(m_\pi)$, w.r.t. Q^2 of the ratio. Before comparing to experiment, this quantity needs to be chirally extrapolated, and we have adopted the form [85]

$$s(m_\pi) = k_1 - k_2 \log\left(\frac{m_\pi^2}{(4\pi f_\pi)^2}\right), \tag{51}$$

with two generic parameters, k_1 and k_2. Figure 19 shows the lattice calculations of the ratios at the three lightest quark masses. The resulting slopes obtained from linear fits to these data are summarized in Table XXVII.

TABLE XXII. Dipole fits to $G_E(Q^2)$ with varying fit intervals.

$[Q^2_{\min}, Q^2_{\max}]$ (GeV^2)	χ^2/dof	A_0	M_d (GeV)	$\langle r_E^2\rangle$ (fm^2)
[0, 1.5]	1.00	0.9992(20)	1.029(11)	0.4406(96)
[0, 0.5]	0.69	0.9994(22)	1.035(12)	0.4362(103)
[0, 0.4]	0.80	0.9997(22)	1.035(12)	0.4361(104)
[0, 0.3]	1.23	0.9999(22)	1.035(12)	0.4364(104)
[0, 0.2]	1.75	1.0005(23)	1.041(13)	0.4311(111)
[0, 1.5]	1.00	0.9992(20)	1.029(11)	0.4406(96)
[0.1, 1.5]	0.93	1.0048(42)	1.022(12)	0.4474(108)
[0.2, 1.5]	0.82	1.0175(108)	1.008(16)	0.4600(150)
[0.3, 1.5]	0.81	1.0500(243)	0.983(23)	0.4835(222)
[0.4, 1.5]	1.23	1.0636(625)	0.975(41)	0.4915(412)
[0.3, 0.5]	0.39	1.0295(649)	1.003(58)	0.4649(534)
[0.2, 0.4]	0.40	1.0061(151)	1.023(23)	0.4461(205)
[0.1, 0.3]	1.06	1.0064(51)	1.024(14)	0.4455(125)

TABLE XXIII. Dipole fits to $G_M(Q^2)$ with varying fit intervals.

$[Q^2_{\rm min}, Q^2_{\rm max}]$ (GeV^2)	χ^2/dof	A_0	M_d (GeV)	$\langle r_M^2\rangle$ (fm^2)
[0, 1.5]	1.07	4.068(69)	1.127(15)	0.368(10)
[0, 0.5]	1.21	4.082(73)	1.126(18)	0.369(12)
[0, 0.4]	1.33	4.041(77)	1.148(26)	0.355(16)
[0, 0.3]	1.79	4.051(81)	1.134(29)	0.363(19)
[0.2, 1.5]	1.15	4.064(73)	1.127(16)	0.368(11)
[0.3, 1.5]	1.55	4.085(121)	1.120(29)	0.372(20)
[0.4, 1.5]	1.51	3.716(234)	1.208(66)	0.320(35)
[0.3, 0.5]	1.79	4.837(415)	0.966(68)	0.501(70)
[0.2, 0.4]	1.70	4.010(915)	1.158(33)	0.348(20)
[0.1, 0.3]	1.79	4.051(807)	1.134(29)	0.363(19)

TABLE XXIV. Comparison between dipole and tripole fits for isovector $G_M(Q^2)$.

	Dipole	Tripole
χ^2/dof	1.07	1.28
A_0	4.0682(694)	3.9976(671)
$M_{d/t}$ (GeV)	1.127(15)	1.444(18)
$\langle r_M^2\rangle$ (fm^2)	0.368(10)	0.336(86)

We observe that the lattice data are quite linear for $Q^2 < 0.5$ GeV^2 and approximately linear up to 1 GeV^2. Since the leading chiral expansion Eq. (51) only tells us how to extrapolate the slope to the physical pion mass, we only fit the slope at low Q^2 values in these fits. Figure 20 shows the chiral extrapolation of the slope displayed in Fig. 19 to the physical pion mass, denoted by the vertical dashed line. The leading chiral singularity is $\log m_\pi$; cf. Sec. IV B 1, which explains the divergence of the curve as the pion mass goes to zero. The error band propagates the statistical errors to the physical mass and yields the final result for the slope. This final number is shown in the last row of Table XXVII. The fit parameters are summarized in Table XXVIII.

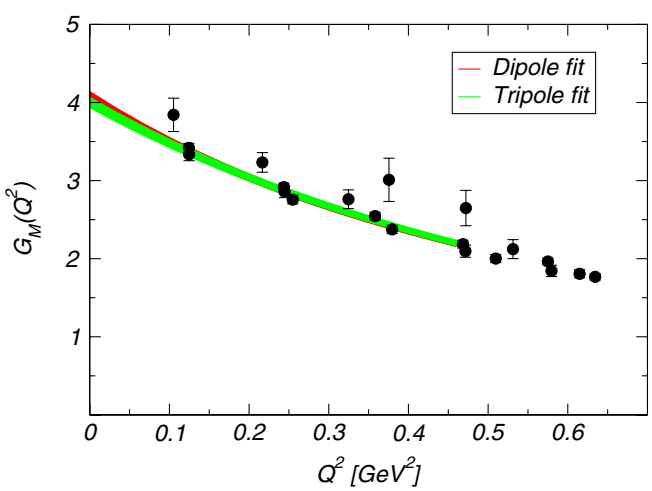

FIG. 18 (color online). Comparison between dipole and tripole fit for isovector $G_M(Q^2)$.

The prediction that can be meaningfully compared to experiment is shown in Fig. 21. The linear behavior of F_1^d/F_1^u as a function of Q^2 departing from $Q^2 = 0$, extrapolated to the physical pion mass is plotted, including the one-sigma error band.

6. Isoscalar form factors

We now turn our attention to the isoscalar form factors. We remind the reader that we have only computed the connected Wick contractions, and that the disconnected diagrams remain to be calculated in the future. In the following we discuss the isoscalar form factors, $F_1^s(Q^2)$ and $F_2^s(Q^2)$ separately.

Isoscalar form factor $F_1^s(Q^2)$.—

We first apply the well-known dipole fits again to the isoscalar form factor $F_1^s(Q^2)$. First, we study the stability of the dipole fits to variations in the fit interval like we did before. We focus again on the ensemble with $m_\pi = 356$ MeV on the 28^3 lattice. Table XXIX summarizes our

TABLE XXV. Dipole fits to $G_E(Q^2)$ for all data sets.

m_π (MeV)	χ^2/dof	A_0	M_d (GeV)	$\langle r_E^2\rangle$ (fm^2)
293	0.77	1.0008(74)	1.014(20)	0.4544(180)
356 on 28^3	1.00	0.9992(20)	1.029(11)	0.4406(96)
356 on 20^3	1.66	0.9998(15)	1.060(11)	0.4158(86)
495	1.43	0.9999(9)	1.106(7)	0.3818(46)
597	4.02	0.9999(5)	1.145(4)	0.3562(28)

TABLE XXVI. Dipole fits to $G_M(Q^2)$ for all data sets.

m_π (MeV)	χ^2/dof	A_0	M_d (GeV)	$\langle r_M^2\rangle$ (fm^2)
293	0.93	3.938 31(1842)	1.133(44)	0.364(28)
356 on 28^3	1.07	4.0682(694)	1.127(15)	0.368(10)
356 on 20^3	2.11	3.9854(826)	1.180(20)	0.336(11)
495	1.13	4.2913(471)	1.196(11)	0.3266(62)
597	1.14	4.4684(291)	1.236(8)	0.3060(38)

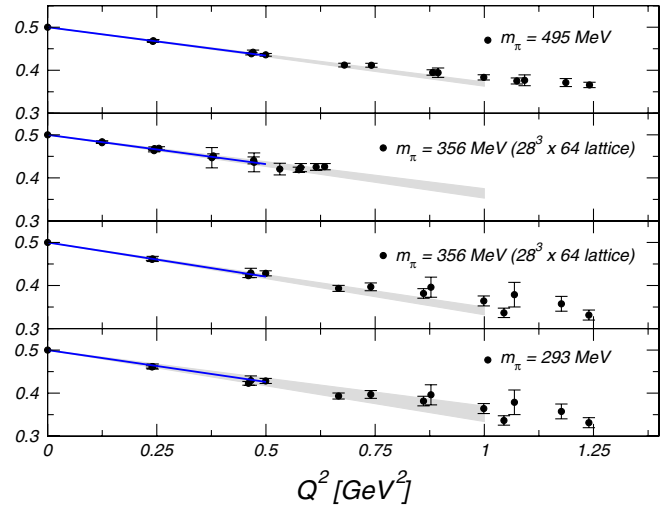

FIG. 19 (color online). Linear fits to $F_1^d/F_1^u(Q^2)$ ratio.

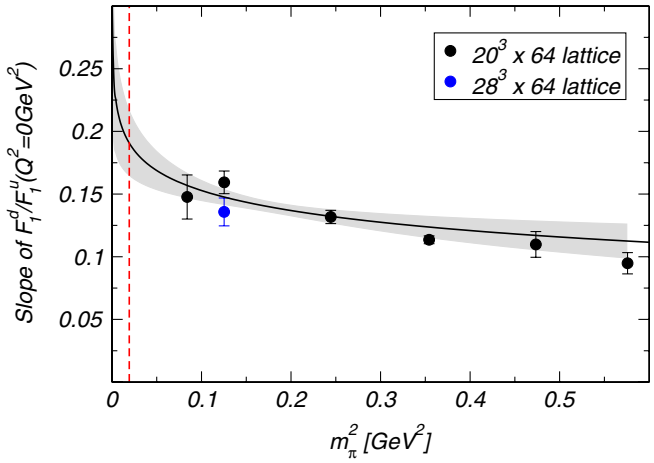

FIG. 20 (color online). Chiral fit to the slope of the ratio $F_1^d/F_1^u(Q^2 = 0\ \text{GeV}^2)$. The physical pion mass is marked by the dashed red line.

findings. It is evident that the dipole provides an excellent, stable fit over the entire available data range.

Applying dipole fits to all available pion masses yields the results shown in Table XXX. We find that even at the lightest available pion mass the obtained radii underestimate the empirical value $\langle r_1^2\rangle = (0.782\ \text{fm})^2$ quoted from Ref. [67] substantially by a factor of 2. A similar discrepancy also appeared in the isovector case, Sec. IV B 1, but it seems to be even more pronounced here. Another noteworthy fact is the inconsistency of the forward value, $F_1^s(Q^2 = 0)$, with the expected value of three. This is most likely a cutoff effect. Although the disagreement is only mild (about 1%), it is outside the relative error bars. We will comment on this below when discussing the chiral expansion.

Reference [67] discusses the chiral expansion in m_π and Q^2. The next-to-leading order SSE expression

$$F_1^s(Q^2, m_\pi) = 3 - 12\tilde{B}_1 \frac{Q^2}{(4\pi f_\pi)^2} \tag{52}$$

has only a linear Q^2 dependence and no m_π dependence. As we have pointed out before, in comparison with the isovector form factor $F_1^v(Q^2, m_\pi)$, the derivative w.r.t. m_π of the isoscalar one does not diverge in the limit $m_\pi \to 0$. It merely approaches a constant value. Since the Q^2 dependence only has a linear part, we need to again restrict ourselves to the regime of small values of Q^2.

TABLE XXVII. Slopes at $Q^2 = 0$ GeV^2 of $F_1^d/F_1^u(Q^2)$ from linear fits. The last line shows the chirally extrapolated value.

m_π (MeV)	Slope (GeV^{-2})
495	−0.132(5)
356 on 28^3	−0.136(11)
356 on 20^3	−0.159(9)
293	−0.148(18)
$m_\pi^{\text{phys}} = 139$	−0.190(26)

Table XXX suggests a nontrivial m_π dependence. However, we observe that the results for $\langle r_1^2\rangle$ are still constant within statistics when we restrict ourselves to the region $m_\pi < 400$ MeV. This cut is consistent with what we have found before in the isovector case.

With the restriction of $m_\pi < 400$ MeV we perform a chiral fit based on Eq. (52). However, when covering the entire fit interval, $Q^2 = [0, 0.5]$ GeV^2, we find an unacceptably large $\chi^2/\text{dof} = 128$. We traced the problem back to the value at the origin, $F_1^s(Q^2 = 0)$. Because of the systematic shift with a small relative error we end up with such a huge discrepancy. Hence, we restrict ourselves to the fitting interval, $Q^2 > 0.01$ GeV^2, which excludes this data point. Varying the upper cutoff in Q^2 yields the results tabulated in Table XXXI. Surprisingly, the radii are even smaller than those obtained from the dipole expression. Furthermore, the overall quality of the fits is poor until $Q^2 < 0.2$ GeV^2 is imposed, at which point the resulting radius is still about 20% smaller than the one obtained from the dipole form. We conclude that applying the NLO expression (52) does not give new insight into the problem.

Isoscalar form factor $F_2^s(Q^2)$.—

The chiral expansion from Ref. [82] yields for the isoscalar spin-flip form factor, $F_2^s(Q^2, m_\pi)$, an expansion of the form

$$F_2^s(Q^2, m_\pi) = \kappa_s^0 - 8m_N m_\pi^2 \tilde{E}_2; \tag{53}$$

TABLE XXVIII. Fit parameters to the slope of the ratio $F_1^d/F_1^u(Q^2)$ as a function of the pion mass.

χ^2/dof	1.5
k_1	0.093(23) GeV^{-2}
k_2	0.023(11) GeV^{-2}
$s(m_\pi^{\text{phys}})$	−0.190(26) GeV^{-2}

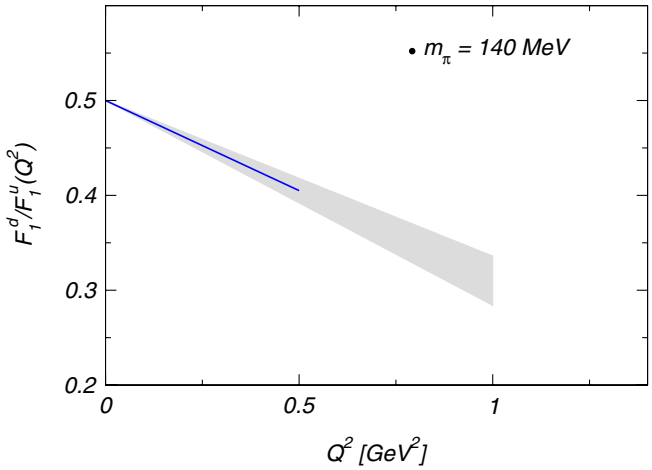

FIG. 21 (color online). Linear slope of $F_1^d/F_1^u(Q^2)$ at the physical pion mass.

i.e., the leading Q^2 dependence vanishes and the m_π dependence is quadratic. Table XXXII shows the result of a fit of Eq. (53) to our lattice data with the cuts $Q^2 = [0, 0.5]$ GeV^2 and $m_\pi < 400$ MeV. The experimental value for $F_2^s(Q^2 = 0, m_\pi = m_\pi^{\rm phys})$ taken from Ref. [69] is listed on the last line. It is evident that the data suggest $\kappa_s^0 < 0$, but we can only fix the order of magnitude since the relative error is about 50%. When plotting the data for the ensemble at $m_\pi = 293$ MeV, we find that the data are indeed flat, albeit with a large relative error. Figure 22 shows this graph with the fit function from Table XXXII for $F_2^s(Q^2, m_\pi = 293$ MeV), which is constant w.r.t. Q^2.

Note that the parameters are poorly determined, although the fit quality as indicated by $\chi^2/$dof is acceptable. We can extract the order of magnitude of both κ_s^0 and $\tilde{E}_2$, but with large statistical uncertainty. On the other hand, we have found the extrapolated value of $F_2^s(Q^2 = 0, m_\pi^{\rm phys})$ to be fully compatible with experiment, having both the correct order of magnitude and the correct sign. We point out again that the forward value will not receive disconnected contributions, thus the value quoted corresponds directly to the experiment.

7. Summary of electromagnetic form factors

For the isovector form factors of the vector current we find that the lattice mean squared radii at present pion masses are significantly below the empirical ones. This finding is qualitatively compatible with chiral perturbation theory, though, since the latter predicts a sharp increase of the mean squared radii as the pion mass approaches the chiral limit. Although our data are consistent with one-loop expressions from both SSE and BChPT, we still require data at smaller pion masses and larger volumes to successfully compare with phenomenology and make predictions in the chiral limit with negligible systematic errors. For the isoscalar form factors of the vector currents we find our results to be in agreement with expectations from chiral expansions—the connected part of $F_1^s(Q^2)$ has a

TABLE XXIX. Dipole fits to isoscalar $F_1^s(Q^2)$ with varying fit intervals.

$[Q^2_{\rm min}, Q^2_{\rm max}]$ (GeV^2)	$\chi^2/$dof	A_0	M_d (GeV)	$\langle r_1^2\rangle$ (fm^2)
[0, 1.5]	1.20	3.0511(27)	1096.9(62)	0.3883(27)
[0, 0.5]	0.77	3.0518(27)	1098.6(65)	0.3871(46)
[0, 0.4]	0.90	3.0521(28)	1099.0(66)	0.3868(46)
[0, 0.3]	0.91	3.0516(29)	1070.0(67)	0.3883(47)
[0, 0.2]	0.76	3.0520(29)	1098.1(68)	0.3875(48)
[0, 1.5]	1.20	3.0511(27)	1096.9(62)	0.3883(27)
[0.1, 1.5]	1.18	3.0587(66)	1090.3(81)	0.3931(59)
[0.2, 1.5]	1.09	3.0356(14)	1103.4(109)	0.3838(76)
[0.3, 1.5]	0.57	3.0141(306)	1107.9(151)	0.3807(104)
[0.4, 1.5]	0.64	3.0522(799)	1097.8(248)	0.3877(175)
[0.3, 0.5]	0.30	3.0309(963)	1102.9(375)	0.3842(260)
[0.2, 0.4]	1.04	3.0430(204)	1102.2(135)	0.3853(98)
[0.1, 0.3]	0.85	3.0589(73)	1090.7(88)	0.3928(63)

TABLE XXX. Dipole fits to isoscalar $F_1^s(Q^2)$ for all data sets.

m_π (MeV)	$\chi^2/$dof	A_0	M_d (GeV)	$\langle r_1^2\rangle$ (fm^2)
293	1.08	3.0421(90)	1086.6(129)	0.3958(94)
356 on 28^3	1.20	3.0511(27)	1096.9(62)	0.3883(27)
356 on 20^3	2.46	3.0538(22)	1107.3(68)	0.3811(47)
495	1.78	3.0541(15)	1152.7(41)	0.3516(25)
597	1.27	3.0550(9)	1201.3(29)	0.3238(16)

TABLE XXXI. Fits to isoscalar $F_1^s(Q^2, m_\pi)$ at varying intervals of Q^2 with fixed pion-mass cut, $m_\pi < 400$ MeV.

Q^2 max (GeV^2)	χ^2/dof	$\tilde{B}_1$	$\langle r_1^2 \rangle$ (fm^2)
0.4	42.7	0.3304(23)	0.2631(18)
0.3	17.9	0.3493(25)	0.2782(20)
0.2	2.1	0.3878(47)	0.3089(38)

TABLE XXXII. Fit results to isoscalar form factor $F_2^s(Q^2)$ for the interval $Q^2 = [0, 0.5]$ GeV^2 and $m_\pi < 400$ MeV. The next-to-last line is our extrapolated result at the physical pion mass, and the last line lists the experimental value for $F_2^s(Q^2 = 0, m_\pi^{\rm phys})$.

	Fit result
χ^2/dof	1.34
κ_s^0	−0.36(25)
$\tilde{E}_2$ (GeV^{-3})	−0.32(29)
Extrap. $F_2^s(Q^2 = 0, m_\pi^{\rm phys})$	−0.32(21)
Exp. $F_2^s(Q^2 = 0, m_\pi^{\rm phys})$	−0.360 586 110(14)

nonvanishing Q^2 dependence, while the Q^2 dependence of $F_2^s(Q^2)$ was not measurable. The overall magnitude of $F_2^s(Q^2 = 0)$ is well in agreement with empirical information, albeit with large uncertainty.

C. Axial form factors

The nucleon axial current matrix element is also expressed in terms of two form factors: The axial form factor, $G_A(Q^2)$, and the induced pseudoscalar form factor, $G_P(Q^2)$. They correspond to the generalized form factors $\tilde{A}_{10}(Q^2)$ and $\tilde{B}_{10}(Q^2)$ in Eq. (9). For a review of the current experimental and theoretical understanding of the axial structure of the nucleon, we refer to Ref. [86]. For more details on the chiral effective field theory expressions that

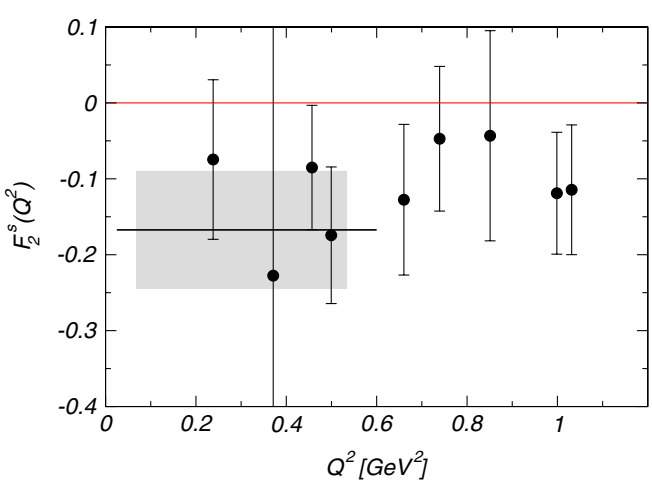

FIG. 22 (color online). Isoscalar form factor $F_2^s(Q^2)$ as a function of Q^2 with SSE fit at $m_\pi = 293$ MeV.

we will use in our fits, see Ref. [67]. For lattice results from other groups, see Ref. [81].

Like the vector current, the axial current needs to be renormalized. The renormalization coefficient can be computed from the conserved axial current; see Ref. [87]. Defining the two-point functions $C(T)$ and $L(T)$ of the conserved and local currents via

$$C(T + 1/2) = \sum_{\vec{x}} \langle \mathcal{A}_0(\vec{x}, T + 1/2)\pi(\vec{0}, 0)\rangle,$$
$$L(T) = \sum_{\vec{x}} \langle A_0(\vec{x}, T)\pi(\vec{0}, 0)\rangle, \tag{54}$$

the axial renormalization constant, Z_A, can then be computed from

$$Z_A(T) = \frac{1}{2}\left(\frac{C(T + 1/2) + C(T - 1/2)}{2L(T)} + \frac{2C(T + 1/2)}{L(T) + L(T + 1)}\right). \tag{55}$$

For large $T \gg 1$, the ratio in Eq. (55) becomes the axial renormalization constant, $Z_A \equiv \lim_{T\to\infty} Z_A(T)$. Based on the ensembles listed in Table I we have used the ranges $T = [12, 29]$ and $T = [35, 52]$ to obtain our final values of the renormalization constants. Table XXXIII summarizes our findings. We thus obtain a quark-mass dependent Z_A factor. Since all the ensembles considered here are at the same value of the lattice spacing a, the differences between the Z_A values in Table XXXIII are entirely due to quark-mass effects. To leading order these effects are expected to be linear in $am_{\rm q}$ [88], and it is important to keep at least this leading quark-mass dependence to avoid introducing $\mathcal{O}(a)$ discretization errors in the matrix elements of A_0.

We will now review the isovector axial form factor, $G_A(Q^2)$, in Sec. IV C 1, the induced pseudoscalar form factor, $G_P(Q^2)$, in Sec. IV C 2, and the two isoscalar axial form factors, $\tilde{A}_{10}(Q^2)$ and $\tilde{B}_{10}(Q^2)$, in Sec. IV C 3. Section IV C 4 summarizes our findings.

1. Isovector axial form factor $G_A(Q^2)$

The isovector axial form factor is usually fit by a dipole form. The forward value, $g_A = G_A(Q^2 = 0)$, has been discussed in detail in Sec. IV A. The dipole mass and its relevance to experiment has been studied in detail in Ref. [86]. Table XXXIV shows results of a series of fits to $G_A(Q^2)$ on the 28^3 lattice at $m_\pi = 356$ MeV. It is evident that the dipole form provides a good fit to the lattice data at all available values of the virtuality, Q^2. It turns out that the axial mass at $m_\pi = 356$ MeV is about 50% larger than the phenomenological value from neutrino scattering, $M_d = (1.026 \pm 0.021)$ GeV, and the one from electroproduction, $M_d = (1.069 \pm 0.016)$ GeV; see Ref. [86]. Hence, the situation is qualitatively similar to the case of the form factors of the vector current.

TABLE XXXIII. Renormalization constant of the axial currents.

$m_{\rm sea}^{\rm asqtad}$	Volume	Z_A
0.007/0.050	$20^3 \times 64$	1.0816
0.010/0.050	$28^3 \times 64$	1.0850
0.010/0.050	$20^3 \times 64$	1.0849
0.020/0.050	$20^3 \times 64$	1.0986
0.030/0.050	$20^3 \times 64$	1.1090

TABLE XXXV. Dipole fits to isovector $G_A(Q^2)$ for all data sets.

m_π (MeV)	χ^2/dof	A_0	M_d (GeV)	$\langle r_A^2\rangle$ (fm^2)
293	0.80	1.154(26)	1.577(56)	0.1879(134)
356 on 28^3	1.70	1.125(15)	1.587(29)	0.1856(67)
356 on 20^3	1.30	1.144(15)	1.661(33)	0.1694(68)
495	1.25	1.142(77)	1.654(16)	0.1708(34)
597	1.05	1.146(46)	1.686(11)	0.1644(21)

For the other ensembles, we obtain the results from the dipole fits at fixed pion mass summarized in Table XXXV. The data have been fit to all available Q^2. The large offset between lattice and phenomenology exhibited by the dipole masses, and thus also by the radii, remains to be explained.

We also study $G_A(Q^2, m_\pi)$ using the chiral expansion from Ref. [67]. At this order, the Q^2 dependence is linear and contains a counterterm which is directly related to the mean squared axial radius, $\langle r_A^2\rangle$. The pion-mass dependence is encoded in $g_A(m_\pi)$:

$$G_A(Q^2, m_\pi) = g_A(m_\pi) - \frac{Q^2}{(4\pi f_\pi)^2}\tilde{B}_3. \tag{56}$$

For the expression of $g_A(m_\pi)$ see Eq. (29). In the following we have performed fits of the Q^2 dependence of G_A at fixed pion masses and extracted the mean squared axial radii by taking

$$\langle r_A^2\rangle = \frac{-6}{g_A(m_\pi)} \frac{{\rm d}G_A(Q^2, m_\pi)}{{\rm d}Q^2}\bigg|_{Q^2=0}. \tag{57}$$

From the resulting series of fits we attempt to extract a sensible interval for the fitting range of Q^2. First we determine the upper cutoff in Q^2 on the 28^3 lattice. The results are listed in Table XXXVI. Since the fit expression is only linear, the exclusion of points at larger Q^2 does indeed improve the quality of the fit, although the overall result is not as satisfactory as for the dipole fit. Both for g_A and for $\langle r_A^2\rangle$ we find that the chiral fit lies below the results from the dipole fits. Furthermore, the fits in this section possess larger uncertainties and the resulting χ^2/dof is worse.

Now, we apply the SSE fit simultaneously to the entire available data set. From the previous section we have learned that $Q^2 = [0, 0.4]$ GeV^2 is a sensible fitting interval which we keep in the following. When varying the upper cutoff in m_π, we obtain the fit results in Table XXXVII.

Graphically, Fig. 23 shows the results of the chiral fit together with a dipole fit and the data set for the 28^3 lattice at $m_\pi = 356$ MeV. The fitting range is $Q^2 = [0, 0.4]$ GeV^2 and $m_\pi < 400$ MeV for the SSE expression and all Q^2 values for the dipole fit. The plot illustrates that the dipole fit works well and that the SSE NLO result is linear in Q^2 and provides a good description of lattice data only for relatively small values of Q^2. There is a rather weak sensitivity to the pion mass, but we need to point out that we do not at all reproduce the value $\tilde{B}_3 = 3.08(27)$ from Ref. [67] determined from the experimental value of the axial radius $\langle r_A^2\rangle = 0.409(12)$ fm^2 (from electroproduction) at the physical pion mass.

To summarize, we find that $G_A(Q^2)$ is described excellently using a dipole-type fit, but the axial radius is substantially smaller than the experimental one. The SSE expansion simply gives a linear dependence in Q^2—it can thus be applied only to small values of Q^2, where the functional behavior is approximately linear. At fixed m_π,

TABLE XXXIV. Dipole fits to isovector $G_A(Q^2)$ with varying fit intervals.

$[Q^2_{\rm min}, Q^2_{\rm max}]$ (GeV^2)	χ^2/dof	g_A	M_d (GeV)	$\langle r_A^2\rangle$ (fm^2)
[0, 1.5]	1.70	1.1245(147)	1.587(29)	0.1856(67)
[0, 0.5]	1.77	1.1334(158)	1.545(31)	0.1956(79)
[0, 0.4]	2.22	1.1343(160)	1.536(34)	0.1980(89)
[0,0.3]	1.71	1.1331(161)	1.550(39)	0.1945(97)
[0, 0.2]	2.25	1.1308(163)	1.508(47)	0.2056(13)
[0, 1.5]	1.70	1.1245(147)	1.587(29)	0.1856(67)
[0.1, 1.5]	1.79	1.1247(150)	1.587(29)	0.1856(68)
[0.2, 1.5]	1.43	1.1303(168)	1.584(33)	0.1862(78)
[0.3, 1.5]	0.53	1.1123(228)	1.598(50)	0.1830(115)
[0.3, 0.5]	0.54	1.1005(642)	1.617(17)	0.1787(369)
[0.2, 0.4]	1.71	1.1533(209)	1.496(49)	0.2088(136)
[0.1, 0.3]	2.01	1.1305(171)	1.563(49)	0.1913(120)

TABLE XXXVI. Chiral fit to $G_A(Q^2, m_\pi = 356\ \text{MeV})$ with varying upper cutoff in Q^2.

Q^2 max (GeV^2)	χ^2/dof	$\tilde{B}_3$	$\langle r_A^2\rangle(m_\pi = 356\ \text{MeV})$ (fm^2)
1.5	4.82	0.725(23)	0.1269(38)
0.5	2.66	0.848(33)	0.1485(46)
0.4	2.67	0.901(39)	0.1577(57)
0.3	2.52	0.949(47)	0.1660(71)
0.2	1.50	1.094(70)	0.1914(11)

TABLE XXXVII. Chiral fits to $G_A(Q^2)$ at fixed interval $Q^2 = [0, 0.4]$ GeV^2 with varying upper cutoff in m_π.

m_π max (MeV)	χ^2/dof	$\tilde{B}_3$	$\langle r_A^2\rangle(m_\pi = 293\ \text{MeV})$ (fm^2)
300	0.71	0.993(130)	0.1707(193)
400	1.73	0.908(32)	0.1560(60)
500	1.54	0.891(20)	0.1531(49)
600	1.76	0.847(12)	0.1457(42)

the fit quality is acceptable. When performing a combined fit in Q^2 and m_π, we still find that the axial radius is substantially underestimated; we also detect a small residual pion-mass dependence that is not present in the SSE expression at the given order since at this order one should take $g_A(m_\pi) = g_A = 1.2$ (cf. Table VIII) in the denominator of Eq. (57).

2. Isovector pseudoscalar form factor

This section discusses fit results to the induced pseudoscalar form factor, $G_P(Q^2, m_\pi)$. We will first focus on the isovector case. Unlike the other form factors, the chiral expansion of $G_P(Q^2, m_\pi)$ includes a pion-pole term [67,81]:

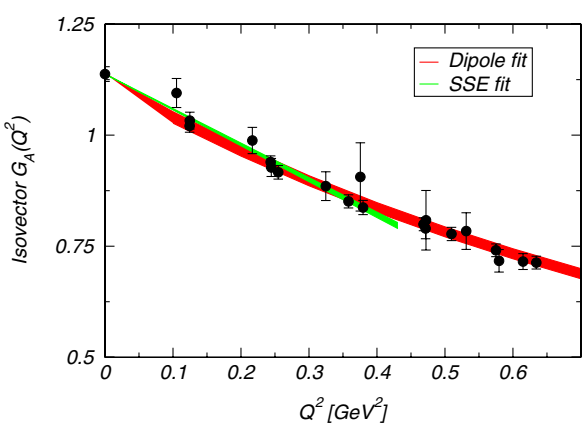

FIG. 23 (color online). Comparison of dipole and chiral fit to $G_A(Q^2)$ for the 28^3 lattice at $m_\pi = 356$ MeV.

$$G_P(Q^2, m_\pi) = \frac{4m_N^2}{m_\pi^2 + Q^2}\left(g_A - \frac{2m_\pi^2\tilde{B}_2}{(4\pi f_\pi)^2}\right) - \frac{2}{3}g_A m_N^2\langle r_A^2\rangle. \tag{58}$$

This NLO expression has two fit parameters, $\tilde{B}_2$ and $\langle r_A^2\rangle$. The former parameter, $\tilde{B}_2$, is a correction to the residue of the pion pole. The parameter $\langle r_A^2\rangle$ is the axial radius encountered above in the axial form factor and induces an overall shift.

As discussed previously, we first perform a series of fits on the 28^3 lattice at fixed $m_\pi = 356$ MeV and vary the upper cutoff in Q^2. For the input parameters to expression (58) see Table VIII. This will give us an understanding of how far the chiral expansion can be expected to hold, although we always have to keep in mind that any agreement for Q^2 larger than 0.5 GeV^2 should be considered merely accidental. Table XXXVIII summarizes the results.

The overall quality of the fit is good and χ^2/dof acceptable. However, we notice that the axial radius, $\langle r_A^2\rangle$, is smaller than the one obtained using the axial form factor, $G_A(Q^2, m_\pi)$. It appears that the NLO SSE formula is not able to connect our data to experiment for that observable.

With a fixed fit interval $Q^2 = [0, 0.5]$ GeV^2 we also performed a combined fit in Q^2 and m_π and varied the upper cutoff for the latter. Note that in this case, the location of the pion pole varies and is set to the appropriate value for each ensemble under consideration. Table XXXIX summarizes our findings. We find the fit formula applicable with the cuts $Q^2 = [0, 0.5]$ GeV^2 and $m_\pi < 400$ MeV.

Next, we study the location of the pole in Eq. (58). Whereas in the previous fits the measured pion mass was used to fix the dependence, we can also treat the pole position as a free parameter. For this study, we choose the fit interval $Q^2 = [0, 0.5]$ GeV^2 on the 28^3 lattice and obtain the results in Table XL. It is evident that there is an uncertainty of about 10%, but within this uncertainty, we find that the location of the pion pole is reproduced. We compare the fits with varying pole positions in Table XL and with a fixed pole position in Table XXXVIII for the interval $Q^2 = [0, 0.5]$ GeV^2 graphically in Fig. 24.

Our overall conclusion is that the isovector $G_P(Q^2)$ form factor can be well described by the pion-pole expression. We find that by applying the cuts $Q^2 = [0, 0.5]$ GeV^2 and $m_\pi < 400$ MeV we obtain acceptable results. Allowing the

TABLE XXXVIII. Pion-pole fits to the isovector pseudoscalar form factor $G_P(Q^2, m_\pi = 356\ \text{MeV})$ on the 28^3 lattice.

Q^2 max (GeV^2)	χ^2/dof	$\tilde{B}_2$	$\langle r_A^2\rangle$ (fm^2)
1.5	1.26	−0.96(13)	0.107(8)
0.5	1.08	−1.01(17)	0.108(14)
0.4	1.22	−0.84(22)	0.088(21)
0.3	0.84	−0.55(31)	0.051(35)

TABLE XXXIX. Chiral fits to $G_P(Q^2)$ at fixed interval $Q^2 = [0, 0.5]$ GeV^2 with varying upper cutoff in m_π.

m_π max (MeV)	χ^2/dof	$\tilde{B}_2$	$\langle r_A^2 \rangle$ (fm^2)
300	1.13	−0.10(80)	0.058(46)
400	1.72	−0.94(15)	0.089(12)
500	2.85	−1.544(87)	0.113(9)
600	3.14	−1.875(56)	0.139(7)

TABLE XL. Result from fit of isovector $G_P(Q^2)$ to pion-pole form with variable pole mass parameter.

	Fit result
χ^2/dof	0.94
$\tilde{B}_2$	−1.98(61)
$\langle r_A^2 \rangle$ (fm^2)	0.192(65)
Fit result m_π (MeV)	417(43)
Actual ensemble m_π (MeV)	356

pion pole to vary freely, we obtain a result compatible with the "true" pion mass, albeit slightly higher.

3. Isoscalar axial form factors

When considering the forward case of the isoscalar axial form factors, we recover the connected part of the first moment of the spin-dependent isoscalar parton distribution which we discuss thoroughly in Sec. IV D. Their Q^2 dependence is not known experimentally, but they have been studied in the framework of chiral perturbation theory. Reference [89] finds a counterterm with a linear Q^2 dependence, and Ref. [90] does not list any Q^2 dependence at the order considered. In a previous paper [91], however, the same authors find a counterterm with linear Q^2 dependence, in agreement with Ref. [89]. In the following we adopt the notation from Eq. (9) when referring to the two form factors; i.e. we denote them by $\tilde{A}_{10}(Q^2)$ and $\tilde{B}_{10}(Q^2)$.

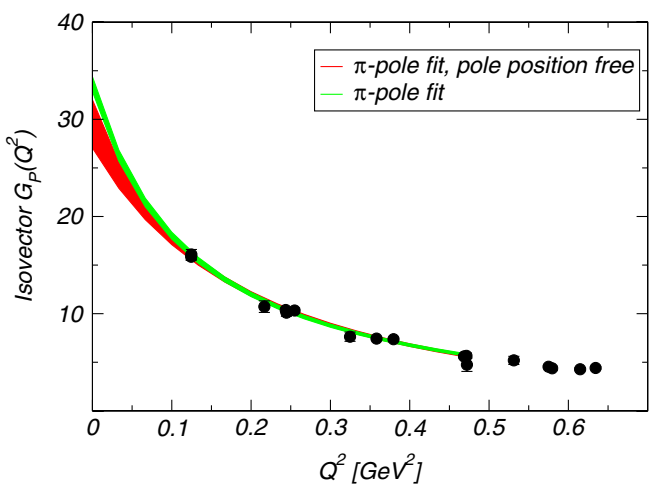

FIG. 24 (color online). Comparison of pion-pole fits to isovector $G_P(Q^2)$ on the 28^3 lattice with fixed pion pole and with the pion pole as a free parameter.

Isoscalar axial form factor $\tilde{A}_{10}$.—

Since the m_π dependence of the forward matrix element is already covered in Sec. IV D, we focus on the Q^2 dependence at each ensemble. First, we study the case $m_\pi = 356$ MeV on the 28^3 lattice. As a generic fit formula we use the dipole expression. Figure 25 displays the result of the fit. Notice that this figure contains an example for six data points that appear superficially high as discussed previously in Ref. [41]; cf. also Sec. III C. The dipole form actually provides a decent description of the data. We find a dipole mass of $M_d = 1683(89)$ MeV with $\chi^2/\text{dof} = 1.87$. Unlike the isovector form factors of the vector current, we cannot refer to previous phenomenological fits of experimental data. Our results for the dipole fits to the different ensembles are listed in Table XLI. The radii thus obtained are denoted by $\langle \tilde{r}_1^2 \rangle$.

Isoscalar axial form factor $\tilde{B}_{10}$.—

For the connected part of the isoscalar form factor $\tilde{B}_{10}(Q^2)$ of the axial current we also find a nontrivial Q^2 dependence. In this case, however, we observe that the form factor has quite a large magnitude and a rather strong falloff. Again, we attempt a dipole-type fit and display the result in Fig. 26. The dipole appears to fit the connected part well with $\chi^2/\text{dof} = 1.88$. However, since the functional form is suggestive of the pion pole (cf. Equation (58) in Sec. IV C 3), we have also attempted a fit to that form. If we keep the pion pole fixed to the actual pion mass of the sample, $m_\pi = 356$ MeV, we obtain a $\chi^2/\text{dof} = 1.86$, whereas leaving it a free parameter gives $\chi^2/\text{dof} = 1.97$ with a measured position of $m_\pi = 394(59)$ MeV. This result is certainly in agreement with the actual pion mass of the underlying ensemble. This indicates that the

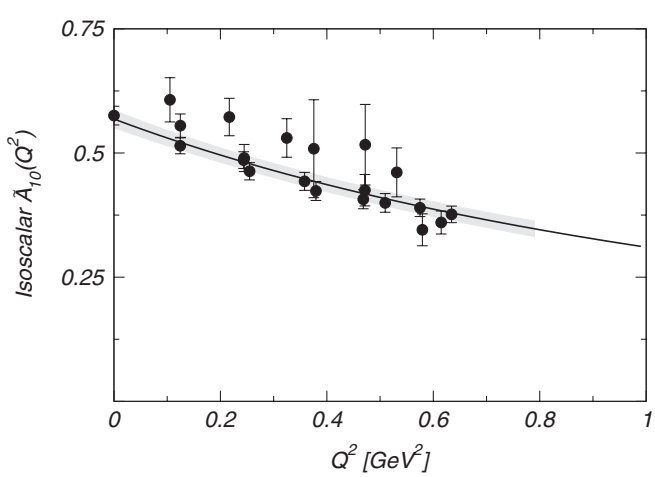

FIG. 25. Dipole fit to the isoscalar axial form factor $\tilde{A}_{10}(Q^2)$ on the 28^3 lattice at $m_\pi = 356$ MeV.

TABLE XLI. Dipole fits to isoscalar $\tilde{A}_{10}(Q^2)$ for all data sets.

m_π (MeV)	χ^2/dof	A_0	M_d (GeV)	$\langle \tilde{r}_1^2 \rangle$ (fm^2)
293	1.45	0.560(31)	1.626(143)	0.176(31)
356 on 28^3	1.87	0.568(18)	1.683(89)	0.165(17)
356 on 20^3	1.58	0.542(17)	1.903(97)	0.129(13)
495	1.10	0.586(9)	1.711(40)	0.1596(75)
597	0.75	0.605(6)	1.691(26)	0.1635(51)

TABLE XLII. Dipole fits to isoscalar $\tilde{B}_{10}(Q^2)$ for all data sets.

m_π (MeV)	χ^2/dof	A_0	M_d (GeV)	$\langle \tilde{r}_2^2 \rangle$ (fm^2)
293	0.65	13.3(37)	0.671(95)	1.04(30)
356 on 28^3	1.88	13.14(85)	0.668(22)	1.05(7)
356 on 20^3	1.22	11.4(11)	0.757(36)	0.82(8)
495	1.15	10.44(54)	0.802(23)	0.73(4)
597	0.89	10.27(34)	0.840(17)	0.66(3)

connected part of the isoscalar $\tilde{B}_{10}(Q^2)$ form factor is indeed compatible with a pion-pole form, although the data do not favor it over a dipole form.

The resulting parameters from dipole fits to all data sets are assembled in Table XLII. It is evident that there is a notable pion-mass dependence, with the dipole mass being affected strongest. This is in line with the functional form in Ref. [89], although the strength of the effect is quite surprising. At $m_\pi = 293$ MeV the mean squared radius, $\langle \tilde{r}_2^2 \rangle$, is larger than 1 fm, making it the largest radius of all observables. Further studies of the chiral behavior for this observable and the computation of disconnected diagrams are interesting directions for future work to shed further light on these observations.

4. Summary of axial form factors

The isovector axial form factor $G_A(Q^2, m_\pi)$ at present lattice pion masses systematically is much flatter as a function of Q^2 than experiment, and this result is not explained by one-loop chiral perturbation theory. This is a qualitative and significant quantitative mismatch between lattice and phenomenology that still remains to be understood. The corresponding pseudoscalar form factor $G_P(Q^2, m_\pi)$ is described very well by a pion-pole form, and both the functional form and the location of the pion pole are in excellent agreement with theory. Still, the SSE cannot explain the discrepancy in the axial radii we extract from G_A and G_P. The connected parts of the isoscalar form factors of the axial current have a strong Q^2 dependence, and we have successfully used dipole forms in each case.

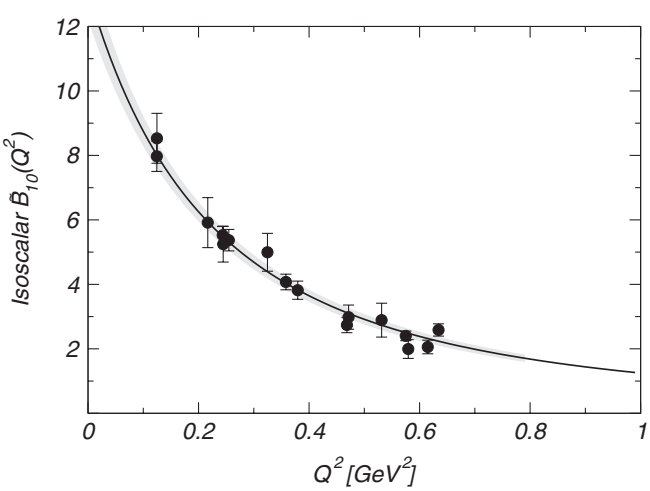

FIG. 26. Dipole fit to the isoscalar axial form factor $\tilde{B}_{10}(Q^2)$ on the 28^3 lattice at $m_\pi = 356$ MeV.

D. Generalized form factors

In this section we present a survey of our results for the generalized form factors, emphasizing their main qualitative features and describing the progress made since our previous publication on the subject [20].

We start with the form factors of the twist-two quark bilinear operator $\bar{q}D_{\{\mu}\gamma_{\nu\}}q$. This operator is particularly important since its forward matrix elements determine the quark momentum fractions; in the isosinglet case, it is one of the terms appearing in the energy-momentum tensor. Furthermore its forward matrix elements contribute to the nucleon mass [92] and spin decompositions; see Sec. IV E. The three form factors A_{20}, B_{20}, C_{20}, which determine its matrix elements between two arbitrary one-nucleon states via Eq. (6), are displayed in Fig. 27 both for the isovector and isosinglet combinations. In the latter case, our computation lacks contributions from the disconnected diagrams.

Similarly, the form factors $\tilde{A}_{20}$ and $\tilde{B}_{20}$ associated with the corresponding twist-two axial operator $\bar{q}D_{\{\mu}\gamma_{\nu\}}\gamma_5 q$ [see (7)] are displayed in Fig. 28. The forward matrix elements of this operator determine the first moments of the polarized structure functions, in other words, the polarized momentum fraction. As is clear from Eqs. (6) and (7), only the A_{20} and $\tilde{A}_{20}$ form factors can be directly obtained at zero momentum transfer; the others require an extrapolation, much as the Pauli form factor.

The statistical uncertainties on A_{20}, B_{20}, C_{20} at $m_\pi =$ 356, 495, and 597 MeV are reduced by about a factor of 3 as compared to our previous publication [20]. Furthermore we have data at one lighter pion mass, 293 MeV, with an accuracy comparable to our previous data in the 600–700 MeV range. Given the expected rapid deterioration of the signal-to-noise ratio when $m_\pi \to 0$, this represents significant progress.

Similar remarks apply to the axial GFFs $\tilde{A}_{20}$ and $\tilde{B}_{20}$. The signal-to-noise ratio of the latter GFF is overall quite poor and worsens visibly with the pion mass. While previously we were essentially unable to obtain a signal below $m_\pi = 500$ MeV, we now dispose of some information down to about $m_\pi = 350$ MeV.

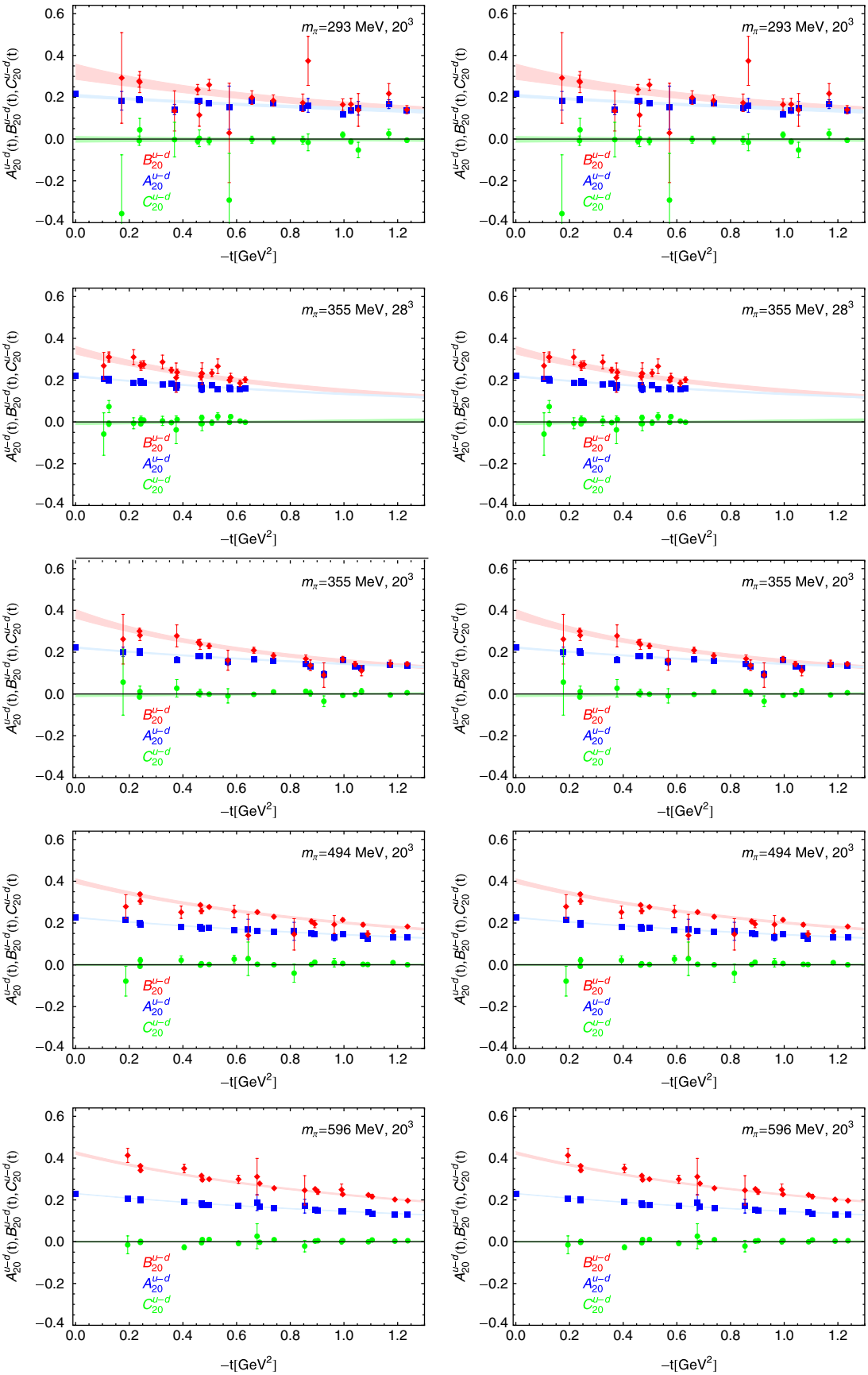

FIG. 27 (color online). The unpolarized isovector and isosinglet GFFs A_{20}, B_{20}, C_{20}.

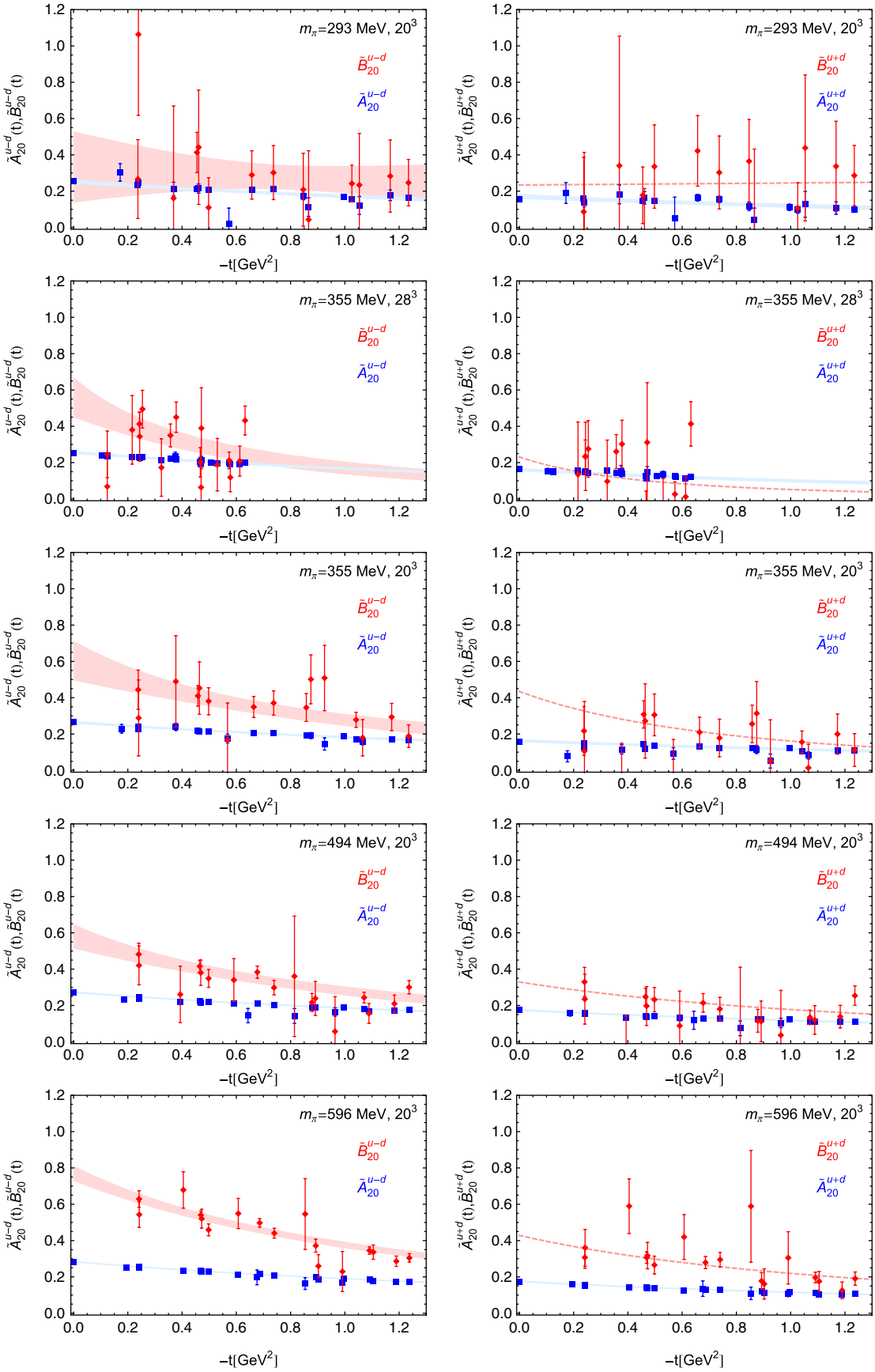

FIG. 28 (color online). The polarized isovector and isosinglet GFFs $\tilde{A}_{20}$ and $\tilde{B}_{20}$.

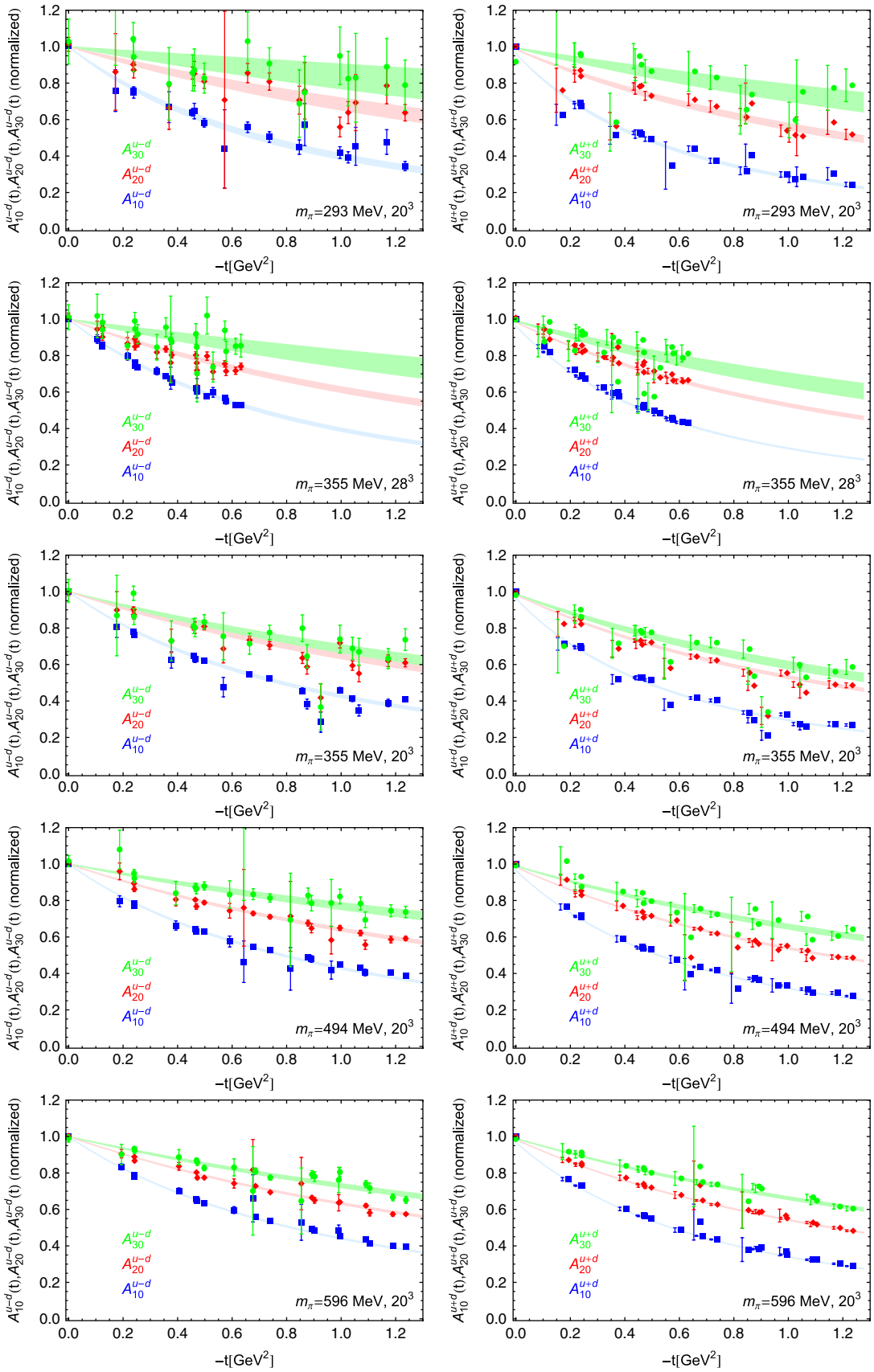

FIG. 29 (color online). Generalized form factors of twist-two operators of dimensions 3, 4, and 5, in the isovector and isosinglet channels. Notice, in particular, the flattening of the slope of the A_{n0} GFF with increasing n.

As in our previous work, we observe a qualitative agreement of the relative magnitudes of the GFFs with predictions from large N_c counting rules, e.g.

$$\begin{aligned} |A_{20}^{u+d}| &\sim N_c^2 \gg |A_{20}^{u-d}| \sim N_c, \\ |B_{20}^{u-d}| &\sim N_c^3 \gg |B_{20}^{u+d}| \sim N_c^2, \\ |C_{20}^{u+d}| &\sim N_c^2 \gg |C_{20}^{u-d}| \sim N_c. \end{aligned} \tag{59}$$

As a matter of fact, we remark that C_{20} is consistent with zero in the isovector channel, whereas it is clearly nonvanishing and negative in the isosinglet channel. This is of interest, since C_{20} entirely determines the longitudinal momentum transfer ξ dependence of the functions $H^{n=2}(\xi, t)$ and $E^{n=2}(\xi, t)$; see Eq. (8). In the case of B_{20}, it is the opposite: B_{20} is very small in the isosinglet channel, but it is positive and quite large (compared to A_{20}) in the isovector channel. However, B_{20}^{u-d} falls off faster than A_{20}^{u-d}, so that the two form factors are practically equal by the time $|t| \approx 1$ GeV^2 is reached, for pion masses ≤ 356 MeV. Their t dependence is thus qualitatively similar to the Q^2 dependence of the electromagnetic form factors, for which chiral perturbation theory predicts that $\langle r_1^v \rangle^2 \sim \log m_\pi$, and $\langle r_2^v \rangle^2 \sim 1/m_\pi$, and experimentally, it is indeed the case that $\langle r_1^v \rangle^2 < \langle r_2^v \rangle^2$.

In the polarized case, the large-N_c counting rules predict

$$\begin{aligned} |\tilde{A}_{20}^{u-d}| &\sim N_c^2 \gg |\tilde{A}_{20}^{u+d}| \sim N_c, \\ |\tilde{B}_{20}^{u-d}| &\sim N_c^4 \gg |\tilde{B}_{20}^{u+d}| \sim N_c^3. \end{aligned} \tag{60}$$

Our lattice data show that the isovector GFFs are only marginally larger in magnitude than the corresponding isosinglet GFFs. We further observe in both the isovector and isosinglet channel that $\tilde{B}_{20}(t) > \tilde{A}_{20}(t)$. Noting that $\tilde{H}^{n=2} = \tilde{A}_{20}$ and $\tilde{E}^{n=2} = \tilde{B}_{20}$ [see Eq. (9)], this is compatible with a dominance of the GPD $\tilde{E}$ over $\tilde{H}$ at small $-t$ as indicated in a recent HERMES study [93].

It is also interesting to compare the size of corresponding polarized and unpolarized form factors. The large-N_c ordering is indeed observed if one compares A_{20}^{u-d} with $\tilde{A}_{20}^{u-d}$, or B_{20}^{u-d} with $\tilde{B}_{20}^{u-d}$, but the differences in magnitude are not pronounced enough to speak of a hierarchy.

The momentum transfer dependence of the GFFs A_{10}, A_{20}, A_{30} is compared in Fig. 29 for both the isovector and isoscalar channels. For this purpose they all have been rescaled to be equal to unity at $t = 0$. It is clear that in both channels, the form factor flattens when the moment n increases. The effect is observed at all pion masses, and it is larger when increasing n from 1 to 2 than when going from $n = 2$ to $n = 3$.

This observation can be made more quantitative by fitting the GFFs with a dipole ansatz for $|t|$ ranging from zero to 0.5 GeV^2. In the isovector channel this leads, via the analogue of Eq. (36), to the squared radii displayed in Fig. 30. The left panel corresponds to unpolarized GFFs, the right panel to the polarized ones. In the infinite momentum frame, the transverse radii correspond to the rms transverse distance (i.e. the impact parameter) of the active parton to the center of momentum of the nucleon. At each pion mass, the higher the moment of the structure function, the smaller the radius associated with it. This effect had been anticipated [38] and was seen by direct lattice calculation for the first time in [2]. Indeed most of the contribution to higher moments comes from the large-x region; a parton carrying by itself most of the nucleon's momentum must be located near the center of mass in the transverse plane.

On the $V = 20^3$ lattices, corresponding to physical volumes of $(2.5\ \text{fm})^3$, it is only for the electromagnetic radius, $n = 1$, that we find a statistically significant increase when the pion mass is reduced. This corresponds to the idea that the growth of the nucleon radius with decreasing quark

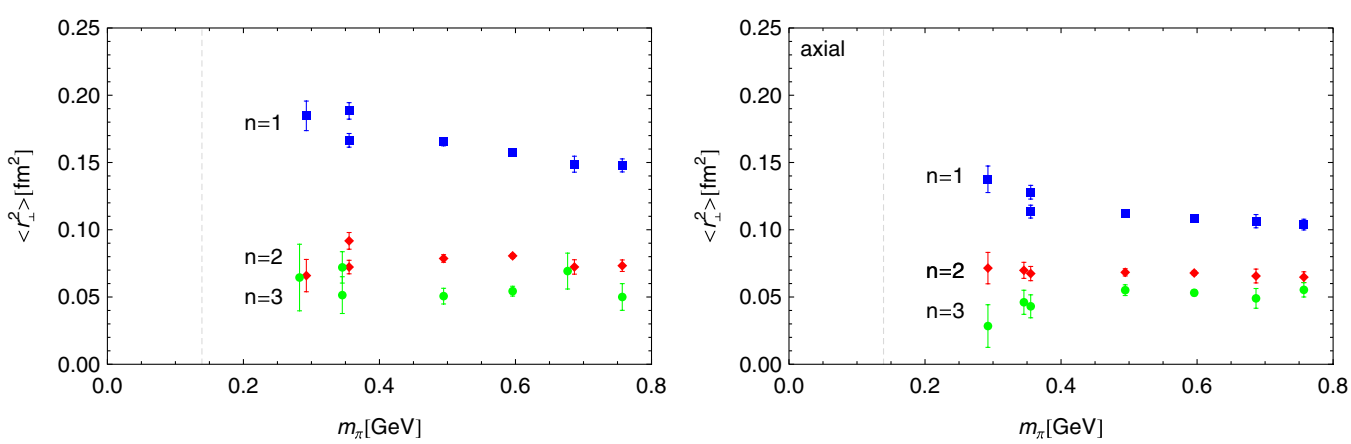

FIG. 30 (color online). Transverse isovector radii as extracted from a dipole fit with momentum cut $|t| < 0.5$ GeV^2. The left panel corresponds to the unpolarized case, and the right panel to the polarized case. At $m_\pi = 356$ MeV, the radius on the 28^3 lattice is in all cases larger than on the 20^3 lattice.

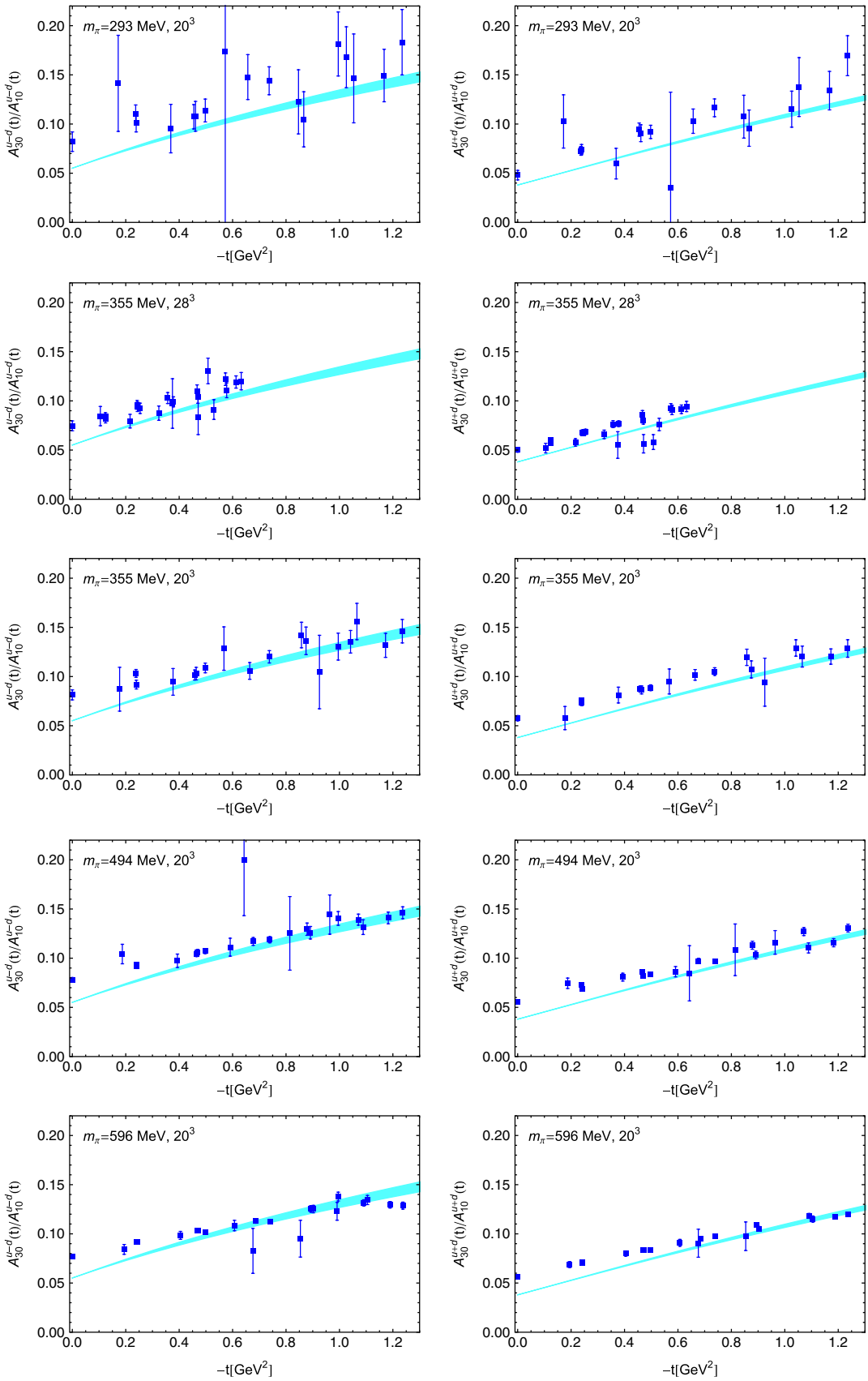

FIG. 31 (color online). Ratio of the A_{30} to the A_{10} unpolarized GFFs, isovector and isosinglet. Disconnected contributions have been omitted.

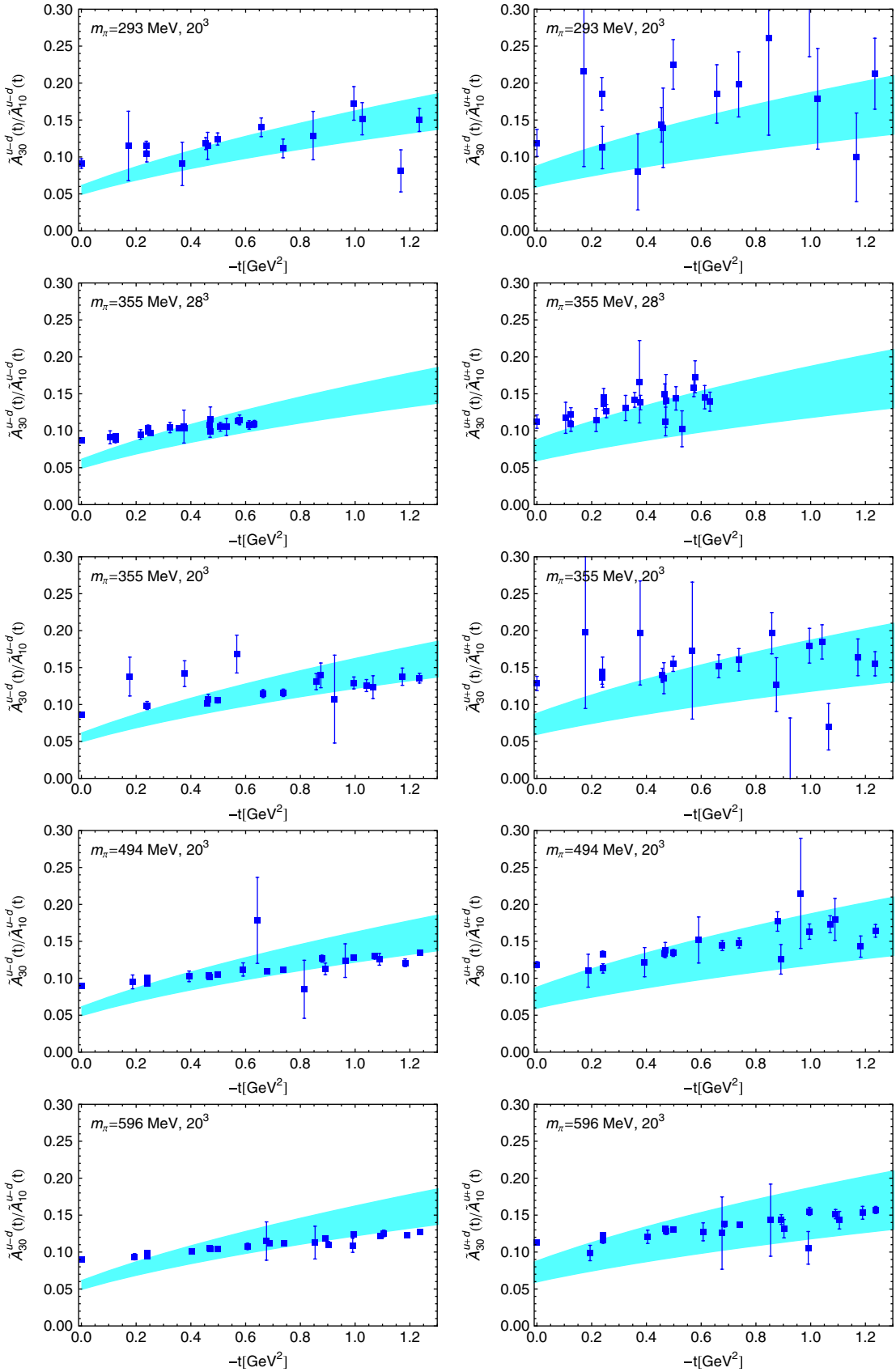

FIG. 32 (color online). Ratio of the $\tilde{A}_{30}$ to the $\tilde{A}_{10}$ polarized GFFs, isovector and isosinglet. Disconnected contributions have been omitted.

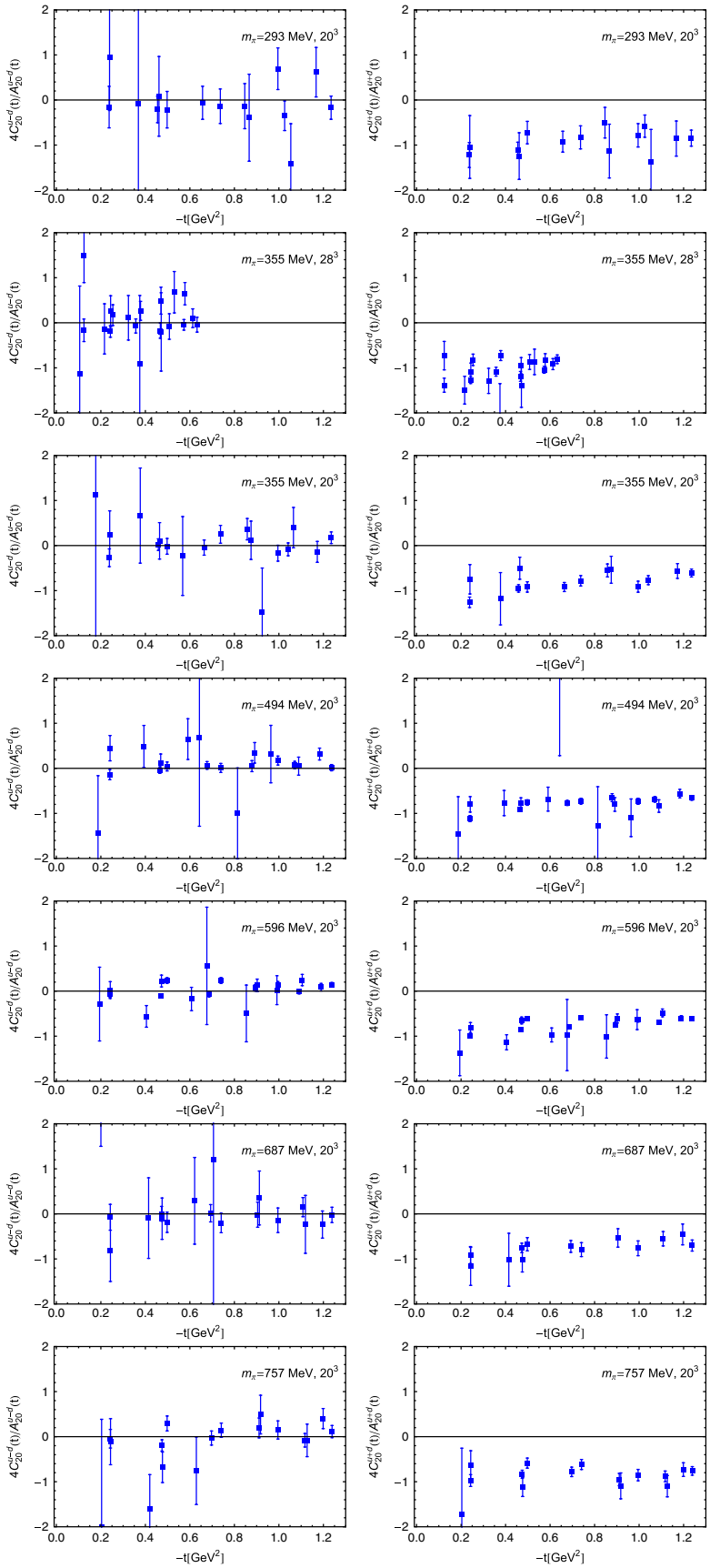

FIG. 33 (color online). Ratios of $n = 2$ generalized form factors.

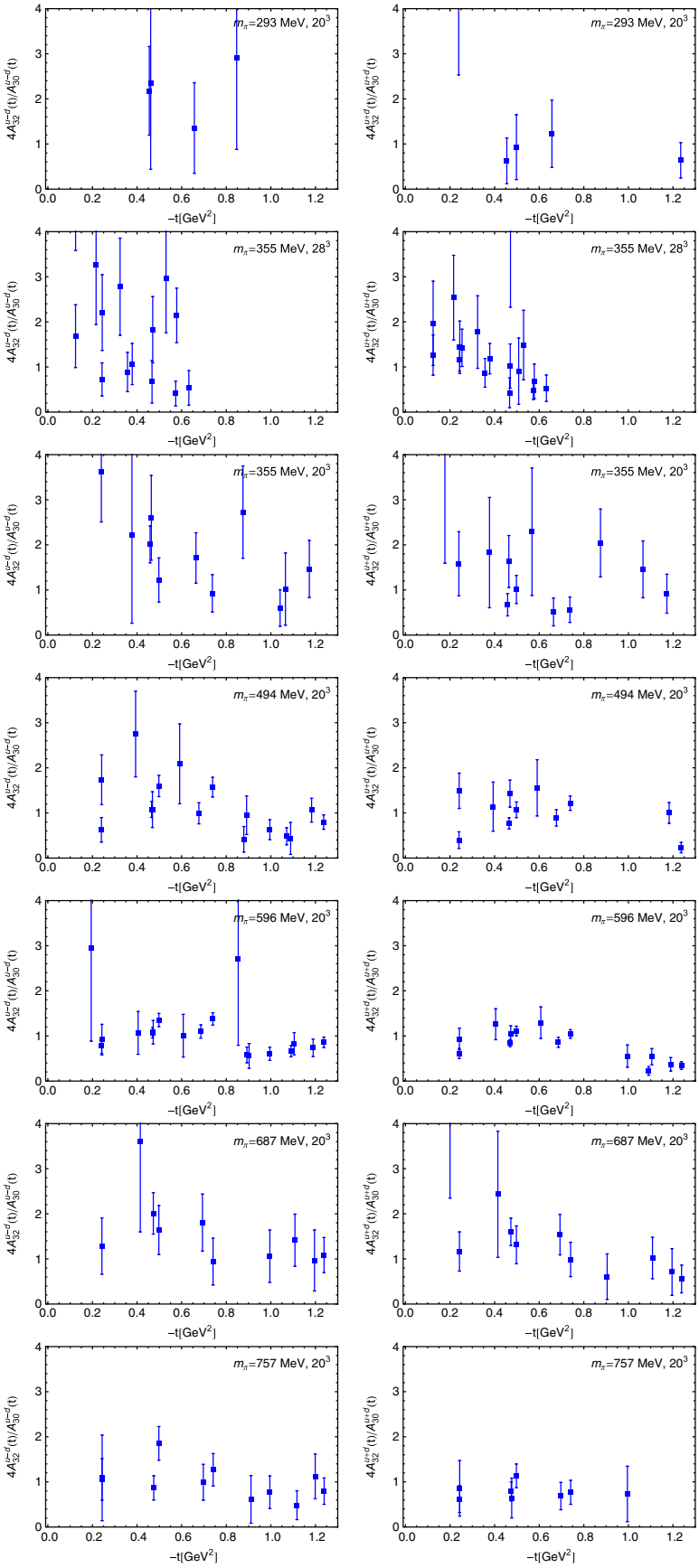

FIG. 34 (color online). Ratios of $n = 3$ generalized form factors.

mass is due to the low-x partons, while the large-x "valence" partons have a transverse distribution that depends only weakly on the quark mass. However, these qualitative lessons are questionable due to the statistically significant finite-size effect observed in several of these radii. The larger lattice volume $V = 28^3$, corresponding to $(3.5\ \mathrm{fm})^3$, leads to larger radii. The largest finite-size effect is seen in the vector and axial-vector form factors [see Sec. III E], but a similar effect is also seen in the A_{20} form factor. It appears that the nucleon is somewhat "squeezed" by the periodic box in which we study it, leading to an underestimation of the radii. This finite-size effect is not statistically significant if one simply extracts an effective square radius from the smallest available momentum transfer $q = 2\pi/L$, as we already pointed out in [9]. The finite-size effect affects the intermediate values of $-t$ most strongly, as discussed in Sec. III E. We believe that this apparently t-dependent finite-size effect on form factors is interesting and deserves further investigation.

Regarding Fig. 30 we also note that the $n = 2$ and 3 polarized radii at $m_\pi = 356$ MeV are statistically compatible with the corresponding unpolarized ones. This is in contrast with the $n = 1$ case, where the Dirac radius is significantly larger than the axial-vector radius. In the chiral limit, the Dirac radius diverges logarithmically, while the axial-vector radius remains finite; see Secs. IV B and IV C. Therefore, the former must become larger than the latter below a certain pion mass. What we see on Fig. 30 is that this hierarchy survives up to very large pion masses, far beyond the range of validity of the argument based on chiral effective theory.

As in [20], we have compiled data on the ratios $A_{30}(t)/A_{10}(t)$ and $\tilde{A}_{30}(t)/\tilde{A}_{10}(t)$ in Figs. 31 and 32, respectively, where we compare them to predictions based on experimental data for the nucleon form factors and PDFs in combination with a model-dependent ansatz for the combined (x, t) dependence of the GPDs, displayed by the error bands [94]. With increased statistics, even at the lightest pion mass there is good evidence that these ratios are generically not flat. A flat ratio would be a direct consequence of the factorization of the GPDs into an x-dependent function and a t-dependent function. In spite of a semiquantitative agreement, we see that the predictions of Diehl *et al.* [94] are systematically steeper than the lattice data, in particular, at small $-t$. This is most probably related to the fact that the lattice data for the radii at the accessible pion masses are systematically below the experimental values. We further observe that the ratio of polarized GFFs is flatter than the unpolarized one (see, for instance, the $m_\pi \simeq 600$ MeV graph, where the data are rather accurate).

Figures 33 and 34 display, respectively, the ratios of GFFs C_{20}/A_{20} and A_{32}/A_{30}, both in the isovector and isosinglet channels. We have already remarked that C_{20} is consistent with zero in the isovector channel; however, in the isosinglet channel, the ratio $4C_{20}/A_{20}$ is of the order of -1. This makes the ξ dependence of $H^{n=2}(\xi, t)$ and $E^{n=2}(\xi, t)$ an order unity effect [see Eq. (8)], which is of great interest due to its direct relation to the frequently discussed D term [95]. For the next higher moment, $n = 3$, the data are rather noisy, but at $m_\pi = 495$ MeV and $m_\pi = 597$ MeV, it is nevertheless clear that $4A_{32}/A_{30}$ is positive, and most likely of order $+1$. Thus the ξ dependence of $H^{n=3}(\xi, t)$ is also substantial, and goes in the other direction compared to the $n = 2$ sector.

1. BChPT extrapolation of A_{20}^{u-d}, B_{20}^{u-d}, C_{20}^{u-d}

In this section we discuss the forward and small $-t$ behavior of the generalized form factors A_{20}^{u-d}, B_{20}^{u-d}, and C_{20}^{u-d}. In particular, $A_{20}^{u-d}(t = 0)$ is the isovector momentum fraction $\langle x\rangle_{u-d}$. The main novelty as compared to [20] is that we now have sufficiently accurate data below $m_\pi = 500$ MeV to test the applicability of covariant BChPT in that regime exclusively. In Ref. [20], the fit range extended up to $m_\pi = 700$ MeV.

The $\mathcal{O}(p^2)$ BChPT result [75] for the isovector GFFs $\{A, B, C\}_{20}^{u-d}(t)$ is

$$A_{20}^{u-d}(t, m_\pi) = A_{20}^{0,u-d}\left(f_A^{u-d}(m_\pi) + \frac{g_A^2}{192\pi^2 f_\pi^2} h_A(t, m_\pi)\right) + \tilde{A}_{20}^{0,u-d} j_A^{u-d}(m_\pi) + A_{20}^{m_\pi,u-d} m_\pi^2 + A_{20}^{t,u-d} t, \tag{61}$$

$$B_{20}^{u-d}(t, m_\pi) = \frac{m_N(m_\pi)}{m_N} B_{20}^{0,u-d} + A_{20}^{0,u-d} h_B^{u-d}(t, m_\pi) + \frac{m_N(m_\pi)}{m_N}\{\delta_B^{t,u-d} t + \delta_B^{m_\pi,u-d} m_\pi^2\}, \tag{62}$$

$$C_{20}^{u-d}(t, m_\pi) = \frac{m_N(m_\pi)}{m_N} C_{20}^{0,u-d} + A_{20}^{0,u-d} h_C^{u-d}(t, m_\pi) + \frac{m_N(m_\pi)}{m_N}\{\delta_C^{t,u-d} t + \delta_C^{m_\pi,u-d} m_\pi^2\}. \tag{63}$$

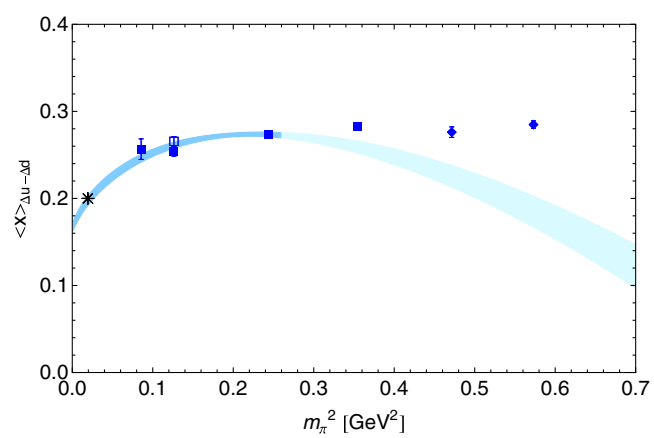

FIG. 35 (color online). The extrapolation of the polarized momentum fraction using HBChPT. The value obtained in the chiral limit is 0.165(8), and the experimental value is from HERMES [49].

Here $f_A^{u-d}(m_\pi)$, $h_{A,B,C}(t, m_\pi)$, and $j_A^{u-d}(m_\pi)$ contain the nonanalytic dependence on the pion mass and momentum transfer squared [see, for instance, Eqs. (28), (40), and (41) of [75]], while $A_{20}^{0,u-d} \equiv A_{20}^{u-d}(t = 0, m_\pi = 0)$, $A_{20}^{m_\pi,u-d}$, and $A_{20}^{t,u-d}$ are low-energy constants. Similarly $B_{20}^{0,u-d} \equiv B_{20}^{u-d}(t = 0, m_\pi = 0)$, $C_{20}^{0,u-d} \equiv C_{20}^{u-d}(t = 0, m_\pi = 0)$, and we have included estimates of $\mathcal{O}(p^3)$ corrections in the form of $(\delta_B^{t,u-d} t)$, $(\delta_B^{m_\pi,u-d} m_\pi^2)$, $(\delta_C^{t,u-d} t)$, and $(\delta_C^{m_\pi,u-d} m_\pi^2)$. The associated low-energy constants are treated as free parameters and may be obtained from a fit to the lattice data. Because of the small prefactor, the term $\propto h_A(t, m_\pi)$ is of $\mathcal{O}(10^{-3})$ for $m_\pi \leq 700$ MeV, $|t| < 1$ GeV^2, and therefore numerically negligible. Also, $h_{B,C}(t, m_\pi)$ are very weakly dependent on t, so

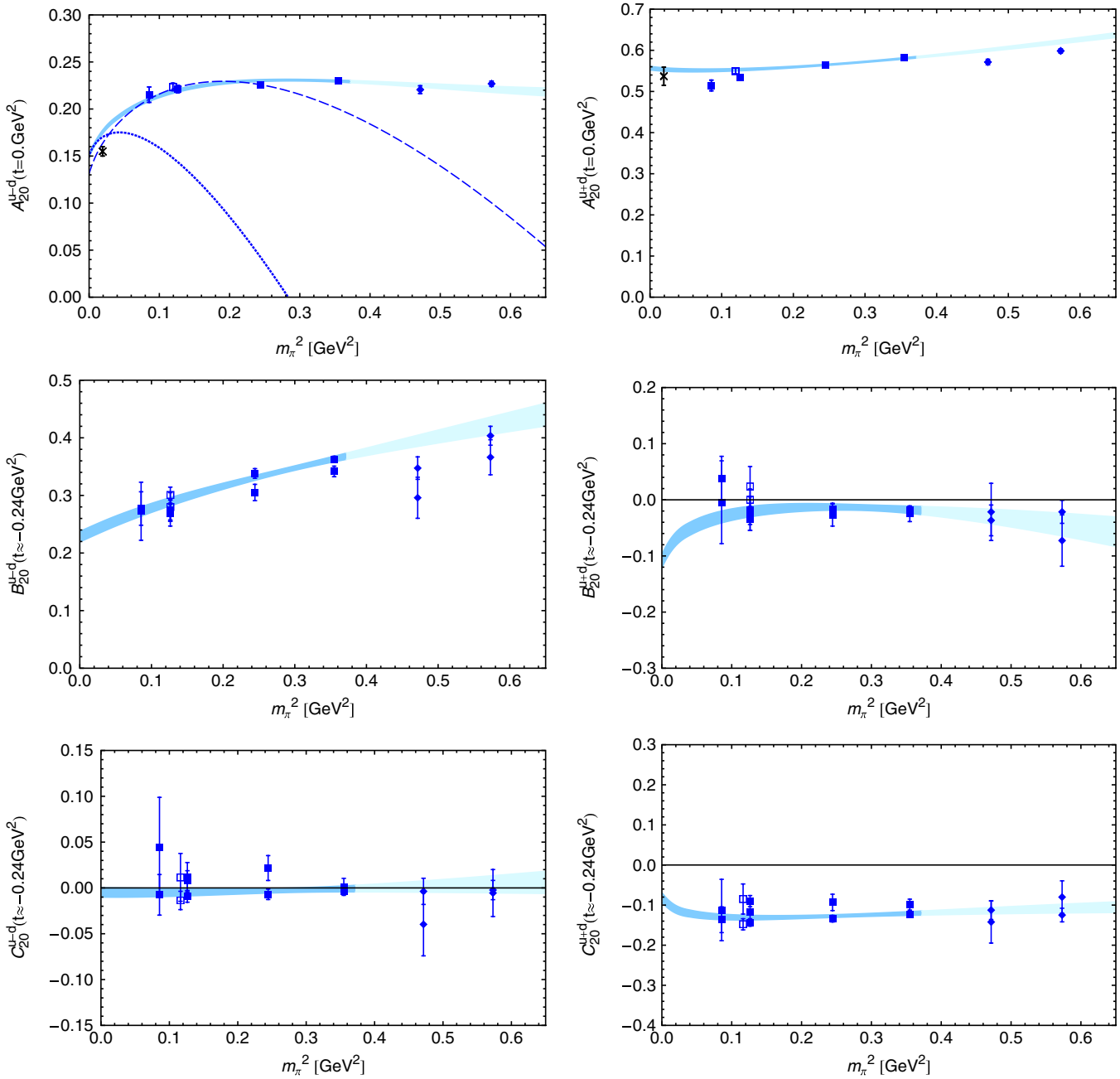

FIG. 36 (color online). Simultaneous BChPT fit to isovector (left) and isosinglet (right) lattice data for $m_\pi < 580$ MeV. The dotted line is the heavy-baryon limit of the BChPT fit. A HBChPT fit to the lattice data for $|t| < 0.3$ GeV^2 and $m_\pi < 500$ MeV is shown by the dashed line. The phenomenological value of $\langle x \rangle_{u\pm d}$ (CTEQ6) is indicated by the cross. Disconnected contributions are omitted in the isosinglet case. Notice that B_{20} and C_{20} are displayed for $t \approx -0.24$ GeV^2. At $m_\pi^2 \approx 0.12$ GeV^2, the larger volume (28^3) is the filled symbol, the smaller volume (20^3) the open symbol; for all other pion masses, the volume is 20^3. The χ^2/dof is 1.5 and 2.8, respectively, in the isovector and isosinglet cases.

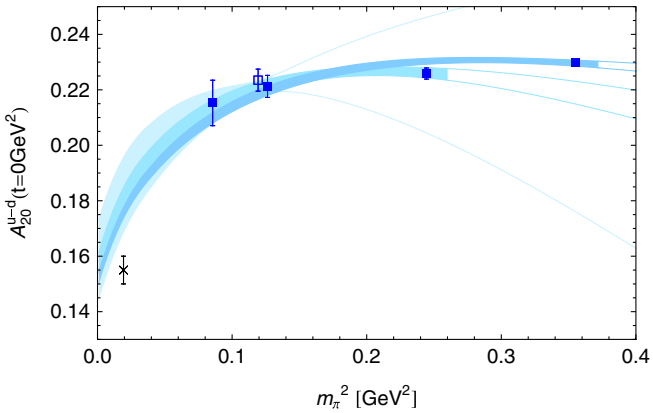

FIG. 37 (color online). A study of the stability of the BChPT extrapolation of A_{20}^{u-d} at $t = 0$ GeV^2 based on Eqs. (61)–(63). The three different error bands represent chiral fits to lattice results for pion masses in the regions $m_\pi < 400$, 500, and 600 MeV, respectively.

that the ansatz for each form factor is practically linear in t. The parameter m_N in the denominator of Eqs. (62) and (63) is the nucleon mass in the chiral limit and was set to 890 MeV, as given in Table VIII.

We use the value $\tilde{A}_{20}^{0,u-d} = 0.17$ obtained from a heavy-baryon chiral perturbation theory (HBChPT) fit to our $m_\pi < 500$ MeV lattice results for $\tilde{A}_{20}^{u-d}(t = 0) = \langle x \rangle_{\Delta u - \Delta d}$. This value is consistent with an earlier determination [96], which we used for a similar fit in [20]. The fit is displayed in Fig. 35.

Since the low-energy constant $A_{20}^{0,u-d}$ is a common parameter in the BChPT formulas for the GFFs A_{20}^{u-d}, B_{20}^{u-d}, and C_{20}^{u-d}, we performed a simultaneous fit based on Eqs. (61)–(63) with a total of 9 (1 common and 8 separate) fit parameters to over 83 lattice data points. The fit is displayed in the left panel of Fig. 36 and the results in the chiral limit and at the physical pion mass are listed below in Table XLIII. The $\chi^2/\mathrm{dof} = 1.5$ is good and gives us confidence that the fit works well. Among the most important results is $\langle x \rangle_{u-d} = 0.1758(20)$, to be compared with $\langle x \rangle_{u-d}^{\mathrm{CTEQ6}} = 0.155(5)$. Our result is thus 10% to 15% higher than the phenomenological value, a statistically significant difference. Compared to [20], it has increased from 0.157(10) by a little less than 2 standard deviations.

TABLE XLIII. Chirally extrapolated GFFs A_{20}, B_{20}, C_{20} using BChPT.

	$m_\pi = 0$	$m_\pi = m_\pi^{\mathrm{phys}}$
A_{20}^{u-d}	0.1496(18)	0.1758(20)
B_{20}^{u-d}	0.282(12)	0.293(12)
C_{20}^{u-d}	−0.0150(84)	−0.0157(86)
A_{20}^{u+d}	0.5567(45)	0.5534(43)
B_{20}^{u+d}	−0.126(16)	−0.077(16)
C_{20}^{u+d}	−0.277(15)	−0.255(13)

The main reason is that $A_{20}^{u-d}(t = 0)$ at our lightest pion mass is bending down less than predicted by the chiral expansion compared to the heavier pion data points.

We obtain $B_{20}^{u-d}(t = 0, m_\pi^{\mathrm{phys}}) = 0.293(12)$, a value compatible with our previous result 0.273(63) [20], but with a much reduced uncertainty. The quantity $C_{20}^{u-d}(t = 0, m_\pi^{\mathrm{phys}}) = -0.0157(86)$ still comes out much smaller than A_{20} and B_{20}, but there is now a hint that it is, in fact, negative.

To study the difference between HBChPT and BChPT, we take the heavy-baryon limit of BChPT while keeping the same values of the fit parameters, and obtained the dotted line in Fig. 36. This curve overlaps with the BChPT curve only for $m_\pi < m_\pi^{\mathrm{phys}}$ and drops off sharply for $m_\pi > m_\pi^{\mathrm{phys}}$, indicating the quantitative importance of the truncated terms when using the coefficients from the BChPT fit. The dashed curve in Fig. 36 shows the result of fitting our lattice data for $|t| < 0.3$ GeV^2 and $m_\pi < 500$ MeV directly with the HBChPT expression, and indicates that the latter describes the behavior of our lattice data over a significantly smaller range of pion masses than the BChPT expression.

As already mentioned above, one of the main achievements of this work is the substantial reduction of the statistical uncertainties of the data points at $m_\pi = 356$, 495, and 597 MeV compared to our previous work [20], and the inclusion of an additional ensemble at $m_\pi = 293$ MeV. This allows us, in particular, to lower the cut in m_π in the chiral fits from 700 MeV to 600 MeV. However, it is also important to note that a full BChPT analysis of A_{20}, B_{20}, and C_{20} consistently including all terms of $\mathcal{O}(p^3)$ is still not available. In view of this, it is interesting to perform a first check of the stability and

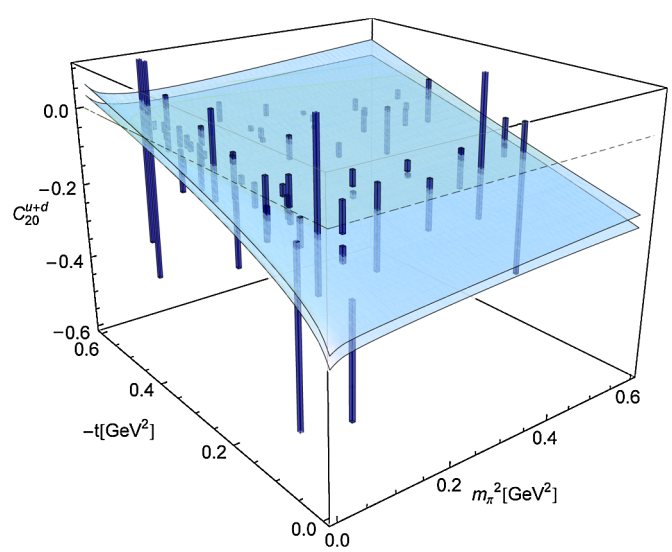

FIG. 38 (color online). The t and m_π^2 dependence of the isosinglet generalized form factor C_{20}. The two sheets indicate the statistical uncertainty of the BChPT fit.

potential uncertainty of the chiral extrapolations by repeating the fit for different maximal values of the included pion masses. Figure 37 shows a comparison of the BChPT extrapolations of A_{20}^{u-d} from fits to the lattice data in the regions $m_\pi < 400$, 500, and 600 MeV. Most importantly, we find that the error bands from all three extrapolations are consistent and do overlap in the region below $m_\pi^2 \sim 0.25\ \mathrm{MeV}^2$ down to the chiral limit. Apparently, the bending toward the physical point is not overly sensitive to the large pion-mass region, where $\mathcal{O}(p^3)$ corrections would have the strongest impact. A quantitative estimate of the uncertainties of the chiral extrapolation must therefore be based on an improved ChPT analysis (e.g. including higher-order effects) and higher precision lattice data at even lower pion masses, which is beyond the scope of the present work.

2. BChPT extrapolation of A_{20}^{u+d}, B_{20}^{u+d}, C_{20}^{u+d}

In this section we treat the GFFs in the isosinglet channel. The quantity $A_{20}^{u+d}(t=0) = \langle x\rangle_{u+d}$ is not only an important hadron structure observable on its own but, in addition, plays an important role for the computation of the total angular momentum contribution of quarks to the nucleon spin, $J^{u+d} = 1/2(A_{20}^{u+d}(0) + B_{20}^{u+d}(0))$, a discussion that we postpone to Sec. IV E. The combined (t, m_π) dependence in BChPT is given by [75]

$$A_{20}^{u+d}(t, m_\pi) = A_{20}^{0,u+d}\left(f_A^{u+d}(m_\pi) - \frac{g_A^2}{64\pi^2 f_\pi^2} h_A(t, m_\pi)\right) + A_{20}^{m_\pi,u+d} m_\pi^2 + A_{20}^{t,u+d} t + \Delta A_{20}^{u+d}(t, m_\pi) + \mathcal{O}(p^3), \tag{64}$$

$$B_{20}^{u+d}(t, m_\pi) = \frac{m_N(m_\pi)}{m_N} B_{20}^{0,u+d} + A_{20}^{0,u+d} h_B^{u+d}(t, m_\pi) + \Delta B_{20}^{u+d}(t, m_\pi) + \frac{m_N(m_\pi)}{m_N} \times \{\delta_B^{t,u+d} t + \delta_B^{m_\pi,u+d} m_\pi^2\} + \mathcal{O}(p^3), \tag{65}$$

$$C_{20}^{u+d}(t, m_\pi) = \frac{m_N(m_\pi)}{m_N} C_{20}^{0,u+d} + A_{20}^{0,u+d} h_C^{u+d}(t, m_\pi) + \Delta C_{20}^{u+d}(t, m_\pi) + \mathcal{O}(p^3), \tag{66}$$

where $A_{20}^{0,u+d} \equiv A_{20}^{u+d}(t=0, m_\pi = 0)$, and $f_A^{u+d}(m_\pi)$ and $h_A(t, m_\pi)$ contain the nonanalytic dependence on the pion mass and momentum transfer squared. Also, $B_{20}^{0,u+d} \equiv B_{20}^{u+d}(t=0, m_\pi = 0)$, and the terms ΔB_{20}, $\delta_B^{t,u+d} t$, and $\delta_B^{m_\pi,u+d} m_\pi^2$ are of $\mathcal{O}(p^3)$ and represent only a part of the full $\mathcal{O}(p^3)$ contribution. Similarly, $C_{20}^{0,u+d} \equiv C_{20}^{u+d}(t = 0, m_\pi = 0)$, and the term ΔC_{20}^{u+d}, proportional to the pion momentum fraction carried by quarks in the chiral limit $\langle x\rangle_{u+d}^{\pi,0}$, is a part of the full $\mathcal{O}(p^3)$ corrections [75]. As in the isovector case, the parameter m_N in the denominator of Eqs. (65) and (66) was set to 890 MeV.

The constants $A_{20}^{m_\pi,u+d}$, $A_{20}^{t,u+d}$, $B_{20}^{0,u+d}$, $\delta_B^{t,u+d}$, and $\delta_B^{m_\pi,u+d}$ may be obtained from a fit to the lattice data. In this counting scheme, contributions from operator insertions in the pion line, proportional to $\langle x\rangle_{u+d}^{\pi,0}$, are of order $\mathcal{O}(p^3)$. Counterterms of the form $\delta_C^{t,u+d} t$ and $\delta_C^{m_\pi,u+d} m_\pi^2$ first appear at $\mathcal{O}(p^4)$. Since in [20] the term $\Delta B_{20}^{u+d}(t, m_\pi)$ was found to lead to unstable fits, we perform a fit dropping this contribution but keeping the counterterms $\propto t$ and $\propto m_\pi^2$. We have also included the formally higher-order counterterms $\delta_C^{t,u+d} t$ and $\delta_C^{m_\pi,u+d} m_\pi$ in the fit to our lattice data. Furthermore, in order to see if such contributions could be relevant for the pion masses and values of the momentum transfer squared accessible in our calculation, we also include the estimate of the $\mathcal{O}(p^3)$ contribution ΔA_{20}^{u+d} provided in [75] in the fit to the lattice data points.

Similar to the isovector case discussed in the previous sections, the low-energy constant $A_{20}^{0,u+d}$ is a common parameter in the chiral extrapolation formulas for the isosinglet GFFs A_{20}^{u+d}, B_{20}^{u+d}, and C_{20}^{u+d}. Using $\langle x\rangle_{u+d}^{\pi,0} = 0.5$ as an input parameter [97–100], we performed a simultaneous fit to 83 lattice data points for these three GFFs, based on Eqs. (64) and (65), with 1 common and 8 separate low-energy constants as fit parameters. The results are also summarized in Table XLIII.

The result χ^2/dof for this fit is 2.8. The result in the chiral limit is $A_{20}^{0,u+d} = 0.5567(45)$, and $\langle x\rangle_{u+d} = A_{20}^{u+d}(t=0, m_\pi^{\mathrm{phys}}) = 0.5534(43)$ at the physical point. Incidentally, this value is in very good agreement with results of phenomenological parametrizations from the CTEQ [101] and MRST collaborations [102], $\langle x\rangle_{u+d}^{\mathrm{MRST2001}} = 0.538(22)$ and $\langle x\rangle_{u+d}^{\mathrm{CTEQ6}} = 0.537(22)$. A variation of the input parameter $\langle x\rangle_{u+d}^{\pi,0}$ by $\pm 10\%$ only leads to a small change in $A_{20}^{0,u+d}(t=0)$ of a few percent. The results of the fit are shown in Fig. 36. As already noted in [20], the slight upward bending in Fig. 36 at low m_π is due to the $\mathcal{O}(p^3)$ contribution ΔA_{20}^{u+d}. The fact that the lightest pion-mass data point does not exhibit this upward bending is partly responsible for the large value of the χ^2. Further calculations are required to see whether, for example, this point is pushed downward by finite-size effects. The inclusion of contributions from disconnected diagrams could also lead to a different m_π dependence.

In Fig. 38, the simultaneous dependence of C_{20}^{u+d} on t and m_π^2 is displayed. The error bars of the lattice data points are illustrated by the stretched cuboids. The two surfaces represent the BChPT fit discussed in this section with its uncertainty. The figure illustrates that C_{20}^{u+d} becomes relatively large near the origin, which implies that the ξ dependence of $H^{n=2}(\xi, t)$ and $E^{n=2}(\xi, t)$ is far from being negligible.

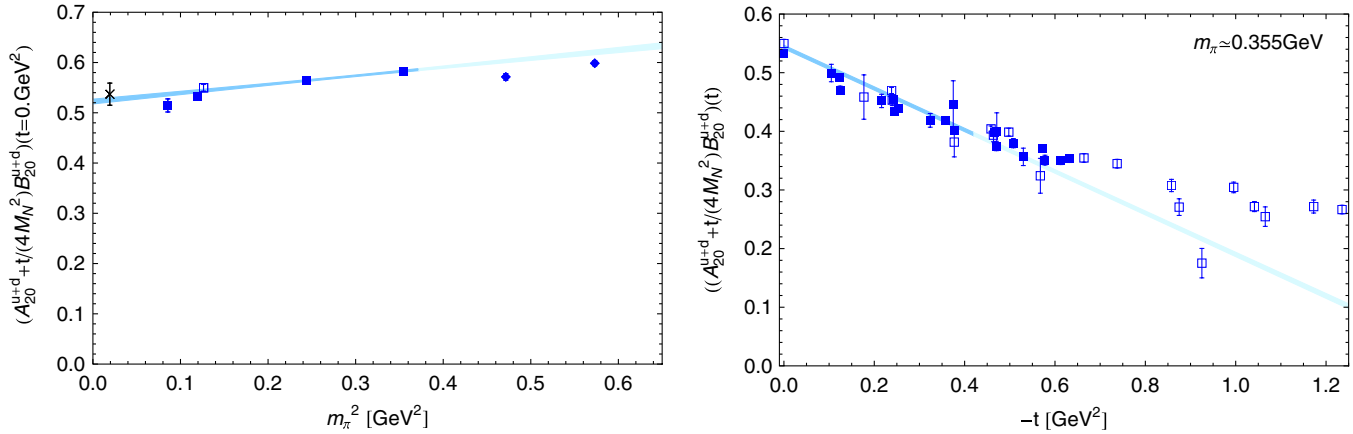

FIG. 39 (color online). Pion-mass and momentum transfer dependence of E_{20}. At $m_\pi = 356$ MeV, the open symbol corresponds to 20^3, the filled symbol to 28^3. At all other pion masses, the volume is 20^3. The extrapolation in m_π at $t = 0$ can be compared to the extrapolation of A_{20}^{u+d} in Fig. 36.

3. HBChPT extrapolation of E_{20}^{u+d} and M_{20}^{u+d}

In HBChPT [90,91] to $\mathcal{O}(p^2)$, the combined (t, m_π) dependence of the GFF combination $E_{20}^{u+d}(t) = A_{20}^{u+d}(t) + t/(4m_N^2)B_{20}^{u+d}(t)$ is quite different from that of $M_{20}^{u+d}(t) = A_{20}^{u+d}(t) + B_{20}^{u+d}(t)$, which in the forward limit is equal to 2 times the total quark contribution to the nucleon spin, $2J_q = M_{20}^{u+d}(t = 0)$. The notation is chosen by analogy with the Sachs form factors in the $n = 1$ sector, E being the analog of G_E and M of G_M. Our results for B_{20}^{u+d} are in units of the quark-mass dependent nucleon mass; to be consistent with the conventions of the chiral expansion Eq. (68) below, we multiply the B_{20}^{u+d} data by $m_N^{\mathrm{phys}}/m_N(m_\pi)$ before performing the fit. In [20], this conversion had been omitted.

While at this order M_{20}^{u+d} shows a nonanalytic dependence on t and m_π as discussed below, E_{20}^{u+d} is constant up to analytic tree-level contributions,

$$E_{20}^{u+d}(t, m_\pi) = E_{20}^{0,u+d} + E_{20}^{m_\pi,u+d} m_\pi^2 + E_{20}^{t,u+d} t. \qquad (67)$$

A fit to our lattice results based on Eq. (67) is shown in Fig. 39. The linear dependence of E_{20} on t and m_π^2 works well within the fit range, while the higher mass points do not quite lie on a common smooth curve. In contrast to the covariant approach, the functional form of $E_{20}(t = 0) = A_{20}(t = 0)$ does not exhibit a term that could lead to an upward bending as seen on the right panel of Fig. 36.

The pion-mass dependence of $M_{20}^{u+d}(t)$ for nonzero t is given by [90,91]

$$M_{20}^{u+d}(t, m_\pi) = M_{20}^{0,u+d}\left\{1 - \frac{3g_A^2 m_\pi^2}{(4\pi f_\pi)^2} \ln\left(\frac{m_\pi^2}{\Lambda_\chi^2}\right)\right\} + M_2^{(2,\pi)}(t, m_\pi) + M_{20}^{m_\pi,u+d} m_\pi^2 + M_{20}^{t,u+d} t, \qquad (68)$$

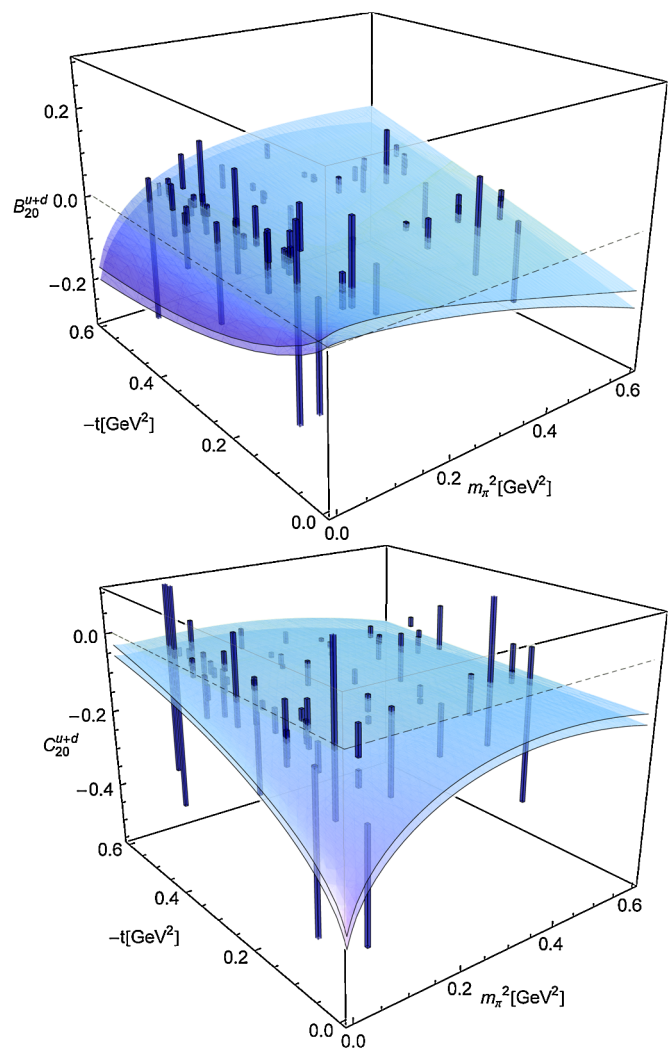

FIG. 40 (color online). The t and m_π^2 dependence of the isosinglet generalized form factors $\frac{m_N^{\mathrm{phys}}}{m_N(m_\pi)} B_{20}$ and $\frac{m_N^{\mathrm{phys}}}{m_N(m_\pi)} C_{20}$, and a HBChPT fit. Its uncertainty is indicated by the two surfaces.

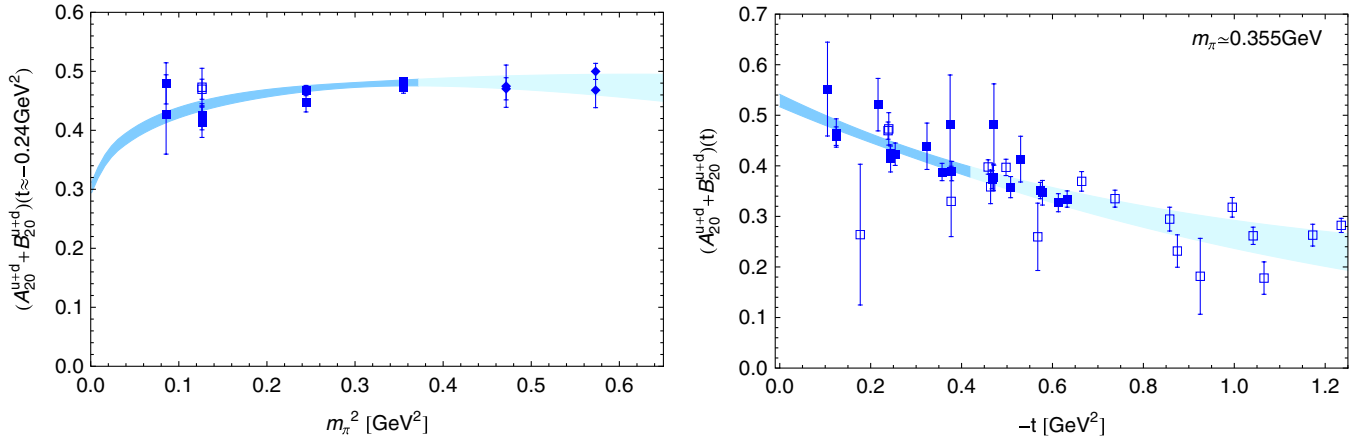

FIG. 41 (color online). Pion and momentum transfer dependence of M_{20}. At $m_\pi = 356$ MeV, the open symbol corresponds to 20^3, the filled symbol to 28^3. At all other pion masses, the volume is 20^3.

with new counterterms $M_{20}^{m_\pi,u+d}$ and $M_{20}^{t,u+d}$. The nonanalytic dependence on t and m_π in $M_2^{(2,\pi)}(t, m_\pi)$ results from pion-operator insertions and is directly proportional to the (isosinglet) momentum fraction of quarks in the pion in the chiral limit, $\langle x\rangle_{u+d}^{\pi,0}$. We use $\langle x\rangle_{u+d}^{\pi,0} = 0.5$ for the fit. The results of chiral fits based on Eq. (68) are presented in Fig. 41. We note that the data for $M_{20}(t = -0.24\ \text{GeV}^2, m_\pi)$ has a tendency of bending downward as a function of m_π, and the fit is able to describe this behavior. We find $M_{20}^{u+d}(t = 0, m_\pi^{\text{phys}}) = 0.528(11)$. We will use this result in Sec. IV E.

4. HBChPT extrapolation of B_{20}^{u+d}

Since the total anomalous gravitomagnetic moment of quarks and gluons in the nucleon has to vanish, $\sum_{q,g} B_{20}(t = 0) = 0$, an interesting question is whether the individual quark and gluon contributions to B_{20} are separately zero or very small. The GFF B_{20}^{u+d} can be written as a linear combination of Eqs. (67) and (68). A separate fit to the data with fixed $E_{20}^{0,u+d} = 0.522$ gives $B_{20}^{u+d}(t = 0, m_\pi^{\text{phys}}) = 0.015(11)$ which is compatible with the fits to M_{20}^{u+d} and E_{20}^{u+d} above that in combination give $(M - E)_{20}^{u+d}(t = 0, m_\pi^{\text{phys}}) = 0.003(12)$. Although the absolute value of $B_{20}^{u+d}(t = 0)$ is again rather small, we note that the sign is different from that found in Sec. IV D 2 based on the BChPT fit, where it was negative. A more accurate calculation and the full $\mathcal{O}(p^3)$ BChPT expression will help resolve the sign of $B_{20}^{u+d}(t = 0)$. The simultaneous dependence of B_{20}^{u+d} on m_π and t is shown in Fig. 40. We recall that the sum of B_{20}^{u+d} and the corresponding quantity for gluons vanishes in the forward direction. The very nontrivial interplay of the t and m_π dependence results in a small value of B_{20}^{u+d} near the origin of the (t, m_π) plane, suggesting also a small value of $B_{20}^{g}(t = 0)$ in the real world. However, near the chiral limit the form factor B_{20}^{u+d} becomes sizable, about -0.1 at $-t \approx 0.24\ \text{GeV}^2$.

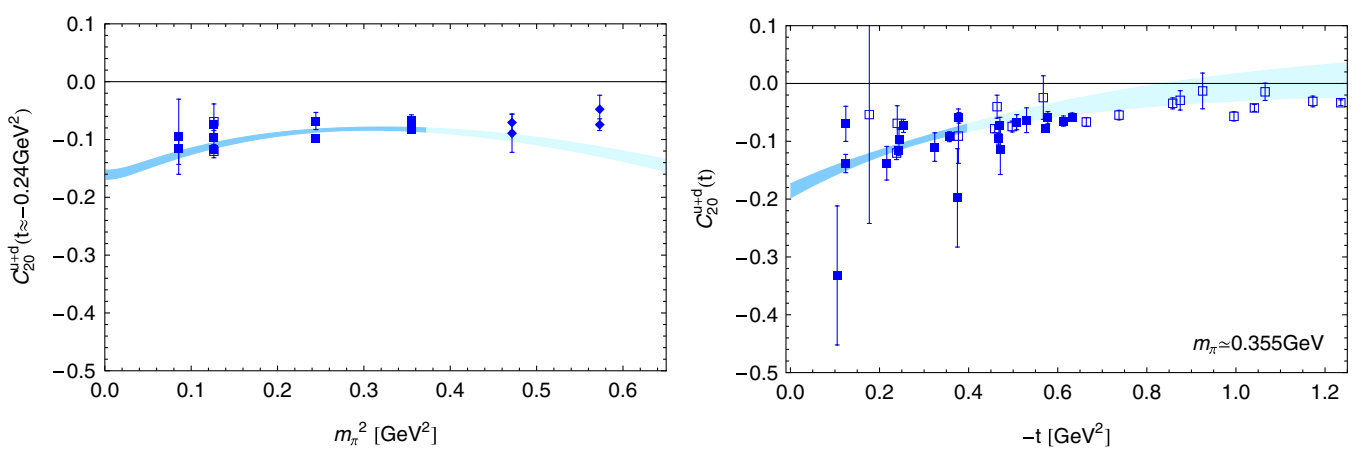

FIG. 42 (color online). Projections of C_{20}^{u+d}—as depicted in Fig. 40—on a constant $-t$ plane and on a constant m_π^2 plane. The HBChPT fit appears as a shaded band.

5. HBChPT extrapolation of C_{20}^{u+d}

At order $\mathcal{O}(p^2)$, the pion-mass dependence of the GFF $C_{20}^{u+d}(t)$ is given by [89–91]

$$C_{20}^{u+d}(t, m_\pi) = \frac{1}{1 - t/(4m_N^2)}\{C_{20}^{0,u+d} + E_2^{(1,\pi)}(t, m_\pi) + E_2^{(2,\pi)}(t, m_\pi) + C^{m_\pi,u+d} m_\pi^2 + C^{t,u+d} t\}, \tag{69}$$

where $C_{20}^{0,u+d} \equiv C_{20}^{u+d}(t = 0, m_\pi = 0)$. The terms $E_2^{(1,\pi)}(t, m_\pi)$ and $E_2^{(2,\pi)}(t, m_\pi)$ contain nonanalytic terms in t and m_π that come from insertions of pion operators proportional to $\langle x\rangle_{u+d}^{\pi,0}$. Additionally, $E_2^{(2,\pi)}(t, m_\pi)$ depends on the low-energy constants c_1, c_2, and c_3, which are set to the same values as in [20]. To be consistent with the chiral expansion Eq. (69), we rescale the C_{20}^{u+d} lattice data by $m_N^{\rm phys}/m_N(m_\pi)$ before performing the fit. We find a value of $C_{20}^{0,u+d} = -0.407(14)$ in the chiral limit, and $C_{20}^{u+d}(t = 0, m_\pi^{\rm phys}) = -0.325(14)$ at the physical pion mass. The simultaneous dependence of C_{20}^{u+d} on m_π and t is shown in Fig. 40, along with the HBChPT fit. Comparing the figure with Fig. 38, one sees that the fits differ significantly at larger values of m_π and $-t$. The result is also shown as a function of the pion mass squared for fixed $t \approx -0.24$ GeV^2 in Fig. 42 (left panel), and the t dependence at a pion mass of 356 MeV is presented in the right panel.

E. Quark contributions to the proton spin

In the following, we will present and discuss our results for the quark spin and orbital angular momentum contributions (OAM) to the proton spin. We first remind the reader that the form factors of the energy-momentum tensor, which in this section we denote by $A^{q,g}(t) \equiv A_{20}^{q,g}(t)$ and $B^{q,g}(t) \equiv B_{20}^{q,g}(t)$, in the forward limit $t = 0$ give direct access to the quark and gluon angular momenta in Ji's nucleon spin sum rule,

$$\frac{1}{2} = \sum_{q=u,d,\ldots} J^q + J^g = \frac{1}{2}\left\{\sum_{q=u,d,\ldots}(A^q(0) + B^q(0)) + (A^g(0) + B^g(0))\right\}. \tag{70}$$

Furthermore, the quark angular momentum may be decomposed in terms of the quark spin, $\Delta\Sigma^q$, and orbital angular momentum, L^q, such that

$$\frac{1}{2} = \sum_{q=u,d,\ldots}\left(\frac{1}{2}\Delta\Sigma^q + L^q\right) + J^g. \tag{71}$$

It is important to note that the decompositions in Eqs. (70) and (71) are fully gauge invariant, and that the individual terms will in general be renormalization scale and scheme dependent. Since the momentum fractions carried by quarks and gluons have to add up to one, i.e. the total nucleon momentum,

$$1 = \sum_{q=u,d,\ldots} A^q(0) + A^g(0) = \sum_{q=u,d,\ldots}\langle x\rangle^q + \langle x\rangle^g, \tag{72}$$

one also finds that the anomalous gravitomagnetic moments, $B^{q,g}(0)$, have to cancel exactly in sum,

$$0 = \sum_{q=u,d,\ldots} B^q(0) + B^g(0). \tag{73}$$

It is a prominent goal of future lattice hadron structure calculations to study the above sum rules in great detail. Since gluonic observables suffer in general from very low signal-to-noise ratios and have so far not been studied on the lattice with sufficient precision, for the moment we will have to concentrate on the (connected) contributions from up and down quarks.

In Sec. IV E 1 below, we will begin with a discussion of J^q based on our results for the GFFs $A_{20}^{u,d}(t)$ and $B_{20}^{u,d}(t)$. There, the results of the covariant and heavy-baryon chiral extrapolations of Secs. IV D 1–IV D 3 will be supplemented and compared with an extrapolation of J^{u+d} using a ChPT formalism that includes explicitly the Δ resonance as an additional degree of freedom. A decomposition of J^q in quark spin and OAM contributions, together with corresponding chiral extrapolations, will be presented in Sec. IV E 2.

1. Quark angular momentum J

From the covariant BChPT extrapolation in Sec. IV D 2 of the isosinglet GFFs $A_{20}(t)$ and $B_{20}(t)$, we find a value of $J_{\rm BChPT}^{u+d} = 0.238(8)$ for the total quark angular momentum contribution at the physical pion mass. This corresponds to $\simeq 48\%$ of the total nucleon spin $S = 1/2$, which is somewhat larger than our result in [20], although the difference is clearly not significant within statistical errors. We note again that these values have to be considered with some caution, since contributions from disconnected diagrams have not been included.

A result that is more accurate regarding the systematics can be given for the isovector, $u - d$, channel where disconnected diagrams cancel out exactly. From the chiral extrapolations in Sec. IV D 1, we obtain $J_{\rm BChPT}^{u-d} = 0.234(6)$ at $m_\pi^{\rm phys}$. That this value is so close to the $u + d$-quark angular momentum already points to a small contribution from down quarks. Indeed, combining the isovector and isosinglet results, we find that the up quarks carry a substantial amount of angular momentum, $J_{\rm BChPT}^{u} = 0.236(6)$, while the contribution from down quarks is very small and even negligible within the small statistical errors, $J_{\rm BChPT}^{d} = 0.0018(37)$. We will see in Sec. IV E 2 below that the smallness of J^d can be traced back to a remarkably precise cancellation between spin and orbital angular momentum of quarks. The results we have just discussed are illustrated in Fig. 43, showing $J^{u,d}$ as a function of m_π^2, together with

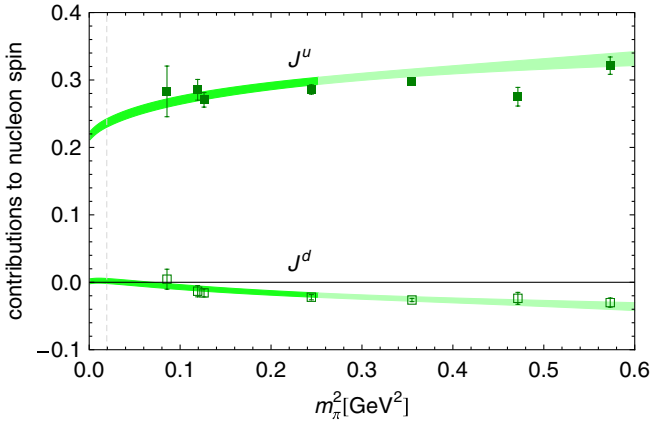

FIG. 43 (color online). Chiral extrapolations of $J^{u,d}$ using BChPT. Note that the displayed lattice data points were not directly employed in the chiral fits. Details are given in the text.

the corresponding BChPT extrapolations indicated by the error bands. We note that the lattice data points were obtained from separate dipole extrapolations of the GFFs $B_{20}^{u,d}(t)$ to $t = 0$.

In order to study possible systematic uncertainties in the chiral extrapolation of quark orbital angular momentum just described, we now briefly discuss a completely different approach to the chiral extrapolation of J^{u+d}. This will be based on HBChPT including the Δ resonance as an explicit degree of freedom, predicting at leading-one-loop order a pion-mass dependence of J^{u+d} of the form [103]

$$\begin{aligned} J^{u+d}_{\mathrm{HBChPT}+\Delta}(m_\pi) = J^{u+d}_{\mathrm{HBChPT}}(m_\pi) - \frac{1}{2}\Bigg(\frac{9}{2}(A+B)^{0,u+d}_{20} \\ + 3\langle x\rangle^{\pi,0}_{u+d} - \frac{15}{2}b_{q\Delta}\Bigg)\frac{8g^2_{\pi N\Delta}}{9(4\pi f_\pi)^2} \\ \times\Bigg\{(m_\pi^2 - 2\Delta^2)\ln\left(\frac{m_\pi^2}{\Lambda_\chi^2}\right) \\ + 2\Delta\sqrt{\Delta^2 - m_\pi^2}\ln\left(\frac{\Delta - \sqrt{\Delta^2 - m_\pi^2}}{\Delta + \sqrt{\Delta^2 - m_\pi^2}}\right)\Bigg\}, \end{aligned} \tag{74}$$

where $\Delta = m_\Delta - m_N$ denotes the Δ-nucleon mass difference, and $g_{\pi N\Delta}$ is the pion-nucleon-Δ coupling. The m_π-dependent $J^{u+d}_{\mathrm{HBChPT}}$ in Eq. (74) corresponds to the HBChPT result without explicit Δ intermediate states as obtained from Eq. (66) for $t = 0$ and is given by[3]

$$\begin{aligned} J^{u+d}_{\mathrm{HBChPT}}(m_\pi) = \frac{1}{2}\Bigg\{(A+B)^{0,u+d}_{20} + 3(\langle x\rangle^{\pi,0}_{u+d} \\ - (A+B)^{0,u+d}_{20})\frac{g_A^2 m_\pi^2}{(4\pi f_\pi)^2}\ln\left(\frac{m_\pi^2}{\Lambda_\chi^2}\right)\Bigg\} \\ + J^{m_\pi,u+d}m_\pi^2. \end{aligned} \tag{75}$$

[3]In the notation of [103], $b_{qN} = (A+B)^{0,u+d}_{20} = M^{0,u+d}$.

Since the GFF $B_{20}(t)$ cannot be extracted directly at $t = 0$, we have first performed separate dipole extrapolations of $B^u_{20}(t)$ and $B^d_{20}(t)$ to $t = 0$, and combined this with our values for $\langle x\rangle^{u+d} = A^{u+d}_{20}(0)$ to obtain $J^{u+d} = (A^{u+d}_{20}(0) + B^{u+d}_{20}(0))/2$. The resulting lattice data points, including the full jackknife errors from the extrapolations of the $B_{20}(t)$ to the forward limit, are displayed in Fig. 44. Chiral fits based on Eq. (74), with the three free parameters $b_{qN} \equiv (A + B)^{0,u+d}_{20}$, $b_{q\Delta}$, and $J^{m_\pi,u+d}$, to the data with $m_\pi \leq 600$ MeV and $m_\pi \leq 700$ MeV are represented by the shaded error band and the curves (representing the upper and lower bounds of an error band), respectively. In both cases, we have fixed $\Delta = 0.3$ GeV and used the large-N_c relation $g_{\pi N\Delta} = 3/(2^{3/2})g_A$ as given in Table VIII.

The fit to our lattice results with $m_\pi \leq 600$ MeV gives $(A + B)^{0,u+d}_{20} = b_{qN} = 0.514(41)$, $b_{q\Delta} = 0.486(55)$, and $J^{u+d}_{\mathrm{HBChPT}+\Delta}(m_\pi^{\mathrm{phys}}) = 0.245(30)$ at the physical pion mass. Including the data point at $m_\pi = 687$ MeV in the fit, we find consistent values with somewhat smaller errors, $(A + B)^{0,u+d}_{20} = b_{qN} = 0.546(24)$, $b_{q\Delta} = 0.449(39)$, and $J^{u+d}_{\mathrm{HBChPT}+\Delta}(m_\pi^{\mathrm{phys}}) = 0.226(22)$. It is encouraging to see that these values fully agree within statistical errors with the results from the global simultaneous BChPT extrapolations of the GFFs $A_{20}(t)$, $B_{20}(t)$, and $C_{20}(t)$ discussed above.

2. Quark spin and orbital angular momentum contributions

For a consistent decomposition of the quark angular momentum, J^q, into quark spin, $\Delta\Sigma^q$, and orbital angular momentum, L^q, contributions, we need in addition lattice results for $\tilde{A}^{u+d}_{10}(t=0) = \Delta\Sigma^{u+d}$ and $\tilde{A}^{u-d}_{10}(t=0) = \Delta\Sigma^{u-d}$.

Our lattice data for $\Delta\Sigma^{u+d}/2$ is displayed in Fig. 45, together with a 2-parameter HBChPT fit represented by the upper shaded error band. The chiral extrapolation leads to a value of $\tilde{A}^{u+d}_{10}/2(t = 0) = \Delta\Sigma^{u+d}/2 = 0.208(10)$ at the

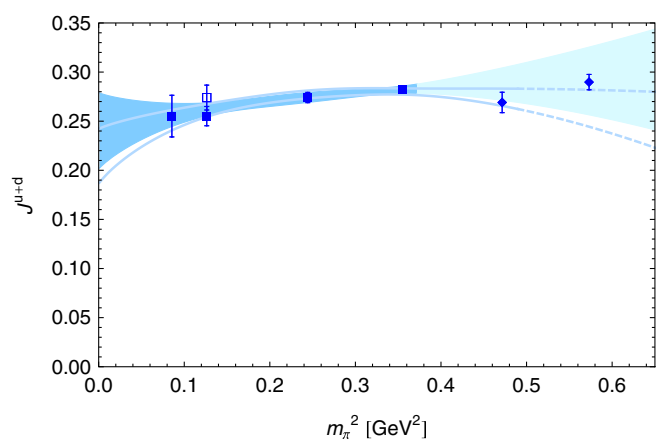

FIG. 44 (color online). Chiral extrapolation of J^{u+d} using HBChPT including the Δ resonance, Eq. (74). The fit and error bands are explained in the text.

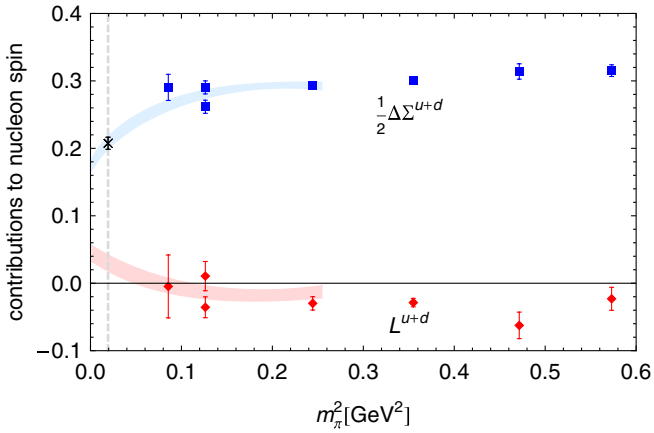

FIG. 45 (color online). Total quark spin and orbital angular momentum contributions to the spin of the proton. The cross represents the value from the HERMES 2007 measurement [49]. The error bands are explained in the text. Disconnected contributions are not included.

physical pion mass, perfectly matching the recent results from HERMES [49] indicated by the cross. However, since this is a leading 1-loop HBChPT fit at comparatively large pion masses, the agreement with the experimental value should be considered with great caution and seen as indicative. Combining this with the results from the previous section for J^{u+d} and the corresponding BChPT extrapolation, we find a remarkably small quark orbital angular momentum $L^{u+d} = J^{u+d} - \Delta\Sigma^{u+d}/2$ contribution to the nucleon spin for a wide range of pion masses, as indicated by the filled diamonds and the lower error band in Fig. 45. From the combined covariant and heavy-baryon chiral extrapolations, we obtain a value of $L^{u+d} = 0.030(12)$ at the physical pion mass.

Superficially seen, such a small OAM contribution from $u + d$ quarks of only $\approx 6\%$ to the nucleon spin is in clear conflict with general expectations from relativistic quark models, which suggest that $L^{u+d} = 30\%$–40% of $1/2$. Moreover, from quite general arguments, e.g. based on light-cone wave-function representations of hadrons, substantial quark orbital motion is essential for the Pauli form factor F_2 to be nonvanishing in general, and also for the formation of azimuthal single spin asymmetries in semi-inclusive deep inelastic scattering related to, e.g., the Sivers effect [104–106]. As we will see in the following, these apparent inconsistencies may be explained by studying, on the one hand, the renormalization scale dependence of quark OAM, and, on the other, the contributions from individual quark flavors.

We begin with the latter by noting that a study of the separate up- and down-quark OAM contributions requires in addition knowledge of the spin and angular momentum in the isovector, $u - d$, channel. To this end, we identify the $u - d$ quark spin contribution with the axial-vector coupling constant, $g_A = \tilde{A}_{10}^{u-d}(t = 0) = \Delta\Sigma^{u-d}$, which we have discussed above in Sec. IV A; cf. Figure 9. Using our lattice data for g_A, $\Delta\Sigma^{u+d}$, and $(A + B)_{20}^{u\pm d}$, we have computed the individual spin and OAM contributions from up and down quarks to the nucleon spin, which are displayed in Fig. 46 as functions of m_π^2. We stress that the chiral extrapolations represented by the shaded error bands in Fig. 46 were not obtained from direct fits to the shown lattice data points, but are the result of combining the superjackknife error bands of the heavy-baryon, SSE, and covariant baryon chiral extrapolations in Figs. 45, 9, and 36. The very good overlap of the bands with the data points may be seen as a first consistency check of our approach, in particular, with respect to the different types of extrapolations in the squared momentum transfer and the pion mass that we have employed throughout this work.

Most remarkably, Fig. 46 shows that the individual up- and down-quark OAM contributions are sizable and of similar magnitude over a wide range of pion masses, but opposite in sign, and therefore only cancel to a large extent in the sum, $L^{u+d} \approx 0$, as already observed in Fig. 45. At the physical pion mass, we find from the chiral extrapolations that $|L^u| \approx |L^d| \approx 33\%$ of $1/2$. A more accurate result can be given for the isovector channel where disconnected contributions cancel out, $L^{u-d} = -0.379(71)$.

These observations may be seen in analogy to a corresponding analysis of the nucleon anomalous magnetic moment, $\kappa = F_2(0) = B_{10}(0)$: Although the proton and neutron anomalous magnetic moments are sizable (and, as noted in [104,107], related to nonzero quark orbital motion), $\kappa^p = 1.79$ and $\kappa^n = -1.91$, they largely cancel in the sum, $\kappa^{u+d} = 3\kappa^{p+n} = -0.36$; see also Sec. IV B 6. However, as for L^{u+d}, this does not imply that the orbital motion of individual quarks in the nucleon is necessarily small.

Furthermore, from a direct comparison of Figs. 43 and 46, we find that the smallness of the angular momentum of

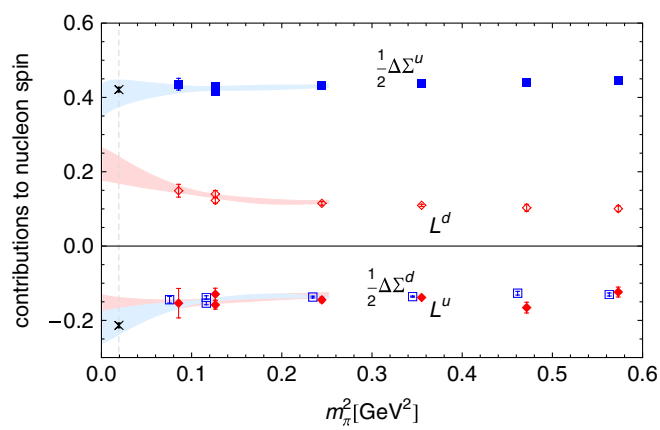

FIG. 46 (color online). Quark spin and orbital angular momentum contributions to the spin of the proton for up and down quarks. Filled and open squares denote $\Delta\Sigma^u/2$ and $\Delta\Sigma^d/2$, and filled and open diamonds denote L^u and L^d, respectively. The crosses represent the values from the HERMES 2007 measurement [49]. The error bands are explained in the text. Disconnected contributions are not included.

down quarks can be seen as the result of another remarkable cancellation, in this case between spin and OAM. While both types of contributions for the down quarks are similarly large in magnitude, $|\Delta\Sigma^d|/2 \approx |L^d| \approx$ 20%–30% of 1/2, they are again of opposite sign and hence cancel out in the sum, $J^d = \Delta\Sigma^d/2 + L^d \approx 0$.

Even though the small value for L^{u+d} in our lattice calculation can be understood to arise from a cancellation between the different quark flavors, it would still be important to understand the striking discrepancy with results from relativistic quark-model calculations, $L^{u+d} \approx$ 30%–40%, as noted above. In principle, this could be related to a severe deficiency of the model, or unexpectedly large, systematic uncertainties in the lattice calculation. A more likely solution has been proposed in [108,109], just by noting that quark-model calculations generically correspond to a low, hadronic scale $\mu \ll 1$ GeV, while the resolution scale chosen here is $\mu^2_{\overline{\rm MS}} = 4$ GeV^2. Since quark OAM is not conserved under (leading and higher-order) evolution [110], it is therefore in general pointless to directly compare the lattice results with the model expectations at the different scales. For a more sensible comparison, one might instead try to evolve the model results up to the lattice scale—or, alternatively, transform the lattice values down to the hadronic scale. In order to show that the different scales might be in principle responsible for the observed discrepancy, we follow Refs. [41,109] and consider the LO scale dependence of L^{u-d}, given by [110]

$$L^{u-d}(t) = \left(\frac{t}{t_0}\right)^{(2/\beta_0)(-16/9)}\left\{L^{u-d}(t_0) + \frac{1}{2}\Delta\Sigma^{u-d}\right\} - \frac{1}{2}\Delta\Sigma^{u-d}, \tag{76}$$

where $t_{(0)} = \ln(\mu^2_{(0)}/\Lambda^2_{\rm QCD})$ with an initial scale denoted by μ_0, and where the isovector spin contribution, $\Delta\Sigma^{u-d}/2 = g_A/2$, is exactly conserved under QCD evolution. Working in the isovector channel allows us to avoid issues related to disconnected diagrams (that were not included in our lattice calculation), and, in particular, the mixing with gluon operators under evolution. Figure 47 shows the result of the LO evolution according to Eq. (76) from an initial scale of $\mu_0 = 2$ GeV, with lattice starting values $L^{u-d} = -0.38$ and $\Delta\Sigma^{u-d}/2 = 0.61$, down to very low (model) scales, as indicated by the left pointing arrow.

Although the application of LO evolution equations at such low scales cannot be quantitatively trusted, we note at least that qualitatively a strong scale dependence sets in as $\mu \to \Lambda_{\rm QCD}$, eventually leading to a change of sign of L^{u-d}. We note that similar observations have been made in the isosinglet channel [109], even allowing for an approximate quantitative agreement of the lattice value for L^{u+d} with the expectations from relativistic quark models. One should keep in mind, however, that the renormalization scheme (e.g. $\overline{\rm MS}$) of a model is in general indeterminate, which is a fundamental limitation in the comparison with

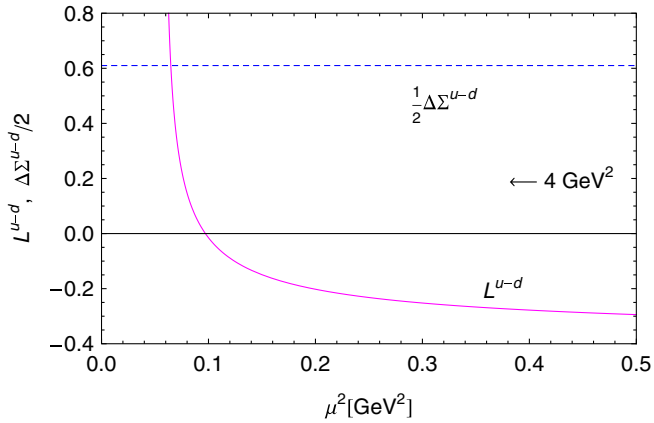

FIG. 47 (color online). Leading order evolution of lattice results for L^{u-d} (solid line) and $\Delta\Sigma^{u-d}$ (dashed line) from $\mu_0^2 =$ 4 GeV^2 down to low hadronic scales.

results from the full theory. To sum up, the above exercise shows very clearly that a one-to-one confrontation of hadron structure observables from the lattice and in models must be considered with great caution.

For convenience, we present in Table XLIV an overview of our results for the (connected) quark contributions to the proton spin, in the $\overline{\rm MS}$ scheme at $\mu^2 = 4$ GeV^2, at the physical pion mass, as obtained from the different chiral extrapolations discussed in this section and the previous sections. We also include estimates of systematic uncertainties due to the renormalization of the 1-derivative operators, as discussed in Sec. III D. At this point we note again that no phenomenological values for $\Delta\Sigma = \langle 1\rangle_{\Delta q}$, $\langle x\rangle_q$, and $\langle x\rangle_{\Delta q}$ have been used in the chiral fits, and that we have so far only included contributions from connected diagrams in the lattice calculations.

As a final note, we look forward to different angles of attack from the experimental and phenomenological sides becoming available. These will supplement the currently available deeply virtual Compton scattering measurements at JLab and HERMES and help to narrow down the statistical and systematic uncertainties [111,112]. Stronger constraints might come from experimental data on, e.g., the transverse target-spin asymmetry $A_{\rm UT}$ for the electroproduction of vector mesons, which is, in particular, sensitive to the GPD E. In this respect, it is interesting to note that the (model-dependent) phenomenological analysis in [113], which is compatible with recent data from HERMES [114] and preliminary results from COMPASS [115] on $A_{\rm UT}$, has found a similar pattern of valence quark (orbital) angular momentum contributions as compared to our result in Table XLIV.

V. SUMMARY AND CONCLUSIONS

We have performed a comprehensive lattice QCD study of the observables characterizing the structure of the nucleon. The moments of forward parton distributions,

TABLE XLIV. Overview of proton spin observables at $m_\pi^{\rm phys}$ from chiral extrapolations of the lattice results, in the $\overline{\rm MS}$ scheme at a scale of $\mu^2 = 4$ GeV^2. Statistical and estimated systematic uncertainties due to the renormalization of the 1-derivative operators are given in brackets in the form $(\cdots)_{\rm stat}(\cdots)_{\rm ren}$; cf. Sec. III D. For the other observables we quote only the statistical uncertainty. We refer to Fig. 38 and the adjacent discussion for a study of potential uncertainties due to the chiral extrapolations. The experimental numbers for $\Delta\Sigma$ are from [49] for a scale of $\mu^2 = 5$ GeV^2. Details are given in the text.

	J^{u-d}	J^{u+d}	J^u	J^d	$g_A = \Delta\Sigma^{u-d}$	$\Delta\Sigma^{u+d}/2$	$\Delta\Sigma^u/2$	$\Delta\Sigma^d/2$	L^{u-d}	L^{u+d}	L^u	L^d
BChPT	0.234(6)(16)	0.238(8)(17)	0.236(6)(17)	0.0018(37)(1)								
HBChPT		0.264(6)(18)				0.208(10)				0.056(11)(18)		
HBChPT + Δ		0.226(22)(16)			1.21(17)							
mixed ChPT							0.411(36)	−0.203(35)	−0.379(71)(16)	0.030(12)(17)	−0.175(36)(17)	0.205(35)(0)
experiment					1.2670(35)	0.208(9)	0.421(6)	−0.214(6)				

the electromagnetic and axial form factors, and a set of generalized form factors, for both the isovector and the isoscalar flavor combinations, were calculated. We have applied various kinds of chiral expansion schemes to the data and compared our results to experimental values. Determining a wide set of nucleon properties simultaneously allows us to assess the range of applicability of these schemes, and allows us to gauge how sensitive the nucleon properties are to changes in the up- and down-quark masses.

The picture that emerges is that a nucleon composed of quarks corresponding to pion masses in the range $290\ \mathrm{MeV} < m_\pi < 760\ \mathrm{MeV}$ is significantly more compact than the nucleon in nature, when probed by a local vector current, as realized experimentally through photon-nucleon interaction. Both the Dirac and Pauli radii are less than a factor of $2/3$ of their physical values; cf. Figures 10 and 14. A similar observation holds for the axial radius (see Table XXXIV)—consequently, a nucleon composed of heavier up and down quarks would also appear much smaller than the physical nucleon if probed by a W boson. When performing fits to our data using the small-scale expansion (SSE) and covariant baryon chiral perturbation theory (BChPT) schemes, we find that the pion-mass dependence of our data is weaker than what we expect from those chiral expansions. Still, our findings are qualitatively compatible with the picture of a nucleon growing substantially in size when approaching the chiral limit. We also find that the Dirac form factor, at $m_\pi = 356$ MeV and for $0.3 < Q^2/\mathrm{GeV}^2 < 0.7$, exhibits a statistically significant finite-size effect in the femto-universe in which we study the nucleon; see Fig. 8. The latter appears to be "squeezed" when observed on the hypertorus of size $(2.5\ \mathrm{fm})^3$. For this reason the chiral schemes might well be applicable to the pion-mass regime which we probe if we have quantitative control of finite-size effects. Hence, an important task for future lattice calculations will be to determine at what level such finite-size effects are influencing the extraction of the nucleon's infinite-volume properties. For the axial charge, we find the finite-size dependence to be at most (4–5)% at $m_\pi = 356$ MeV (cf. Figure 3), but the effect is expected to grow in the chiral regime.

We find the axial charge of the nucleon to be (8–10)% lower than in the physical world, and its pion-mass dependence is very weak in the explored range; see Fig. 9. The latter observation is in qualitative agreement with the prediction of chiral effective theory, and continues up to pion masses far outside its range of validity. It is an important challenge to show that g_A really rises by (8–10)% as m_π is decreased from 300 MeV down to its physical value.

We have also presented extensive data on the generalized form factors (GFFs), which are related to the x moments of the generalized parton distributions (GPDs). The higher the spin of the twist-two operator, the smaller the radii of the associated GFFs. This observation holds throughout the explored pion-mass range (see Fig. 29) and is in accord with the expectation of a decreasing transverse size of the nucleon, as measured by the impact parameter of an active quark relative to the nucleon center of momentum, with increasing longitudinal momentum fraction x. Since only the vector and axial-vector radii (i.e. for the lowest moment $n = 1$) exhibit a statistically significant growth when the pion mass is reduced (cf. Figure 30), the hierarchy between these radii and those associated with higher spin operators increases toward the physical point. We have also found that the longitudinal momentum transfer ξ dependence of the GPDs is significant, as the ratios $C_{20}^{u+d}/A_{20}^{u+d}$ and $A_{32}^{u+d}/A_{30}^{u+d}$ show quite clearly; cf. Equation (8) and Figs. 33 and 34. This is, in fact, consistent with large-N_c counting rules, which predict, in particular, that $C_{20}^{u-d} \sim N_c \sim A_{20}^{u-d}$.

The GFFs in the forward limit, namely, the moments of parton distributions, exhibit a rather mild pion-mass dependence in the accessible range of pion masses. Specifically, both the unpolarized and polarized isovector momentum fractions, shown in Figs. 36 and 35, respectively, will have to bend down as a function of m_π beyond our range, if the lattice data are to make contact with experiment.

Finally, we applied our results for the moments of the GPDs to the decomposition of the proton spin—the final results are listed in Table XLIV. Thus, we extend our previous calculation in Ref. [20] down to $m_\pi = 290$ MeV, and increase its accuracy. The decomposition of quark angular momentum in terms of quark spin and quark orbital angular momentum is displayed in Fig. 46. The spin contributions are in agreement with the HERMES 2007 data [49], while orbital contributions are our predictions. We remind the reader, however, that our calculation did not include the disconnected graphs which contribute to all but isovector quantities, and that the mixing of the isosinglet quark operators with the gluonic operators was not taken into account. These systematic uncertainties should be kept in mind in the interpretation of the nonisovector results. The isovector quantities however, such as $\frac{1}{2}\Delta\Sigma^{u-d}$ and L^{u-d}, do not suffer from these systematic uncertainties. One of the surprises, from the relativistic quark-model point of view, is the negative sign of L^{u-d}. Various interpretations of this result have been proposed [109,116]. As pointed out in Ref. [109], L^{u-d} evolves rapidly at low renormalization scales, because $J^{u-d} = L^{u-d} + \frac{1}{2}\Delta\Sigma^{u-d}$ renormalizes multiplicatively and $\frac{1}{2}\Delta\Sigma^{u-d}$ is scale invariant. In any case, lattice studies of the Ji sum rule, Eq. (70), have led to a renewed interest in the problem of "decomposing the total angular momentum of an interacting multiconstituent system into contributions from various constituents" (cited from [116]; see also [117]).

Given that lattice QCD provides a systematically improvable way of solving QCD, there should be eventual agreement between nucleon properties calculated in this framework and those measured by experiment. Thus, an

extension of the present calculation down to $m_\pi = 200$ MeV is almost certain to uncover the dramatic effects predicted by chiral effective theory near the chiral limit. To be specific, the isovector Dirac radius $\langle r_1^2 \rangle$ and the Pauli radius $\langle r_2^2 \rangle$ can provide important benchmarks of our understanding of nucleon structure—they both need to grow particularly fast as m_π decreases below 250 MeV, if our lattice data are to make contact with the phenomenological values; see Figs. 12 and 16. The calculation of these and similar observables would thus test our understanding of both chiral effective field theory and of lattice calculations as applied to nucleon structure.

To achieve this goal we must be sure that statistical uncertainties, cutoff effects, and finite-size effects are well understood and under control. We believe that our current work provides an important step in this direction, as it demonstrates the improvement we have achieved in reducing statistical uncertainties and the application of chiral perturbation theory. In view of the success of our methods and techniques and given the recent increase in the computing power available to lattice QCD practitioners, we are optimistic that this program can be carried out successfully in the course of the next few years.

ACKNOWLEDGMENTS

The authors wish to thank George T. Fleming, Dru B. Renner, and Andre P. Walker-Loud for their contributions to this project and to the LHPC Collaboration for valuable discussions of the physics and presentation of this work. This work was supported in part by U.S. DOE Contracts No. DE-AC05-06OR23177 and No. DE-FG03-97ER4014, by the DOE Office of Nuclear Physics under Grants No. DE-FG02-94ER40818, No. DE-FG02-04ER41302, No. DE-FG02-96ER40965, No. DE-FG02-05ER25681, and No. DE-AC02-06CH11357, and the EU (I3HP) under Contract No. RII3-CT-2004-506078. This work was supported by DOE Contract No. DE-AC05-06OR23177, under which Jefferson Science Associates, LLC operates Jefferson Laboratory, and by DOE Contract No. DE-AC05-84ER40150 of the Southeastern Universities Research Association, Inc. Ph. H. and B. M. acknowledge support by the Emmy-Noether program and the cluster of excellence ''Origin and Structure of the Universe'' of the DFG. W. S. acknowledges support by the National Science Council of Taiwan under Grants No. NSC96-2112-M002-020-MY3 and No. NSC96-2811-M002-026 and by NuAS in Germany, and wishes to thank the Institute of Physics at Academia Sinica for their kind hospitality and support. W. S. particularly thanks Jiunn-Wei Chen at National Taiwan University and Hai-Yang Cheng and Hsiang-nan Li at Academia Sinica for their hospitality and for valuable physics discussions and suggestions. K. O. acknowledges support from the Jeffress Memorial Trust Grant No. J-813, and Ph. H., M. P., and W. S. acknowledge support by the Alexander von Humboldt-foundation through the Feodor-Lynen program. It is a pleasure to acknowledge the use of resources provided by the New Mexico Computing Applications Center (NMCAC) on Encanto, and of computer resources provided by the DOE through the USQCD project at Jefferson Lab and through its support of the MIT Blue Gene/L. These calculations were performed using the Chroma software suite [118]. We are indebted to members of the MILC Collaboration for providing the dynamical quark configurations that made our full QCD calculations possible.

[1] M. Göckeler *et al.* (QCDSF), Phys. Rev. Lett. **92**, 042002 (2004).
[2] P. Hägler *et al.* (LHPC), Phys. Rev. D **68**, 034505 (2003).
[3] P. Hägler *et al.* (LHPC), Phys. Rev. Lett. **93**, 112001 (2004).
[4] R. G. Edwards *et al.* (LHPC), Phys. Rev. Lett. **96**, 052001 (2006).
[5] A. A. Khan *et al.*, Phys. Rev. D **74**, 094508 (2006).
[6] C. Alexandrou, G. Koutsou, J. W. Negele, and A. Tsapalis, Phys. Rev. D **74**, 034508 (2006).
[7] C. Alexandrou, G. Koutsou, T. Leontiou, J. W. Negele, and A. Tsapalis, Phys. Rev. D **76**, 094511 (2007).
[8] H.-W. Lin, T. Blum, S. Ohta, S. Sasaki, and T. Yamazaki, Phys. Rev. D **78**, 014505 (2008).
[9] S. N. Syritsyn *et al.*, Phys. Rev. D **81**, 034507 (2010).
[10] C. Alexandrou *et al.*, Proc. Sci., LAT2009 (2009) 145.
[11] K. Takeda *et al.* (JLQCD), arXiv:0910.5036.
[12] J. M. Zanotti, Proc. Sci. LATTICE2008 (2008) 007 [arXiv:0812.3845].
[13] D. B. Renner, Proc. Sci., LAT2009 (2009) 018.
[14] M. Göckeler *et al.*, arXiv:0912.0167.
[15] P. Hägler, Phys. Rep. **490**, 49 (2010).
[16] C. W. Bernard *et al.*, Phys. Rev. D **64**, 054506 (2001).
[17] A. Bazavov *et al.*, Rev. Mod. Phys. **82**, 1349 (2010).
[18] J. W. Negele *et al.* (LHPC), Int. J. Mod. Phys. A **21**, 720 (2006).
[19] W. Schroers, Eur. Phys. J. A **31**, 784 (2007).
[20] P. Hägler *et al.* (LHPC), Phys. Rev. D **77**, 094502 (2008).
[21] A. Walker-Loud *et al.*, Phys. Rev. D **79**, 054502 (2009).
[22] S. N. Syritsyn *et al.*, Proc. Sci., LATTICE2008 (2008) 169.
[23] C. Alexandrou *et al.*, Phys. Rev. D **77**, 085012 (2008).
[24] W. Detmold *et al.*, Phys. Rev. D **78**, 014507 (2008).

[25] S. R. Beane, K. Orginos, and M. J. Savage, Int. J. Mod. Phys. E **17**, 1157 (2008).
[26] M. Golterman, T. Izubuchi, and Y. Shamir, Phys. Rev. D **71**, 114508 (2005).
[27] K. Orginos and A. Walker-Loud, Phys. Rev. D **77**, 094505 (2008).
[28] J.-W. Chen, D. O'Connell, and A. Walker-Loud, J. High Energy Phys. 04 (2009) 090.
[29] N. Mathur, S. J. Dong, K. F. Liu, L. Mankiewicz, and N. C. Mukhopadhyay, Phys. Rev. D **62**, 114504 (2000).
[30] V. Gadiyak, X.-D. Ji, and C.-W. Jung, Phys. Rev. D **65**, 094510 (2002).
[31] D. Müller, D. Robaschik, B. Geyer, F. M. Dittes, and J. Horejsi, Fortschr. Phys. **42**, 101 (1994).
[32] X.-D. Ji, Phys. Rev. D **55**, 7114 (1997).
[33] A. V. Radyushkin, Phys. Rev. D **56**, 5524 (1997).
[34] M. Diehl, Phys. Rep. **388**, 41 (2003).
[35] M. Deka *et al.*, Phys. Rev. D **79**, 094502 (2009).
[36] T. Doi *et al.*, Phys. Rev. D **80**, 094503 (2009).
[37] J. D. Bratt *et al.* (unpublished).
[38] M. Burkardt, Phys. Rev. D **62**, 071503 (2000).
[39] D. Dolgov *et al.* (LHPC), Phys. Rev. D **66**, 034506 (2002).
[40] C. Aubin *et al.*, Phys. Rev. D **70**, 094505 (2004).
[41] J. D. Bratt *et al.* (LHPC), Proc. Sci., LATTICE2008 (2008) 141.
[42] B. Efron, *The Jackknife, the Bootstrap, and Other Resampling Plans* (Society for Industrial and Applied Mathematics, Philadelphia, PA, 1982).
[43] W. Schroers, arXiv:hep-lat/0304016.
[44] T. Blum, C. Dawson, and T. Izubuchi (private communication).
[45] A. Ali Khan *et al.* (CP-PACS), Phys. Rev. D **65**, 054505 (2002).
[46] B. Bistrovic, Ph.D. thesis, MIT, Cambridge, MA, 2005.
[47] G. Martinelli, C. Pittori, C. T. Sachrajda, M. Testa, and A. Vladikas, Nucl. Phys. **B445**, 81 (1995).
[48] S. Syritsyn *et al.* (work in progress).
[49] A. Airapetian *et al.* (HERMES), Phys. Rev. D **75**, 012007 (2007).
[50] T. R. Hemmert, M. Procura, and W. Weise, Phys. Rev. D **68**, 075009 (2003).
[51] V. Bernard and U.-G. Meissner, Phys. Lett. B **639**, 278 (2006).
[52] T. Yamazaki *et al.* (RBC + UKQCD), Phys. Rev. Lett. **100**, 171602 (2008).
[53] C. F. Perdrisat, V. Punjabi, and M. Vanderhaeghen, Prog. Part. Nucl. Phys. **59**, 694 (2007).
[54] J. Friedrich and T. Walcher, Eur. Phys. J. A **17**, 607 (2003).
[55] J. Arrington, W. Melnitchouk, and J. A. Tjon, Phys. Rev. C **76**, 035205 (2007).
[56] G. Hohler *et al.*, Nucl. Phys. **B114**, 505 (1976).
[57] P. Mergell, U. G. Meissner, and D. Drechsel, Nucl. Phys. **A596**, 367 (1996).
[58] M. A. Belushkin, H. W. Hammer, and U. G. Meissner, Phys. Rev. C **75**, 035202 (2007).
[59] J. C. Bernauer, Lect. Notes Phys. **745**, 79 (2008).
[60] B. D. Milbrath *et al.* (Bates FPP), Phys. Rev. Lett. **80**, 452 (1998).
[61] T. Pospischil *et al.* (A1), Eur. Phys. J. A **12**, 125 (2001).
[62] O. Gayou *et al.* (Jefferson Lab Hall A), Phys. Rev. Lett. **88**, 092301 (2002).
[63] O. Gayou *et al.*, Phys. Rev. C **64**, 038202 (2001).
[64] V. Punjabi *et al.*, Phys. Rev. C **71**, 055202 (2005).
[65] T. R. Hemmert, B. R. Holstein, and J. Kambor, J. Phys. G **24**, 1831 (1998).
[66] M. Göckeler *et al.* (QCDSF), Phys. Rev. D **71**, 034508 (2005).
[67] V. Bernard, H. W. Fearing, T. R. Hemmert, and U. G. Meissner, Nucl. Phys. **A635**, 121 (1998).
[68] T. Gail, Ph.D. thesis, Technical University Munich, 2007.
[69] C. Amsler *et al.* (Particle Data Group), Phys. Lett. B **667**, 1 (2008).
[70] M. Procura, B. U. Musch, T. R. Hemmert, and W. Weise, Phys. Rev. D **75**, 014503 (2007).
[71] G. Colangelo and S. Dürr, Eur. Phys. J. C **33**, 543 (2004).
[72] M. Procura, T. R. Hemmert, and W. Weise, Phys. Rev. D **69**, 034505 (2004).
[73] M. Procura, B. U. Musch, T. Wollenweber, T. R. Hemmert, and W. Weise, Phys. Rev. D **73**, 114510 (2006).
[74] T. Becher and H. Leutwyler, Eur. Phys. J. C **9**, 643 (1999).
[75] M. Dorati, T. A. Gail, and T. R. Hemmert, Nucl. Phys. **A798**, 96 (2008).
[76] V. Bernard, N. Kaiser, and U.-G. Meissner, Nucl. Phys. **A615**, 483 (1997).
[77] N. Fettes, U.-G. Meissner, and S. Steininger, Nucl. Phys. **A640**, 199 (1998).
[78] D. R. Entem and R. Machleidt, Phys. Rev. C **66**, 014002 (2002).
[79] A. Ali Khan *et al.* (QCDSF-UKQCD), Nucl. Phys. **B689**, 175 (2004).
[80] M. Göckeler *et al.* (QCDSF), arXiv:0709.3370.
[81] M. Göckeler *et al.* (QCDSF/UKQCD), Proc. Sci., LAT2007 (2007) 161.
[82] T. R. Hemmert and W. Weise, Eur. Phys. J. A **15**, 487 (2002).
[83] R. G. Edwards *et al.* (LHPC), Proc. Sci., LAT2005 (2006) 056.
[84] Experiment E02-013 at Jefferson Lab, http://hallaweb.jlab.org/experiment/E02-013/.
[85] J. D. Bratt, Ph.D. thesis, MIT, Cambridge, MA, USA, 2009.
[86] V. Bernard, L. Elouadrhiri, and U. G. Meissner, J. Phys. G **28**, R1 (2002).
[87] T. Blum *et al.*, Phys. Rev. D **69**, 074502 (2004).
[88] M. Lüscher, S. Sint, R. Sommer, and P. Weisz, Nucl. Phys. **B478**, 365 (1996).
[89] S.-i. Ando, J.-W. Chen, and C.-W. Kao, Phys. Rev. D **74**, 094013 (2006).
[90] M. Diehl, A. Manashov, and A. Schäfer, Eur. Phys. J. A **31**, 335 (2007).
[91] M. Diehl, A. Manashov, and A. Schäfer, Eur. Phys. J. A **29**, 315 (2006).
[92] X.-D. Ji, Phys. Rev. Lett. **74**, 1071 (1995).
[93] A. Airapetian *et al.* (HERMES), Phys. Lett. B **682**, 345 (2010).
[94] M. Diehl, T. Feldmann, R. Jakob, and P. Kroll, Eur. Phys. J. C **39**, 1 (2005).

[95] M. V. Polyakov and C. Weiss, Phys. Rev. D **60**, 114017 (1999).
[96] R. G. Edwards *et al.*, Proc. Sci., LAT2006 (2006) 121.
[97] P. J. Sutton, A. D. Martin, R. G. Roberts, and W. J. Stirling, Phys. Rev. D **45**, 2349 (1992).
[98] M. Glück, E. Reya, and I. Schienbein, Eur. Phys. J. C **10**, 313 (1999).
[99] H. B. Meyer and J. W. Negele, Phys. Rev. D **77**, 037501 (2008).
[100] M. Guagnelli *et al.* (Zeuthen-Rome (ZeRo)), Eur. Phys. J. C **40**, 69 (2005).
[101] J. Pumplin *et al.*, J. High Energy Phys. 07 (2002) 012.
[102] A. D. Martin *et al.*, Eur. Phys. J. C **28**, 455 (2003).
[103] J.-W. Chen and X.-D. Ji, Phys. Rev. Lett. **88**, 052003 (2002).
[104] S. J. Brodsky, D. S. Hwang, B.-Q. Ma, and I. Schmidt, Nucl. Phys. **B593**, 311 (2001).
[105] S. J. Brodsky, D. S. Hwang, and I. Schmidt, Phys. Lett. B **530**, 99 (2002).
[106] M. Burkardt and D. S. Hwang, Phys. Rev. D **69**, 074032 (2004).
[107] S. J. Brodsky and S. D. Drell, Phys. Rev. D **22**, 2236 (1980).
[108] M. Wakamatsu and Y. Nakakoji, Phys. Rev. D **77**, 074011 (2008).
[109] A. W. Thomas, Phys. Rev. Lett. **101**, 102003 (2008).
[110] X.-D. Ji, J. Tang, and P. Hoodbhoy, Phys. Rev. Lett. **76**, 740 (1996).
[111] M. Mazouz *et al.* (Jefferson Lab Hall A), Phys. Rev. Lett. **99**, 242501 (2007).
[112] A. Airapetian *et al.* (HERMES), J. High Energy Phys. 06 (2008) 066.
[113] S. V. Goloskokov and P. Kroll, Eur. Phys. J. C **59**, 809 (2009).
[114] A. Airapetian *et al.* (HERMES), Phys. Lett. B **679**, 100 (2009).
[115] C. Schill (COMPASS), arXiv:0807.5021.
[116] M. Burkardt and B. C. Hikmat, Phys. Rev. D **79**, 071501 (2009).
[117] F. Wang, X. S. Chen, X. F. Lu, W. M. Sun, and T. Goldman, arXiv:0909.0798.
[118] R. G. Edwards and B. Joo (SciDAC), Nucl. Phys. B, Proc. Suppl. **140**, 832 (2005).